Electrohydrodynamic Modeling of Droplet Vibrations under the Influence of Electric Fields

Elektrohydrodynamische Modellierung von Wassertropfenvibrationen unter dem Einfluss elektrischer Felder
Zur Erlangung des akademischen Grades Doktor-Ingenieur (Dr.-Ing.)
genehmigte Dissertation von Dipl.-Ing. Harald Songoro aus Orléans, France
März 2015 — Darmstadt — D 17

TECHNISCHE
UNIVERSITÄT
DARMSTADT

Fachbereich Elektrotechnik und Informationstechnik
Institut für Theorie Elektromagnetischer Felder (TEMF)

Electrohydrodynamic Modeling of Droplet Vibrations under the Influence of Electric Fields
Elektrohydrodynamische Modellierung von Wassertropfenvibrationen unter dem Einfluss elektrischer Felder

Genehmigte Dissertation von Dipl.-Ing. Harald Songoro aus Orléans, France

1. Gutachten: Prof. Dr.-Ing. Thomas Weiland
2. Gutachten: Prof. Dr.-Ing. Herbert De Gersem

Tag der Einreichung: 16.12.2014
Tag der Prüfung: 12.03.2015

Darmstadt, 2015 — D 17

Bitte zitieren Sie dieses Dokument als:
URN: urn:nbn:de:tuda-tuprints-44718
URL: http://tuprints.ulb.tu-darmstadt.de/4471

Erklärung laut §9 PromO

Ich versichere hiermit, dass ich die vorliegende Dissertation allein und nur unter Verwendung der angegebenen Literatur verfasst habe. Die Arbeit hat bisher noch nicht zu Prüfungszwecken gedient.

16.12.2014

Acknowledgments

This thesis would not have been possible without the support and advices of many people. In particular, I would like to thank Prof. Dr.-Ing. Thomas Weiland for giving me the opportunity to work at TEMF and for his supervision.

I am also particularly grateful to Prof. Dr.-Ing. Herbert De Gersem for accepting to be Co-Referee and to PD Dr. rer. nat. Erion Gjonaj for his continuous assistance, many stimulating discussions and for reading this thesis.

I would like to acknowledge the Deutsche Forschungsgemeinschaft (DFG) for their financial support within the framework of the Collaborative Research Center Transregio 75. "Droplet Dynamics Under Extreme Ambient Conditions".

I would like to thank Ph. D. Candidate Mohammed Nazemi for providing measurement data and Ph. D. Candidate Jens Trommler for providing me with extensive Linux support.

Additionally, I would like to thank all my colleagues from TEMF for fruitful discussions and for creating a very friendly atmosphere.

Finally, I would like to thank my family and friends, especially Alena Ey and Michael Pedersen, for all their support.

Kurzfassung

Die Dynamik von Wassertropfen unter Einwirkung elektrischer Felder spielt für viele Ingenieursanwendungen eine wesentliche Rolle. Ein Beispiel ist die, durch Regentropfen hervorgerufene, Alterung der Kunststoffoberfläche von Freiluft- Hochspannungsisolatoren. Hierbei verursachen auf der Oberfläche haftende Wassertropfen unzählige elektrische Teilentladungen, welche das Material beschädigen und damit die Lebensdauer von Hochspannungsisolatoren verkürzen.

Motiviert durch diese Problematik beschäftigt sich die vorliegende Arbeit mit der numerischen Simulation der Dynamik von Wassertropfen unter Einwirkung von starken zeitabhängigen Hochspannungsfeldern. Unter Dynamik wird im Folgenden sowohl die Bewegung als auch die Verformung des Wassertropfens verstanden. Die Anwendung eines statischen elektrischen Feldes auf einen Wassertropfen führt lediglich zu einer Verlängerung der Geometrie des Tropfens entlang der Hauptrichtung des externen Feldes; ein Vorgang, welcher auch theoretisch gut verstanden ist. Im zeitabhängigen Fall durchlaufen die Wassertropfen eine wesentlich kompliziertere oszillierende Bewegung, wobei sich die elektrische Feldverteilung und die Tropfenform gleichzeitig ändern und sich gegenseitig beeinflussen. Dieser multiphysikalisch gekoppelte Prozess war inzwischen Gegenstand zahlreicher experimenteller Studien, konnte jedoch bisher nicht numerisch simuliert werden.

In der vorliegenden Arbeit wird ein numerisches Verfahren zur Simulation, der durch das elektrische Feld erzwungenen Bewegung eines einzelnen Wassertropfens auf einer Kunststoffoberfläche vorgestellt. Das Verfahren besteht in der numerischen Lösung der zeitabhängigen, dreidimensionalen elektroquasistatischen Feldgleichungen gekoppelt mit den Navier-Stokes-Gleichungen. Zur Lösung des elektrischen Teilproblems wurde ein spezieller FEM-Ansatz mit dynamischen, der Geometrie angepassten Gittern entwickelt. Hierbei werden gekrümmte Tetraeder-Elemente hoher Ordnung verwendet, welche eine akkurate Berechnung des maxwellschen Spannungstensors und damit der elektrischen Kraftdichteverteilung im Tropfen ermöglichen. Auf der anderen Seite wird, für die Berechnung der sich ändernden Tropfengeometrie unter Einwirkung dieser Kräfte, ein Mehrphasen-Finite-Volumen-Verfahren eingesetzt. Die grösste Herausforderung besteht in der Realisierung einer numerisch effizienten Kopplungsschnittstelle zwischen den elektrischen und strömungsdynamischen Teilproblemen. Diese Schnittstelle beinhaltet eine Prozedur zur numerischen Rekonstruktion der Tropfenoberfläche, in der dynamischen Anpassung des Rechengitters an die Tropfengeometrie und schliesslich in der Implementierung eines Multiraten-Zeitintegrationsverfahrens mit einer geeigneter zeitlicher Synchronisation zwischen den Teillösungen des gekoppelten Problems.

Der Vergleich zwischen der numerisch berechneten Tropfenbewegung und der entsprechenden, mit einer Hochgeschwindigkeitskamera aufgezeichneten Videobildern zeigt eine gute Übereinstimmung sowohl für horizontal als auch für vertikal angelegte elektrische Wechselfelder. Die Simulationsergebnisse werden ferner mithilfe eines eindimensionalen linearen Oszillatormodells analysiert. Dieses einfache Modell eignet sich gut dafür, das Einschwingverhalten des Tropfens besser zu verstehen. Dabei wird gezeigt, dass die beobachteten Tropfenvibrationen, welche bei Frequenzen unterhalb der Erregerfrequenz

auftreten, nicht notwendigerweise auf einer elektrischen Aufladung des Wassertropfens zurückzuführen sind. Vielmehr könnten diese untergedämpfte freien Vibrationsmoden entsprechen, welche aufgrund der sehr langen Einschwingzeiten, sowohl im Experiment als auch in der Simulation zu beobachten sind. Diese Erkenntnis wird auch dadurch gestützt, dass die Frequenzen dieser Unterharmonischen mit den Eigenschwingfrequenzen eines freien sessilen Wassertropfens übereinstimmen.

Abstract

This work focuses on numerical simulations of water droplet deformations under the influence of transient high-voltage electric fields. In the stationary case, the droplet elongates parallel to the electrostatic field. In the transient case, water droplets undergo a complicated oscillatory motion as the electric field and the droplet shape change simultaneously.

This multiphysics phenomenon has been the subject of experimental studies but has never been simulated before in the case of a transient electric field. Practical applications of this work include the numerical study of the premature aging of polymer insulators used in power transmission lines and due to water droplets as well as the simulation of industrial processes such as electrowetting and dielectrophoresis.

In this thesis, the motion of a single water droplet located on the hydrophobic surface of a silicone rubber insulator is simulated numerically. This is achieved by solving the transient, three-dimensional system composed of the full sets of electro-quasistatics and Navier-Stokes equations. The solution of the coupled system is obtained by using a computational approach based on the finite element method on a moving mesh for the electrical part of the problem and on the finite volume method on a fixed mesh for the fluid mechanical part. The electro-quasistatics finite element solver calculates on a moving curvilinear tetrahedral mesh the electric field, Maxwell stress tensor and electric force density with higher and mixed-element orders. The multiphase flow finite volume solver computes on a fixed Cartesian hexahedral grid the droplet deformation by tracking the evolution of the water-air interface with the volume of fluid method. Both solvers use an independent time integration scheme but are leapfrogged in a synchronized manner to provide a time accurate calculation of the droplet deformations.

Several experimental investigations are performed to verify simulation results using a high speed camera. The comparison between simulation and experiment shows good agreement between the numerically computed droplet motion and the recorded video images for both horizontal and vertical applied AC electric fields.

The simulation results are analyzed by applying a one-dimensional mechanical model of water droplet deformation based on the linear harmonic oscillator. The standard model which is limited to the steady-state regime is extended to include the transient regime. It is shown that the droplet vibrations occuring at frequencies below the driving frequency are not necessarily due to the accidental charging of the water droplet as it is sometimes suggested in the literature. Rather, they may be caused by underdamped droplet oscillations which originate in the transient regime. This finding is further supported by the fact that their frequencies correspond to the resonance frequencies of the sessile water droplets oscillating freely.

Contents

1 Introduction

Advances in computer simulation over the past decades have transformed applied sciences and product development. Increases in computing speed have enabled the simulation of complex real-world models and advances in numerical techniques have improved the efficiency of simulation software. Simulation based science and engineering have largely focused on applications dominated by one physical effect, usually mechanical, electrical or thermal.

Most processes, however, involve combinations of multiple physical effects which must be modeled in order to include all relevant physical effects. Such multiphysics problems typically involve coupled systems of partial differential equations and are among the most challenging problems to solve.

A classical approach to solving multiphysics problem is linking together stand-alone solvers within a shared simulation framework. This modular approach has been successfully used by researchers and multiphysics simulation software. However, it is best suited for weakly coupled problems and it is less practicable for strongly coupled problems such as in computational electrohydrodynamics where time-varying electric fields interact with surrounding fluids. In addition, stand-alone solvers are tailored for a specific range of applications and are not easily customizable.

These issues have been addressed recently with the emergence of open source simulation libraries such as NGsolve [1] or OpenFoam [2] which provide a simulation framework to develop and combine customized solvers. However, these frameworks favor a single discretization method such as the finite element or finite volume method which are not optimal for all classes of partial differential equations or types of geometry. For instance, the finite volume method is hardly used in computational electromagnetics whereas it is ubiquitous in computational fluid dynamics.

This work focuses on a multiphysics approach which combined in a new way multiple discretization methods in order to simulate the vibrational motion of droplets under the influence of electric fields.

1.1 Motivation

Droplet electrohydrodynamics plays a key role in many industrial processes. This is the case in electrowetting or dielectrophoresis which is increasingly used in medical applications. It is also relevant in natural processes such as droplet induced electrical discharge on wet insulating surfaces in power transmission lines.

This latter phenomenon has been the subject of experimental studies [3] but has never been investigated numerically in the case of non-stationary electric field. In the stationary case, the droplet elongates parallel to the electrostatic field if the field is strong enough. This process can be modeled as a coupled problem as in [4], [5]. In the non-stationary case, the electric field and the droplet shape change simultaneously and the droplet starts to vibrate. This corresponds to the case of a strongly coupled problem and requires the solution in a time-accurate manner of the coupled electrical and fluid dynamics problem. The electrical problem is an initial boundary value problem with strong electric field gradients near the droplet interface where the droplet curvature plays an important role. Boundary value problems on curved domains are best resolved by using high order finite element discretizations for the droplet geometry and for the electric field. The fluids dynamics problem is an incompressible multiphase flow with a free air-water interface. Multiphase solvers based on the finite volume method on a Cartesian grid are known to perform well for such problems. Consequently we propose to solve the electrohydrodynamics problem for non-stationary electric fields by a coupling approach based on the finite volume method and the finite element method on a moving curvilinear mesh.

1.2 Application

This work focuses on a particular application from power transmission line technology. The object of investigation is the electrical breakdown triggered by vibration of rainwater droplets on polymeric insulator surface. This phenomenon is responsible for the premature aging of polymer insulators (cf. Figure 1.1). The droplet deformations amplify the electric field near the droplet interface, especially at the contact line where water is in contact with both air and polymer, which may cause an electrostatic discharge. Moreover the electric strength at the contact line can be amplified substantially depending on the contact angle between the droplet surface and the insulator plane. Over time, these physical damages reduce the resistance and hydrophobicity of the insulator leading to its premature degradation. These phenomena have recently become important since ceramic insulators have been replaced in recent years by lighter and more effective polymer insulators.

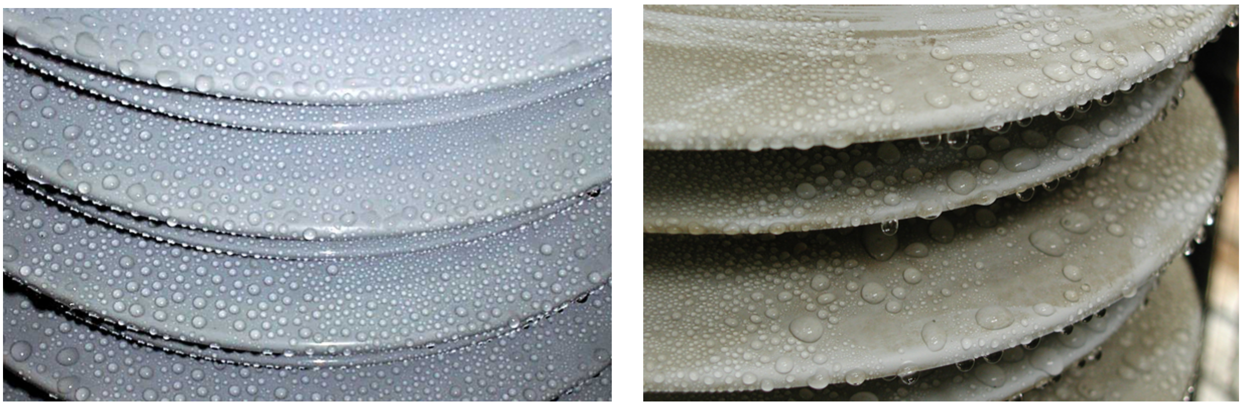

Figure 1.1.: Undamaged (left) and damaged (right) insulator surface. The surface hydrophobicity is reduced because of droplet induced partial discharge (courtesy of Prof. Dr.-Ing. V. Hinrichsen, Technische Universität Darmstadt).

1.3 Outline

This thesis is organized as follows. In chapter 2 we state the mathematical model used for the electrohydrodynamic problem of rainwater droplet vibrations on polymer insulators and we derive the electric force causing the droplet deformations. In chapter 3 we give a step-by-step development of the finite element method on a moving mesh and calculate the discretized electric force in the curvilinear mesh. In chapter 4 we give an overview of the customized multiphase flow solver built with OpenFoam to solve the fluid dynamics problem. Chapter 5 is devoted to the solution of the coupled problem. We first propose a scheme to couple in time the electrical and fluid dynamics solvers. Both solvers use an independent time integration scheme but are leapfrogged in a synchronized manner to provide a time-accurate calculation of the droplet deformations. We then present several meshing techniques for multiple discretization methods, in particular related to the use of curvilinear elements. Chapter 6 is devoted to the validations and applications of the proposed method. We first compare the simulation results of a water droplet placed in an externally applied transient electric field to experimental data corresponding to the same set-up. Then, we propose a mechanical model of water droplet deformation consistent with the simulated and experimental results .

2 The electrohydrodynamic model

An electrohydrodynamic model of a water droplet under high voltage fields can be represented by a single droplet lying on a planar insulator block. The droplet vibrations are caused by an externally applied transient electric field $\vec{E}$ which is oriented either parallel or normal to the insulator surface. This phenomenon is illustrated in Figure 2.1. It corresponds to an electrical and fluid dynamics coupled problem where the time-dependent electric force density $\vec{f_e}$ tends to deform the droplet while the gravitational force $\vec{g}$ and the surface tension force $\vec{f_s}$ tend to bring back the droplet to its equilibrium shape as shown in Figure 2.1.

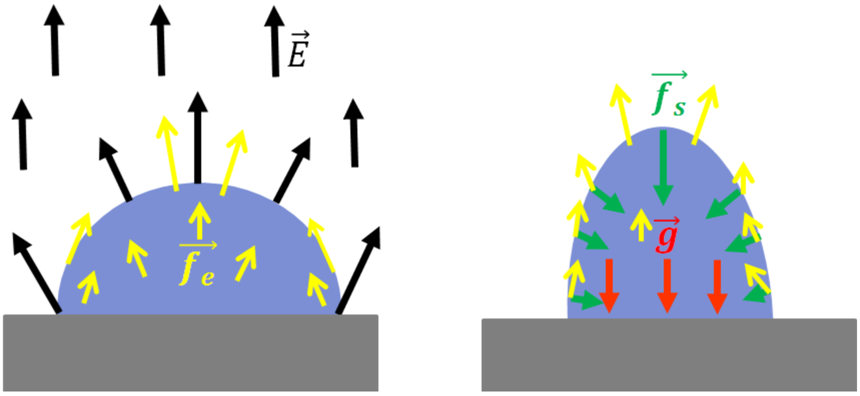

Figure 2.1.: Electrical and mechanical forces acting on a water droplet.

2.1 The electrical model

Power transmission typically operate at 50 or 60Hz. Experiments show that millimetric water droplets (such as rainwater droplets) vibrate at frequencies which are approximately multiple of the frequency of the externally applied electric field [6]. Therefore the characteristic time constant τ of the model is greater than $1ms$. The characteristic spatial dimension l of the model is twice the droplet radius which is less than $1cm$. Thus, the maximum velocity $v = \frac{\tau}{l}$ of any droplet deformation is well below the light celerity in water $\simeq 10^8 m/s$. Under these assumptions, Maxwell's equations for stationary media still apply [7]. Since all materials involved are non magnetic, induced eddy currents can be neglected and the electric field at these frequencies is essentially irrotational [8]. Maxwell's equations can, thus, be simplified to the electro-quasistatic equation:

$$\begin{aligned} \vec{E} &= -\vec{\nabla} V, && (2.1) \\ -\vec{\nabla} \cdot \left(\frac{\partial \varepsilon \cdot \vec{\nabla} V}{\partial t} \right) &= \vec{\nabla} \cdot \left(\sigma \vec{\nabla} V \right), && (2.2) \end{aligned}$$

where V is the scalar potential, ε the permittivity, σ the electrical conductivity.

The solution of the electro-quasistatic equation determines the electric field causing droplet vibrations. In the next sections the electric force density acting on a isotropic linear dielectric medium is derived by using two different approaches.

2.1.1 The Kelvin polarization force density

In this approach, the interaction of the externally applied electric field with the water molecules represented by elementary dipoles is considered. In the absence of magnetic field, the Lorentz force density acting on the electric dipole of charge Q consists only of the Coulomb force. Denoting the two poles by M and N, respectively, the total force acting on the dipole is $\vec{F}_e = Q\left(\vec{E}_N - \vec{E}_M\right)$, where $\vec{E}_N$ and $\vec{E}_M$ are the electrical fields at the respective position. Thus, the electric field gradient is given by:

$$\vec{E}_N - \vec{E}_M = \begin{pmatrix} \begin{pmatrix} \frac{\partial E_x}{\partial x} & \frac{\partial E_x}{\partial y} & \frac{\partial E_x}{\partial z} \end{pmatrix} \\ \begin{pmatrix} \frac{\partial E_y}{\partial x} & \frac{\partial E_y}{\partial y} & \frac{\partial E_y}{\partial z} \end{pmatrix} \\ \begin{pmatrix} \frac{\partial E_z}{\partial x} & \frac{\partial E_z}{\partial y} & \frac{\partial E_z}{\partial z} \end{pmatrix} \end{pmatrix} \cdot \begin{pmatrix} \overrightarrow{MN} \\ \overrightarrow{MN} \\ \overrightarrow{MN} \end{pmatrix}. \tag{2.3}$$

We evaluate the electric force acting on the dipole according to[10]:

$$\vec{F}_e = Q\left(\vec{E}_N - \vec{E}_M\right) = Q \begin{pmatrix} \begin{pmatrix} \frac{\partial E_x}{\partial x} & \frac{\partial E_x}{\partial y} & \frac{\partial E_x}{\partial z} \end{pmatrix} \\ \begin{pmatrix} \frac{\partial E_y}{\partial x} & \frac{\partial E_y}{\partial y} & \frac{\partial E_y}{\partial z} \end{pmatrix} \\ \begin{pmatrix} \frac{\partial E_z}{\partial x} & \frac{\partial E_z}{\partial y} & \frac{\partial E_z}{\partial z} \end{pmatrix} \end{pmatrix} \cdot \begin{pmatrix} \vec{d} \\ \vec{d} \\ \vec{d} \end{pmatrix} = \begin{pmatrix} p_x \frac{\partial E_x}{\partial x} + p_y \frac{\partial E_x}{\partial y} + p_z \frac{\partial E_x}{\partial z} \\ p_x \frac{\partial E_y}{\partial x} + p_y \frac{\partial E_y}{\partial y} + p_z \frac{\partial E_y}{\partial z} \\ p_x \frac{\partial E_z}{\partial x} + p_y \frac{\partial E_z}{\partial y} + p_z \frac{\partial E_z}{\partial z} \end{pmatrix}, \tag{2.4}$$

where $\vec{d} = \overrightarrow{MN}$ and $\vec{p} = \left(p_x \; p_y \; p_z\right)^t = Q\vec{d}$ is the electric dipole moment.
By denoting $\vec{P}$ the average electric dipole moment per unit of volume, we obtain the macroscopic electric force density acting on the dielectric medium which is called the Kelvin polarization force density $\vec{f_K}$:

$$\vec{f_K} \;=\; \left(\vec{P} \cdot \vec{\nabla}\right) \vec{E}. \tag{2.5}$$

For an isotropic linear dielectric medium the polarization is proportional to the electric field:

$$\vec{P} = \varepsilon_0 \chi \vec{E}. \tag{2.6}$$

where $\chi = \varepsilon_r - 1$ is the electric susceptibility of the medium. The permittivity and the electric susceptibility are functions of the position. Therefore, the Kelvin polarization force density becomes:

$$\vec{f_K} = (\varepsilon - \varepsilon_0) \begin{pmatrix} \frac{\partial V}{\partial x} \frac{\partial^2 V}{\partial x^2} + \frac{\partial V}{\partial y} \frac{\partial^2 V}{\partial y \partial x} + \frac{\partial V}{\partial z} \frac{\partial^2 V}{\partial z \partial x} \\ \frac{\partial V}{\partial x} \frac{\partial^2 V}{\partial x \partial y} + \frac{\partial V}{\partial y} \frac{\partial^2 V}{\partial y^2} + \frac{\partial V}{\partial z} \frac{\partial^2 V}{\partial z \partial y} \\ \frac{\partial V}{\partial x} \frac{\partial^2 V}{\partial x \partial z} + \frac{\partial V}{\partial y} \frac{\partial^2 V}{\partial y \partial z} + \frac{\partial V}{\partial z} \frac{\partial^2 V}{\partial z^2} \end{pmatrix}. \tag{2.7}$$

The Kelvin force polarization density can also be written as:

$$\vec{f_K} = \left(\vec{P}\cdot\vec{\nabla}\right)\vec{E} = \frac{1}{2}\left(\varepsilon-\varepsilon_0\right)\vec{\nabla}\left(\vec{E}\cdot\vec{E}\right). \tag{2.8}$$

by using the vector identity $\left(\vec{E}\cdot\vec{\nabla}\right)\vec{E} = \left(\vec{\nabla}\times\vec{E}\right)\times\vec{E} + \frac{1}{2}\vec{\nabla}\left(\vec{E}\cdot\vec{E}\right)$ with $\vec{\nabla}\times\vec{E} = 0$.
In addition, when the permittivity is a differentiable function of position, (2.8) becomes:

$$\vec{f_K} = \frac{1}{2}\left(\varepsilon-\varepsilon_0\right)\vec{\nabla}\left(\vec{E}\cdot\vec{E}\right) = \frac{1}{2}\vec{\nabla}\left(\left(\varepsilon-\varepsilon_0\right)\vec{E}\cdot\vec{E}\right) - \frac{1}{2}\left(\vec{E}\cdot\vec{E}\right)\vec{\nabla}\varepsilon. \tag{2.9}$$

Free charges are absent from rainwater under normal conditions but are included in the model for the sake of generality. The Lorentz force acting only on the free charge is $\varrho_f\vec{E}$ where $\varrho_f = \vec{\nabla}\cdot\vec{D}$. Thus, the total electric force density acting on the free charges and on the charges bounded to the water molecules is:

$$\vec{f_e} = \varrho_f\vec{E} + \left(\vec{P}\cdot\vec{\nabla}\right)\vec{E} = \varrho_f\vec{E} + \frac{1}{2}\left(\varepsilon-\varepsilon_0\right)\vec{\nabla}\left(\vec{E}\cdot\vec{E}\right), \tag{2.10}$$

or, alternatively:

$$\vec{f_e} = \varrho_f\vec{E} + \frac{1}{2}\vec{\nabla}\left(\left(\varepsilon-\varepsilon_0\right)\vec{E}\cdot\vec{E}\right) - \frac{1}{2}\left(\vec{E}\cdot\vec{E}\right)\vec{\nabla}\varepsilon. \tag{2.11}$$

2.1.2 The Korteweg-Helmholtz force density

In this approach the electric force density is derived by applying the principle of virtual work to a dielectric medium responding to an applied electric field. The total electrostatic energy density W in a dielectric medium is given by [9] :

$$W\left(\vec{D}\right) = \int_0^{\vec{D}} \vec{E}\cdot d\vec{D}. \tag{2.12}$$

In general, $\vec{E} = f\left(\alpha_1, \ldots \alpha_n, \vec{D}\right)$ where f is a constitutive law for the dielectric medium corresponding to a physical model parametrized by the α_i and $\vec{D}$.
The force density acting on such medium is the Korteweg-Helmholtz force density [10] :

$$\vec{f_{KH}} \quad = \quad \varrho_f\vec{E} - \sum_{0\leq i\leq n}\alpha_i\vec{\nabla}\left(\left.\frac{\partial W}{\partial\alpha_i}\right|_{\alpha_j,\vec{D}}\right), \tag{2.13}$$

where ϱ_f is the free charge density.
The constitutive law for the isotropic linear dielectric medium used in (2.1.1) is

$$\vec{E} = f\left(\chi,\vec{D}\right) = \frac{1}{\varepsilon_0\left(\chi+1\right)}\vec{D}. \tag{2.14}$$

Its electrostatic energy density is calculated according to (2.12) as:

$$W\left(\vec{D}\right) = \int_0^{\vec{D}} \frac{1}{\varepsilon_0\left(\chi+1\right)}\vec{D}\cdot d\vec{D} = \frac{1}{\varepsilon_0\left(\chi+1\right)}\left(\frac{1}{2}\vec{D}\cdot\vec{D}\right) \tag{2.15}$$

$$\text{or } \left.\frac{\partial W}{\partial \chi}\right|_{\vec{D}} = -\frac{1}{\varepsilon_0(\chi+1)^2}\left(\frac{1}{2}\vec{D}\cdot\vec{D}\right) = -\frac{1}{2}\varepsilon_0\left(\vec{E}\cdot\vec{E}\right). \tag{2.16}$$

This yields the following force density according to (2.13) :

$$\vec{f}_{KH} = \varrho_f\vec{E} + \frac{1}{2}\chi\varepsilon_0\vec{\nabla}\left(\vec{E}\cdot\vec{E}\right) = \varrho_f\vec{E} + \frac{1}{2}\left(\varepsilon-\varepsilon_0\right)\vec{\nabla}\left(\vec{E}\cdot\vec{E}\right) = \vec{f}_e. \tag{2.17}$$

The expression (2.10) of the electric force density is, thus, recovered.
Assuming that the permittivity is a differentiable function of position, the Korteweg-Helmholtz force density can also be written as :

$$\vec{f}_{KH} = \varrho_f\vec{E} - \sum_{0\le i\le n}\vec{\nabla}\left(\alpha_i\left.\frac{\partial W}{\partial \alpha_i}\right|_{\alpha_j,\vec{D}}\right) + \sum_{0\le i\le n}\left(\left.\frac{\partial W}{\partial \alpha_i}\right|_{\alpha_j,\vec{D}}\right)\vec{\nabla}\alpha_i, \tag{2.18}$$

$$\vec{f}_{KH} = \varrho_f\vec{E} - \vec{\nabla}\left(\chi\left.\frac{\partial W}{\partial \chi}\right|_{\vec{D}}\right) + \left(\left.\frac{\partial W}{\partial \chi}\right|_{\vec{D}}\right)\vec{\nabla}\chi, \tag{2.19}$$

where ϱ_f is the free charge density. Finally, the Korteweg-Helmholtz force density becomes:

$$\vec{f}_{KH} = \varrho_f\vec{E} + \frac{1}{2}\vec{\nabla}\left(\left(\varepsilon-\varepsilon_0\right)\vec{E}\cdot\vec{E}\right) - \frac{1}{2}\left(\vec{E}\cdot\vec{E}\right)\vec{\nabla}\varepsilon = \vec{f}_e, \tag{2.20}$$

which is the same as (2.11).
Both approaches are, therefore, equivalent for an isotropic linear dielectric medium.
Note that the constitutive law employed for both approaches does not include the electrostriction effect, since the electric field is assumed to be independent from the mechanical pressure.

2.1.3 The Maxwell stress tensor

The total electric force acting on a volume V is given by:

$$\vec{F}_e = \iiint_V \vec{f}_e dV. \tag{2.21}$$

This integral quantity is often of more interest for numerical methods than the force density. It is convenient to express the electric force density as the divergence of a stress tensor noted by T in order to apply the divergence theorem:

$$\vec{F}_e = \iiint_V \operatorname{div}(\mathsf{T})\,dV = \iiint_V \begin{pmatrix} \vec{\nabla}\cdot\left(T_{11} & T_{12} & T_{13}\right) \\ \vec{\nabla}\cdot\left(T_{21} & T_{22} & T_{23}\right) \\ \vec{\nabla}\cdot\left(T_{31} & T_{32} & T_{33}\right) \end{pmatrix} dV. \tag{2.22}$$

The divergence theorem applied to a vector field $\vec{F}$ and to the gradient of a scalar function g in a volume V yields:

$$\iiint_V \left(\vec{\nabla}\cdot\vec{F}\right) dV = \iint_{\partial V} \vec{F}\cdot\vec{n}dS \text{ and } \iiint_V \left(\vec{\nabla}g\right) dV = \iint_{\partial V} g\vec{n}dS. \tag{2.23}$$

where the closed surface ∂V is oriented by the normal $\vec{n}$ pointing outwards of V.
The electric force density (2.10) including the free charge is written as:

$$\vec{f_e} = \varrho_f \vec{E} + \frac{1}{2}\left(\varepsilon - \varepsilon_0\right)\vec{\nabla}\left(\vec{E}\cdot\vec{E}\right). \tag{2.24}$$

In order to derive the tensor we define the bilinear function **R** as:

$$\mathbf{R}\left(\vec{P},\vec{E}\right) = \begin{pmatrix} \frac{\partial P_x E_x}{\partial x} + \frac{\partial P_y E_x}{\partial y} + \frac{\partial P_z E_x}{\partial z}) \\ \frac{\partial P_x E_y}{\partial x} + \frac{\partial P_y E_y}{\partial y} + \frac{\partial P_z E_y}{\partial z} \\ \frac{\partial P_x E_z}{\partial x} + \frac{\partial P_y E_z}{\partial y} + \frac{\partial P_z E_z}{\partial z} \end{pmatrix}. \tag{2.25}$$

The product rule for derivatives yields $\mathbf{R}\left(\vec{P},\vec{E}\right) = \left(\vec{P}\cdot\vec{\nabla}\right)\vec{E} + \left(\vec{\nabla}\cdot\vec{P}\right)\vec{E}$. By definition, $\vec{P} = \vec{D} - \varepsilon_0\vec{E}$, therefore, $\mathbf{R}\left(\vec{P},\vec{E}\right) = \mathbf{R}\left(\vec{D},\vec{E}\right) - \varepsilon_0\mathbf{R}\left(\vec{E},\vec{E}\right)$. Thus,

$$\begin{aligned} \mathbf{R}\left(\vec{D},\vec{E}\right) - \varepsilon_0\mathbf{R}\left(\vec{E},\vec{E}\right) &= \left(\vec{P}\cdot\vec{\nabla}\right)\vec{E} + \left(\vec{\nabla}\cdot\vec{D}\right)\vec{E} - \varepsilon_0\left(\vec{\nabla}\cdot\vec{E}\right)\vec{E}, && (2.26)\\ \mathbf{R}\left(\vec{D},\vec{E}\right) - \varepsilon_0\left(\vec{E}\cdot\vec{\nabla}\right)\vec{E} &= \left(\vec{P}\cdot\vec{\nabla}\right)\vec{E} + \left(\vec{\nabla}\cdot\vec{D}\right)\vec{E}, && (2.27)\\ \mathbf{R}\left(\vec{D},\vec{E}\right) - \frac{1}{2}\varepsilon_0\vec{\nabla}\left(\vec{E}\cdot\vec{E}\right) &= \vec{f_K} + \varrho_f\vec{E} = \vec{f_e}. && (2.28) \end{aligned}$$

The electric force density can therefore be expressed as the divergence of the following stress tensor:

$$\begin{aligned} \vec{f_e} &= \begin{pmatrix} \frac{\partial D_x E_x - \frac{1}{2}\varepsilon_0 E^2}{\partial x} + \frac{\partial D_y E_x}{\partial y} + \frac{\partial D_z E_x}{\partial z}) \\ \frac{\partial D_x E_y}{\partial x} + \frac{\partial D_y E_y - \frac{1}{2}\varepsilon_0 E^2}{\partial y} + \frac{\partial D_z E_y}{\partial z} \\ \frac{\partial D_x E_z}{\partial x} + \frac{\partial D_y E_z}{\partial y} + \frac{\partial D_z E_z - \frac{1}{2}\varepsilon_0 E^2}{\partial z} \end{pmatrix}. && (2.29)\\ &= \operatorname{div}\begin{pmatrix} D_x E_x - \frac{1}{2}\varepsilon_0 E^2 & D_y E_x & D_z E_x \\ D_x E_y & D_y E_y - \frac{1}{2}\varepsilon_0 E^2 & D_z E_y \\ D_x E_z & D_y E_z & D_z E_z - \frac{1}{2}\varepsilon_0 E^2 \end{pmatrix}. && (2.30) \end{aligned}$$

The electric force acting on a volume V is:

$$\vec{F_e} = \iint_{\partial V} \begin{pmatrix} \left(\vec{D}\cdot\vec{n}\right)E_x - \frac{\varepsilon_0}{2}E^2 n_x \\ \left(\vec{D}\cdot\vec{n}\right)E_y - \frac{\varepsilon_0}{2}E^2 n_y \\ \left(\vec{D}\cdot\vec{n}\right)E_z - \frac{\varepsilon_0}{2}E^2 n_z \end{pmatrix}^* dS = \iint_{\partial V} \left(\left(\vec{D}\cdot\vec{n}\right)\vec{E} - \frac{\varepsilon_0}{2}E^2\vec{n}\right)^* dS. \tag{2.31}$$

In (2.31), $*$ indicates that these quantities are generally discontinuous at the interface between two dielectrics (such at the droplet surface). The surface integral in (2.31) is not well defined. Thus, calculating electric forces from the stress tensor requires special treatment.
The integrand in (2.31) corresponds to the following surface force density:

$$\vec{f_s} = \left(\vec{D} \cdot \vec{n}\right) \vec{E} - \frac{\varepsilon_0}{2} E^2 \vec{n}. \tag{2.32}$$

We consider two dielectric materials V_1 and V_2 of respective permittivities ε_1 and ε_2 as shown in Figure 2.2. Their interface is denoted $I = V_1 \cap V_2$ and is oriented by the normal $\vec{n}$ going from V_1 to V_2 and by the two orthonormal vectors $\vec{\tau_i}$ and $\vec{\tau_j}$ tangential to the interface.

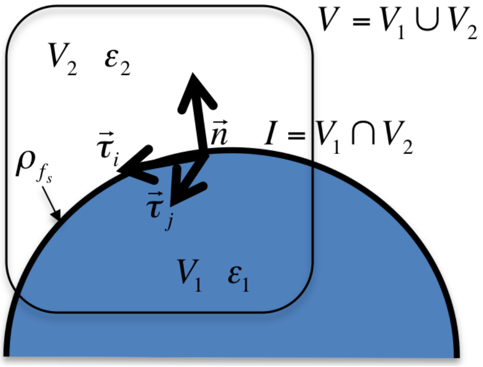

Figure 2.2.: Gaussian pillbox V across two dielectric materials.

The surface force density acting on the surface of the Gaussian pillbox is zero except at the interface I between the two dielectric materials. This is calculated in the following by applying the Gauss theorem to (2.31) and the Gaussian pillbox V.
The tangential component of the surface force density acting on the surface $V_1 \cap V_2$ is:

$$\left(\vec{f_{s_1}} + \vec{f_{s_2}}\right) \cdot \vec{\tau} = \left(\vec{D_1} \cdot \vec{n}\right) \vec{E_1} \cdot \vec{\tau} - \left(\vec{D_2} \cdot \vec{n}\right) \vec{E_2} \cdot \vec{\tau}, \tag{2.33}$$

where $\vec{\tau}$ stands for either $\vec{\tau_i}$ or $\vec{\tau_j}$.
The continuity condition of the displacement flux density is:

$$\vec{D_1} \cdot \vec{n} - \vec{D_2} \cdot \vec{n} = \varrho_{f_s}. \tag{2.34}$$

where ϱ_{f_s} is the free surface charge density. The continuity condition of the electric field is:

$$\vec{E_1} \cdot \vec{\tau} = \vec{E_2} \cdot \vec{\tau}. \tag{2.35}$$

Therefore:

$$\left(\vec{f_{s_1}} + \vec{f_{s_2}}\right) \cdot \vec{\tau} = \varrho_{f_s} \vec{E_1} \cdot \vec{\tau} = \varrho_{f_s} \vec{E_2} \cdot \vec{\tau}. \tag{2.36}$$

The surface force density has no tangential component at material interfaces in the absence of free surface charge:

$$\left(\vec{f_{s_1}} + \vec{f_{s_2}}\right) \cdot \vec{\tau} \quad = \quad 0. \tag{2.37}$$

The normal component of the surface force density acting on material 1 and material 2 is:

$$\left(\vec{f}_{s_1}+\vec{f}_{s_2}\right)\cdot\vec{n}=\left(\vec{D}_1\cdot\vec{n}\right)\vec{E}_1\cdot\vec{n}-\left(\vec{D}_2\cdot\vec{n}\right)\vec{E}_2\cdot\vec{n}+\frac{\varepsilon_0}{2}\left(E_2^2-E_1^2\right). \tag{2.38}$$

We introduce the following notations for the electric field components at the interface $I=V_1\cap V_2$:

$$E_{\tau_1}^2=\left(\vec{E}_1\cdot\vec{\tau}_i\right)^2+\left(\vec{E}_1\cdot\vec{\tau}_j\right)^2,\ E_{\tau_2}^2=\left(\vec{E}_2\cdot\vec{\tau}_i\right)^2+\left(\vec{E}_2\cdot\vec{\tau}_j\right)^2. \tag{2.39}$$

$$E_{n_1}^2=\left(\vec{E}_1\cdot\vec{n}\right)^2,\ E_{n_2}^2=\left(\vec{E}_2\cdot\vec{n}\right)^2. \tag{2.40}$$

The continuity conditions (2.34) and (2.35) yield:

$$D_{n_1}=D_{n_2}+\varrho_{f_s}\ \text{ and }\ E_{\tau_1}^2=E_{\tau_2}^2. \tag{2.41}$$

Therefore:

$$\left(\vec{f}_{s_1}+\vec{f}_{s_2}\right)\cdot\vec{n} = D_{n_1}E_{n_1}-D_{n_2}E_{n_2}+\frac{\varepsilon_0}{2}\left(E_{n_2}^2-E_{n_1}^2\right). \tag{2.42}$$

$$\left(\vec{f}_{s_1}+\vec{f}_{s_2}\right)\cdot\vec{n} = \varrho_{f_s}E_{n_1}+\left(E_{n_1}-E_{n_2}\right)D_{n_2}+\varepsilon_0\left(E_{n_2}-E_{n_1}\right)\frac{\left(E_{n_2}+E_{n_1}\right)}{2}. \tag{2.43}$$

$$\left(\vec{f}_{s_1}+\vec{f}_{s_2}\right)\cdot\vec{n} = \varrho_{f_s}E_{n_1}+\left(E_{n_1}-E_{n_2}\right)\left(\varepsilon_2E_{n_2}-\varepsilon_0\frac{\left(E_{n_2}+E_{n_1}\right)}{2}\right). \tag{2.44}$$

$$\left(\vec{f}_{s_1}+\vec{f}_{s_2}\right)\cdot\vec{n} = \varrho_{f_s}E_{n_1}+\left(E_{n_1}-E_{n_2}\right)\left(\frac{\varepsilon_2E_{n_2}+\varepsilon_1E_{n_1}-\varrho_{f_s}}{2}-\varepsilon_0\frac{\left(E_{n_2}+E_{n_1}\right)}{2}\right). \tag{2.45}$$

$$\left(\vec{f}_{s_1}+\vec{f}_{s_2}\right)\cdot\vec{n} = \varrho_{f_s}\frac{E_{n_1}+E_{n_2}}{2}+\left(E_{n_1}-E_{n_2}\right)\frac{\left(\varepsilon_2-\epsilon_0\right)E_{n_2}+\left(\varepsilon_1-\epsilon_0\right)E_{n_1}}{2}. \tag{2.46}$$

$$\left(\vec{f}_{s_1}+\vec{f}_{s_2}\right)\cdot\vec{n} = \varrho_{f_s}\frac{E_{n_1}+E_{n_2}}{2}+\frac{P_{n_2}+P_{n_1}}{2}\left(E_{n_1}-E_{n_2}\right). \tag{2.47}$$

where $\vec{P}=\left(\varepsilon-\varepsilon_0\right)\vec{E}$ is the dielectric polarization density and $P_n=\vec{P}\cdot\vec{n}$.
The first term corresponds to the action of the averaged electric fields on the free surface charges and the second term to the action of the electric field on the averaged electric dipole density. This is consistent with the expression of the volume force density derived in (2.10) from the Kelvin force polarization density:

$$\vec{f}_e=\varrho_f\vec{E}+\left(\vec{P}\cdot\vec{\nabla}\right)\vec{E}. \tag{2.48}$$

2.1.3.1 The Maxwell stress tensor for incompressible flow

We saw in the previous sections that the electric force density (2.10) could be expressed as the sum of a conservative and non conservative term:

$$\vec{f}_e=\varrho_f\vec{E}+\frac{1}{2}\vec{\nabla}\left(\left(\varepsilon-\varepsilon_0\right)\vec{E}\cdot\vec{E}\right)-\frac{1}{2}\left(\vec{E}\cdot\vec{E}\right)\vec{\nabla}\varepsilon \tag{2.49}$$

In section 2.2, we will show that in the case of an incompressible flow the conservative term can be dropped as it gives no contribution to the fluid flow. The relevant electric force density becomes:

$$\vec{f}_e = \varrho_f \vec{E} - \frac{1}{2}\left(\vec{E}\cdot\vec{E}\right)\vec{\nabla}\varepsilon. \tag{2.50}$$

which is equivalent to:

$$\vec{f}_e \;=\; \mathsf{div}\begin{pmatrix} D_x E_x - \varepsilon_0\frac{E^2}{2} & D_y E_x & D_z E_x \\ D_x E_y & D_y E_y - \varepsilon_0\frac{E^2}{2} & D_z E_y \\ D_x E_z & D_y E_z & D_z E_z - \varepsilon_0\frac{E^2}{2} \end{pmatrix} - \frac{1}{2}\vec{\nabla}\left(\left(\varepsilon-\varepsilon_0\right)E^2\right). \tag{2.51}$$

Rearranging terms, we finally obtain,

$$\vec{f}_e \;=\; \mathsf{div}\begin{pmatrix} D_x E_x - \varepsilon\frac{E^2}{2} & D_y E_x & D_z E_x \\ D_x E_y & D_y E_y - \varepsilon\frac{E^2}{2} & D_z E_y \\ D_x E_z & D_y E_z & D_z E_z - \varepsilon\frac{E^2}{2} \end{pmatrix}. \tag{2.52}$$

This expression is similar (but not identical) to the force density derived from the Maxwell stress tensor (2.30) .
The electric force acting on a volume V is:

$$\vec{F}_e = \iiint_V \vec{f}_e dV = \iint_{\partial V}\begin{pmatrix} \bigl(D_x E_x - \frac{1}{2}\varepsilon E^2 & D_y E_x & D_z E_x\bigr)^* \cdot\vec{n} \\ \bigl(D_x E_y & D_y E_y - \frac{1}{2}\varepsilon E^2 & D_z E_y\bigr)^* \cdot\vec{n} \\ \bigl(D_x E_z & D_y E_z & D_z E_z - \frac{1}{2}\varepsilon E^2\bigr)^* \cdot\vec{n} \end{pmatrix} dS. \tag{2.53}$$

where *, again indicates that those quantities are generally discontinuous across the dielectric surface. Furthermore,

$$\vec{F}_e = \iint_{\partial V}\begin{pmatrix} \left(\vec{D}\cdot\vec{n}\right)E_x - \frac{\varepsilon}{2}E^2 n_x \\ \left(\vec{D}\cdot\vec{n}\right)E_y - \frac{\varepsilon}{2}E^2 n_y \\ \left(\vec{D}\cdot\vec{n}\right)E_z - \frac{\varepsilon}{2}E^2 n_z \end{pmatrix}^* dS = \iint_{\partial V}\left(\left(\vec{D}\cdot\vec{n}\right)\vec{E} - \frac{\varepsilon}{2}E^2\vec{n}\right)^* dS. \tag{2.54}$$

The integrand in (2.54) corresponds to the following surface force density:

$$\vec{f}_s = \left(\vec{D}\cdot\vec{n}\right)\vec{E} - \frac{\varepsilon}{2}E^2\vec{n}. \tag{2.55}$$

We consider two dielectric materials V_1 and V_2 of respective permittivities ε_1 and ε_2 as shown in Figure 2.2. Their interface is denoted $I = V_1 \cap V_2$ and is oriented by the normal $\vec{n}$ going from V_1 to V_2 and by the tangential vectors $\vec{\tau}_i$ and $\vec{\tau}_j$.
The surface force density acting on I is calculated by applying the Gauss theorem to (2.54) for the Gaussian pillbox V. The tangential component of the surface force density acting on the surface ∂V is

$$\left(\vec{f}_{s_1} + \vec{f}_{s_2}\right)\cdot\vec{\tau} = \left(\vec{D}_1\cdot\vec{n}\right)\vec{E}_1\cdot\vec{\tau} - \left(\vec{D}_2\cdot\vec{n}\right)\vec{E}_2\cdot\vec{\tau}. \tag{2.56}$$

The continuity condition of the displacement flux density is:

$$\vec{D_1}\cdot\vec{n} - \vec{D_2}\cdot\vec{n} = \varrho_{f_s}, \tag{2.57}$$

where ϱ_{f_s} is the free surface charge density.
The continuity condition of the electric field is:

$$\vec{E_1}\cdot\vec{\tau} = \vec{E_2}\cdot\vec{\tau}. \tag{2.58}$$

Therefore :

$$\left(\vec{f_{s_1}} + \vec{f_{s_2}}\right)\cdot\vec{\tau} = \varrho_{f_s}\vec{E_1}\cdot\vec{\tau} = \varrho_{f_s}\vec{E_2}\cdot\vec{\tau}. \tag{2.59}$$

Thus, the surface force density has no tangential component at material interfaces in the absence of free surface charge:

$$\left(\vec{f_{s_1}} + \vec{f_{s_2}}\right)\cdot\vec{\tau} \;=\; 0. \tag{2.60}$$

The normal component of the surface force density acting on the material 1 and material 2 is:

$$\left(\vec{f_{s_1}} + \vec{f_{s_2}}\right)\cdot\vec{n} = \left(\vec{D_1}\cdot\vec{n}\right)\vec{E_1}\cdot\vec{n} - \left(\vec{D_2}\cdot\vec{n}\right)\vec{E_2}\cdot\vec{n} + \left(\varepsilon_2\frac{E_2^2}{2} - \varepsilon_1\frac{E_1^2}{2}\right). \tag{2.61}$$

We denote $\vec{\tau_i}$ and $\vec{\tau_j}$ two orthonormal vectors tangent to the interface $I = V_1 \cap V_2$ and

$$E_{\tau_1}^2 = \left(\vec{E_1}\cdot\vec{\tau_i}\right)^2 + \left(\vec{E_1}\cdot\vec{\tau_j}\right)^2 \,,\, E_{\tau_2}^2 = \left(\vec{E_2}\cdot\vec{\tau_i}\right)^2 + \left(\vec{E_2}\cdot\vec{\tau_j}\right)^2. \tag{2.62}$$

$$E_{n_1}^2 = \left(\vec{E_1}\cdot\vec{n}\right)^2 \,,\, E_{n_2}^2 = \left(\vec{E_2}\cdot\vec{n}\right)^2. \tag{2.63}$$

The continuity conditions (2.57) and (2.58) yield:

$$D_{n_1} = D_{n_2} + \varrho_{f_s} \text{ and } E_{\tau_1}^2 = E_{\tau_2}^2. \tag{2.64}$$

Therefore:

$$\left(\vec{f_{s_1}} + \vec{f_{s_2}}\right)\cdot\vec{n} \;=\; D_{n_1}E_{n_1} - D_{n_2}E_{n_2} + \left(\varepsilon_2\frac{E_2^2}{2} - \varepsilon_1\frac{E_1^2}{2}\right). \tag{2.65}$$

$$\left(\vec{f_{s_1}} + \vec{f_{s_2}}\right)\cdot\vec{n} \;=\; D_{n_1}E_{n_1} - D_{n_2}E_{n_2} + \frac{1}{2}\left(\varepsilon_2 E_{n_2}^2 - \varepsilon_1 E_{n_1}^2\right) + \frac{1}{2}\left(\varepsilon_2 - \varepsilon_1\right)E_{\tau_2}^2. \tag{2.66}$$

$$\left(\vec{f_{s_1}} + \vec{f_{s_2}}\right)\cdot\vec{n} \;=\; \frac{1}{2}\left(\varrho_{f_s}E_{n_1} + \left(E_{n_1} - E_{n_2}\right)\varepsilon_2 E_{n_2}\right) + \frac{1}{2}\left(\varepsilon_2 - \varepsilon_1\right)E_{\tau_2}^2. \tag{2.67}$$

$$\left(\vec{f_{s_1}} + \vec{f_{s_2}}\right)\cdot\vec{n} \;=\; \frac{1}{2}\left(\varrho_{f_s}E_{n_1} + \left(E_{n_1} - E_{n_2}\right)\left(\varepsilon_1 E_{n_1} - \varrho_{f_s}\right)\right) + \frac{1}{2}\left(\varepsilon_2 - \varepsilon_1\right)E_{\tau_2}^2. \tag{2.68}$$

$$\left(\vec{f_{s_1}} + \vec{f_{s_2}}\right)\cdot\vec{n} \;=\; \varrho_{f_s}\frac{E_{n_1} + E_{n_2}}{2} + \frac{1}{2}\left(\varepsilon_2 - \varepsilon_1\right)\left(E_{\tau_2}^2 + E_{n_1}E_{n_2}\right). \tag{2.69}$$

$$\left(\vec{f_{s_1}} + \vec{f_{s_2}}\right)\cdot\vec{n} \;=\; \varrho_{f_s}\frac{E_{n_1} + E_{n_2}}{2} - \frac{1}{2}\left(\vec{E_1}\cdot\vec{E_2}\right)\left(\varepsilon_1 - \varepsilon_2\right). \tag{2.70}$$

The first term corresponds to the action of the averaged electric fields on the free surface charge as found in (2.47) for the general case. The second term is the contribution of $-\frac{1}{2}\left(\vec{E}\cdot\vec{E}\right)\vec{\nabla}\varepsilon$ in (2.50).

We showed in the previous sections that in absence of electrostriction, the electric force density acting on an isotropic linear dielectric medium could be derived either from the Kelvin force polarization density or from the principle of virtual work and the Korteweg-Helmholtz force density. In addition different expressions can be derived depending on the spatial differentiability of the permittivity. This force can be written as the sum of a conservative and non conservative term. For the simulation of a compressible flow both terms must be used as source terms in the momentum equation whereas in the case of incompressible flows the conservative term can be dropped without impacting the fluid motion. In both cases the electric force acting on a dielectric medium can be calculated by only considering the normal surface force. The different forces acting on the droplet according to Table 2.1 and Table 2.2 are presented in Figure 2.3 :

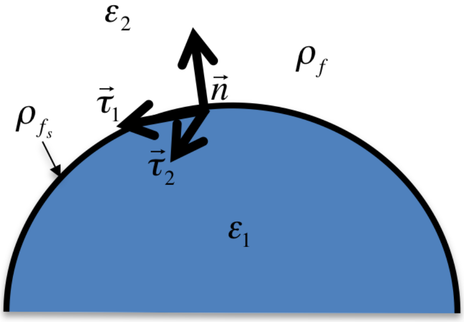

Figure 2.3.: Interface between two dielectric media ε_1 and ε_2 in presence of free charge ϱ_f and free surface charge ϱ_{f_s}.

In the absence of free charge, the surface force densities acting at an interface have only a normal component. The volume force and surface force densities with their associated Maxwell stress tensors are summarized for the general case in Table 2.1 and for incompressible flows only in Table 2.2.

	Compressible and incompressible flows
Constitutive law	$\vec{D} = \varepsilon \vec{E}$
Volume force densities	$\vec{f}_v = \varrho_f \vec{E} + \left(\left(\varepsilon - \varepsilon_0 \right) \vec{E} \cdot \vec{\nabla} \right) \vec{E} = \varrho_f \vec{E} + \frac{1}{2} \left(\varepsilon - \varepsilon_0 \right) \vec{\nabla} \left(\vec{E} \cdot \vec{E} \right)$
Maxwell Stress Tensor	$\mathsf{T} = \begin{pmatrix} D_x E_x - \varepsilon_0 \frac{E^2}{2} & D_y E_x & D_z E_x \\ D_x E_y & D_y E_y - \varepsilon_0 \frac{E^2}{2} & D_z E_y \\ D_x E_z & D_y E_z & D_z E_z - \varepsilon_0 \frac{E^2}{2} \end{pmatrix}$
Surface force densities	$\vec{f}_s \cdot \vec{\tau} = \varrho_{f_s} \vec{E}_1 \cdot \vec{\tau} = \varrho_{f_s} \vec{E}_2 \cdot \vec{\tau}$ $\vec{f}_s \cdot \vec{n}_{1 \to 2} = \varrho_{f_s} \frac{\vec{E}_1 \cdot \vec{n} + \vec{E}_2 \cdot \vec{n}}{2} + \frac{\left(\varepsilon_1 - \varepsilon_0 \right) \vec{E}_1 \cdot \vec{n} + \left(\varepsilon_2 - \varepsilon_0 \right) \vec{E}_2 \cdot \vec{n}}{2} \left(\vec{E}_1 \cdot \vec{n} - \vec{E}_2 \cdot \vec{n} \right)$

Table 2.1.: Forces and stress tensor for dielectrics (without electrostriction) in the general case.

	Incompressible flows
Constitutive law	$\vec{D} = \varepsilon \vec{E}$ and ε spatially differentiable
Volume force densities	$\vec{f_v} = \varrho_f \vec{E} - \frac{1}{2}\left(\vec{E}\cdot\vec{E}\right)\vec{\nabla}\varepsilon$
Maxwell Stress Tensor	$\mathsf{T}' = \begin{pmatrix} D_x E_x - \varepsilon \frac{E^2}{2} & D_y E_x & D_z E_x \\ D_x E_y & D_y E_y - \varepsilon \frac{E^2}{2} & D_z E_y \\ D_x E_z & D_y E_z & D_z E_z - \varepsilon \frac{E^2}{2} \end{pmatrix}$
Surface force densities	$\vec{f_s}\cdot\vec{\tau} = \varrho_{f_s}\vec{E_1}\cdot\vec{\tau} = \varrho_{f_s}\vec{E_2}\cdot\vec{\tau}$ $\vec{f_s}\cdot\vec{n}_{1\to 2} = \varrho_{f_s}\frac{\vec{E_1}\cdot\vec{n}+\vec{E_2}\cdot\vec{n}}{2} - \frac{1}{2}\left(\vec{E_1}\cdot\vec{E_2}\right)\left(\varepsilon_1 - \varepsilon_2\right)$

Table 2.2.: Forces and stress tensor for dielectrics (without electrostriction) for incompressible flows.

2.2 The fluid dynamics model

The simulation of water droplet vibrations in the presence of electric field is modeled as a two phase flow problem. The dimensionless Reynolds number for this problem is:

$$R_e = \frac{vL}{\mu} \simeq 10000 >> 1, \tag{2.71}$$

where $v = 1m/s$ is the maximum water velocity, $L = 0.01m$ is the maximum droplet size and $\mu = 1.10^{-6}m^2/s$ is the water kinematic viscosity at 20 °Celsius. For large Reynolds numbers, surface tension effects are estimated based on the dimensionless Weber number which measures the relative importance of the fluid's inertia compared to its surface tension:

$$W_e = \frac{\varrho L v^2}{\sigma_s} \simeq 3 \approx 1, \tag{2.72}$$

where $\sigma_s = 0.07N/m$ is the surface tension, $v = 0.2m/s$ is the typical water velocity, $\varrho = 1000kg/m^3$ is the water mass density and $L = 5.10^{-3}m$ is the typical droplet size. The small Weber number indicates that the problem is dominated by surface tension effects. The latter combines the effect of the inward inter-molecular attractive force with the radially outward pressure gradient force across the surface. In this model we assume that the surface tension is uniform and constant in time. The incompressibility assumption holds for water meaning that the effect of the pressure on the density is small enough to be considered negligible. It also holds for air at ambient temperature and for velocity lower than 0.3 Mach [11]. The Navier-Stokes equations for incompressible flow describing the air-water flow system are:

$$\begin{aligned} \frac{\partial \varrho\vec{u}}{\partial t} + \vec{\nabla}\cdot\left(\varrho\vec{u}\vec{u}\right) - \mathsf{div}\left(\mathsf{T_v}\right) &= -\vec{\nabla}p + \varrho\vec{g} + \vec{f_s} + \vec{f_e}, & (2.73) \\ \mathsf{T_v} &= \mu\left(\vec{\nabla}\vec{u} + {}^t\vec{\nabla}\vec{u}\right), & (2.74) \\ \vec{\nabla}\cdot\vec{u} &= 0, & (2.75) \end{aligned}$$

where $\vec{u}$ is the fluid velocity, p is the pressure, ϱ is the mass density, μ is the dynamic viscosity, T_v is the stress deviator tensor, $\vec{g}$ is the gravitational force density, $\vec{f}_s$ is the water droplet surface tension force. The electrical problem and the fluid dynamics problem are coupled through the electric force density $\vec{f}_e$ added as a source term to the momentum equation (2.73). As shown in the previous sections, the electric force density can be expressed as the sum of a conservative and non conservative terms:

$$\vec{f}_e = \varrho_f \vec{E} + \frac{1}{2}\vec{\nabla}\left(\left(\varepsilon - \varepsilon_0\right)\vec{E}^2\right) - \frac{1}{2}\left(\vec{E}^2\right)\vec{\nabla}\varepsilon. \tag{2.76}$$

Therefore the momentum equation becomes:

$$\begin{aligned}
\frac{\partial \varrho \vec{u}}{\partial t} + \vec{\nabla}\cdot\left(\varrho\vec{u}\vec{u}\right) - \mathsf{div}\left(\mathsf{T}_\mathsf{v}\right) &= \vec{\nabla}\left(\left(\varepsilon - \varepsilon_0\right)\frac{\vec{E}^2}{2} - p\right) + \varrho\vec{g} + \vec{f}_s + \varrho_f\vec{E} - \frac{\vec{E}^2}{2}\vec{\nabla}\varepsilon, \quad (2.77)\\
\mathsf{T}_\mathsf{v} &= \mu\left(\vec{\nabla}\vec{u} + {}^t\vec{\nabla}\vec{u}\right), \quad (2.78)\\
\vec{\nabla}\cdot\vec{u} &= 0, \quad (2.79)
\end{aligned}$$

which is equivalent to:

$$\begin{aligned}
\frac{\partial \varrho \vec{u}}{\partial t} + \vec{\nabla}\cdot\left(\varrho\vec{u}\vec{u}\right) - \mathsf{div}\left(\mathsf{T}_\mathsf{v}\right) &= -\vec{\nabla}p' + \varrho\vec{g} + \vec{f}_s + \varrho_f\vec{E} - \frac{\vec{E}^2}{2}\vec{\nabla}\varepsilon, \quad (2.80)\\
\mathsf{T}_\mathsf{v} &= \mu\left(\vec{\nabla}\vec{u} + {}^t\vec{\nabla}\vec{u}\right), \quad (2.81)\\
\vec{\nabla}\cdot\vec{u} &= 0, \quad (2.82)
\end{aligned}$$

where $p' = p - \frac{1}{2}\left(\varepsilon - \varepsilon_0\right)\vec{E}^2$ is a modified pressure including electric field pressure stemming from the conservative term of the electric force. Thus, this part of the electric force density can be dropped in the incompressible case yielding an effective force density of:

$$\vec{f}_e = \varrho_f\vec{E} - \frac{1}{2}\left(\vec{E}^2\right)\vec{\nabla}\varepsilon. \tag{2.83}$$

According to (2.52), this force density can be derived from a modified Maxwell Stress Tensor:

$$\mathsf{T}' = \begin{pmatrix} D_x E_x - \varepsilon\frac{E^2}{2} & D_y E_x & D_z E_x \\ D_x E_y & D_y E_y - \varepsilon\frac{E^2}{2} & D_z E_y \\ D_x E_z & D_y E_z & D_z E_z - \varepsilon\frac{E^2}{2} \end{pmatrix}, \quad \vec{f}_e = \mathsf{div}\mathsf{T}'. \tag{2.84}$$

3 The finite element method on a moving mesh

3.1 The physical model

A model consisting of a single water droplet lying on a planar insulator block located between two electrodes is used to investigate the droplet oscillations in a strong electric field. Figure 3.1 shows two arrangements of a water droplet on an insulating surface placed in a horizontal (left) and vertical (right) externally applied electric field, respectively. In the horizontal field configuration two cylindrical high voltage electrodes are embedded in an insulating plate at opposite sides [12, 13] and generate a nearly horizontal electric field at the droplet location. To generate a vertical field stress, two circular electrodes are embedded in an insulating material and arranged in a certain distance to each other, thus, providing a small air gap. Embedding the electrodes in the insulator avoids partial discharges occurring at the edges or flashovers between the electrodes. The gap distance can easily be changed to adjust the appropriate E-field at the water droplet. In order to obtain the same electric field stress at both horizontal and vertical arrangements, the applied voltage (RMS value) between the electrodes is $7.5kV$ and $3.35kV$ in the horizontal and the vertical configuration, respectively.

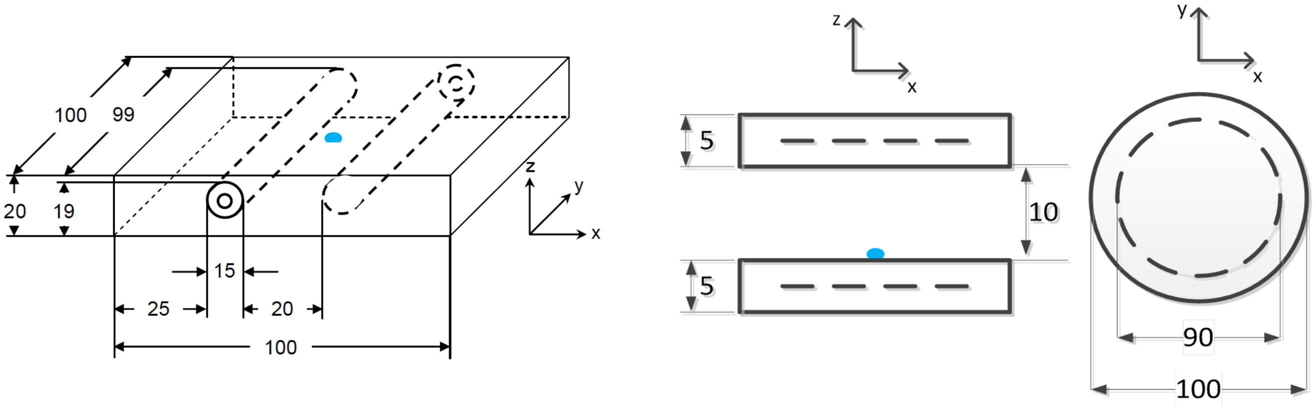

Figure 3.1.: Experimental arrangements (dimensions in mm) generating a horizontal (left) and vertical (right) electric field, (images from [13])

3.2 The computational model

The computational model corresponding to the cases where the electric field is oriented parallel and normal to the insulator surface, respectively, is shown in Figure 3.2. It includes the pair of electrodes, the droplet, the polymer block and the surrounding air. Dirichlet boundary

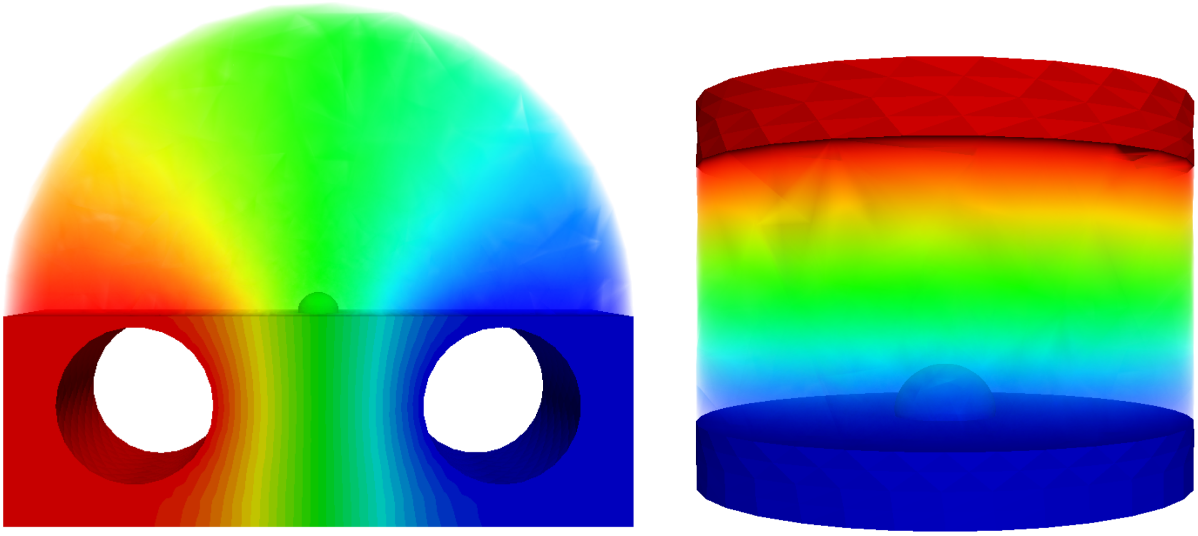

Figure 3.2.: Model corresponding to horizontal (left) and vertical (right) field set-ups. The electric scalar potential is shown. Solid colors are used to identify the polymer and the droplet.

conditions set the potential on the electrodes whereas Neumann boundary conditions close the rest of the computational domain.

Figure 3.3 shows the simulated electric field strength resulting for the two configurations when no water droplet is present. As can be seen, the externally applied electric field for both horizontal and vertical field configurations, in the area between electrodes, has approximately the same value of $4.25 kV/cm$.

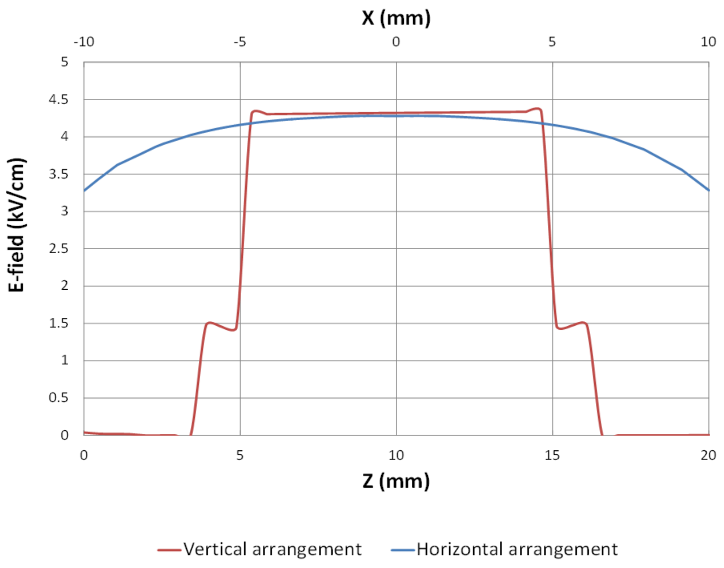

Figure 3.3.: Simulated electric field stress without water droplet for an applied voltage of $7.5 kV$ for the horizontal and of $3.35 kV$ for the vertical field configuration, respectively.

We assume in the following that while the droplet changes shape, it does not break-up into smaller droplets. Thus, the topology of the phase boundary remains the same. An efficient discretization approach for this case can be obtained by keeping the mesh connectivity which avoids costly remeshing operations. Figure 3.4 shows how the mesh elements of the water droplet mesh are deformed to match the time dependent droplet shape.

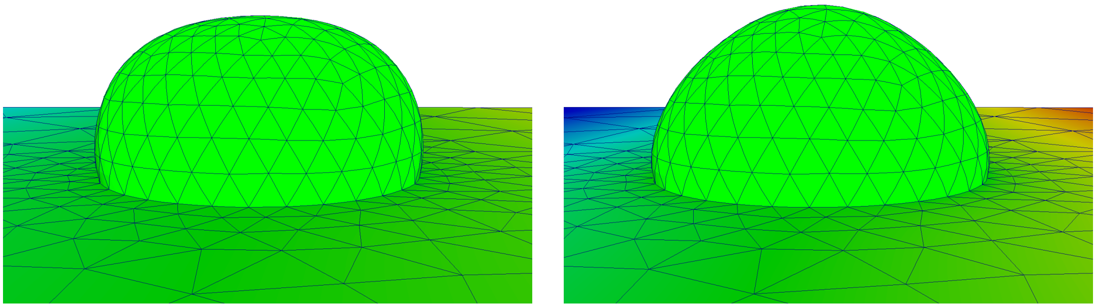

Figure 3.4.: Snapshots at two different instants of the water droplet and insulator surface meshes in the horizontal field configuration. The mesh elements are deformed to match the changing droplet shape.

3.3 Time discretization

We showed in chapter 2.1 that the electro-quasistatic equation (2.2) described the time evolution of the potential in the vibrating droplet. It is integrated in time over an elementary time step as follows:

$$\int_{t_n}^{t_{n+1}} -\vec{\nabla}\cdot\left(\left.\frac{\partial \epsilon\vec{\nabla}V}{\partial t}\right|_{x,y,z}\right) dt \quad = \quad -\left[\vec{\nabla}\cdot\left(\epsilon\vec{\nabla}V\right)\right]_{t_n}^{t_{n+1}} = \int_{t_n}^{t_{n+1}} \vec{\nabla}\cdot\left(\sigma\vec{\nabla}V\right) dt. \tag{3.1}$$

Applying the trapezoid rule to the right-hand side of (3.1) yields the Crank-Nicolson scheme [14]:

$$\left[\vec{\nabla}\cdot\left(\epsilon\vec{\nabla}V\right)\right]_{t_n}^{t_{n+1}} \quad = \quad -\frac{\mathrm{dt}}{2}\left(\vec{\nabla}\cdot\left(\sigma\vec{\nabla}V\right)\Big|^{n} + \vec{\nabla}\cdot\left(\sigma\vec{\nabla}V\right)\Big|^{n+1}\right). \tag{3.2}$$

Finally, we obtain the following time stepping scheme:

$$-\vec{\nabla}\cdot\left(\left(\epsilon+\frac{\sigma\mathrm{dt}}{2}\right)\vec{\nabla}V\right)\Bigg|^{n+1} \quad = \quad -\vec{\nabla}\cdot\left(\left(\epsilon-\frac{\sigma\mathrm{dt}}{2}\right)\vec{\nabla}V\right)\Bigg|^{n}, \tag{3.3}$$

with the constant time step $\mathrm{dt} = t_{n+1} - t_n$. Assuming that the high voltage field is switched at $t_0 = 0$, the initial potential distribution is $V|_0 = 0$.
On a fixed mesh and for linear problems, the Crank Nicolson scheme (3.3) has a second-order truncation error and is unconditionally stable [15].

3.4 Spatial discretization

We denote $\Omega \subset \mathbb{R}^3$ the bounded domain corresponding to the computational domain and $L^2(\Omega)$ the Hilbert space of square integrable real-valued functions defined over Ω:

$$\begin{aligned} L^2(\Omega) &= \left\{ f:\Omega \rightarrow \mathbb{R} \mid \langle f,f\rangle = \int_\Omega |f|^2 d\Omega < \infty \right\} \text{ endowed with,} && (3.4)\\ \langle f,g\rangle &= \int_\Omega f g d\Omega\,. && (3.5)\end{aligned}$$

$L^2(\Omega)$ contains all piecewise continuous functions defined over Ω. In order to find a suitable space to represent the potential we must further restrict $L^2(\Omega)$ to the functions having also a square integrable gradient:

$$\begin{aligned} H^1(\Omega) &= \left\{ f \in L^2(\Omega),\ \frac{\partial f}{\partial x_i} \in L^2(\Omega),\ 1 \le i \le 3 \right\} \text{ endowed with,} && (3.6)\\ \langle f,g\rangle_{H^1(\Omega)} &= \int_\Omega f g + \sum_{i=1}^{3} \frac{\partial f}{\partial x_i}\frac{\partial g}{\partial x_i} d\Omega\,. && (3.7)\end{aligned}$$

We define the linear differential operator corresponding to the div-grad operator in H^1.

$$\begin{aligned} \mathsf{A}_\alpha : H^1(\Omega) &\rightarrow L^2(\Omega) && (3.8)\\ \mathsf{A}_\alpha V &= -\vec{\nabla}\cdot\left(\alpha\vec{\nabla}V\right)\,. && (3.9)\end{aligned}$$

Then, at each time step t_{n+1} one needs to solve the following boundary-value problem:

$$\begin{aligned} \mathsf{A}_{\epsilon+\frac{\sigma \mathrm{dt}}{2}} V\Big|^{n+1} &= \mathsf{A}_{\epsilon-\frac{\sigma \mathrm{dt}}{2}} V\Big|^{n} = B|^n\,, && (3.10)\\ V|^{n+1} &= V_b\left(t_{n+1}\right) \text{ on } \Gamma_D\,, && (3.11)\\ \frac{\partial V}{\partial n}\Big|^{n+1} &= 0 \text{ on } \Gamma_N\,, && (3.12)\end{aligned}$$

with Γ_D and Γ_N denoting boundaries where Dirichlet boundary conditions and Neumann boundary conditions, respectively, are enforced and where $V_b(t)$ is the potential enforced on Γ_D. The linear differential operator A_α and the associated problem are strongly elliptic for $\alpha > 0$. According to Céa's lemma [16], this property ensures that a finite element approximation of the solution based on the Galerkin method converges at every time step toward the unique solution of the electro-quasistatic problem (3.10).

3.4.1 The weak solution

In order to find a finite element approximation of the solution at the time step $n+1$, we build a finite element partition of the computation domain $\Omega|_h^{n+1}$ parametrized by the maximum element length h. The solution V of the problem 3.10 belongs to $H^1\left(\Omega|^{n+1}\right)$ and is approximated by $V_h \in H^1\left(\Omega|_h^{n+1}\right)$. The restriction of V_h on each finite element is a linear combination of m shape functions $\varphi_i \in H^1\left(\Omega|_h^{n+1}\right)$ such that:

$$V_h = \sum_{i=1}^{m} v_i \varphi_i\,, \tag{3.13}$$

where (v_i) are the potential degrees of freedom.
The problem of finding $V_h \in H^1\left(\Omega|_h^{n+1}\right)$ such that:

$$\langle \varphi_j, \mathsf{A}_{\epsilon+\frac{\sigma \mathrm{dt}}{2}}\Big|^{n+1} V_h\rangle = \langle \varphi_j, B|_h^n\rangle \text{ for all } \varphi_j \in H^1\left(\Omega|_h^{n+1}\right) , \tag{3.14}$$

$$\sum_{i=1}^{m}\langle \varphi_j, \mathsf{A}_{\epsilon+\frac{\sigma \mathrm{dt}}{2}}\Big|^{n+1} \varphi_i\rangle v_i = \langle \varphi_j, B|_h^n\rangle \text{ for all } \varphi_j \in H^1\left(\Omega|_h^{n+1}\right) , \tag{3.15}$$

has a unique solution V_h which is the best fit to V with respect to the energy norm $\|.\|_{H^1\left(\Omega|^{n+1}\right)}$:

$$\|V - V_h\|_{H^1\left(\Omega|^{n+1}\right)} \leq C \min_{s_h \in H^1\left(\Omega|_h^{n+1}\right)} \|V - s_h\|_{H^1\left(\Omega|^{n+1}\right)} , \tag{3.16}$$

with C a positive constant. In addition, in the case of a smooth solution V approximated by polynomial shape functions $\{\varphi_i\}_{i=1,m}$ forming a complete polynomial basis of degree d, we have [17] :

$$\|V - V_h\|_{L^2\left(\Omega|^{n+1}\right)} = O\left(h^{d+1}\right) \quad \text{when} \quad h \to 0 \, . \tag{3.17}$$

It is important to note that since the shape functions belongs to $H^1\left(\Omega|_h^{n+1}\right)$ the test functions must also belong to $H^1\left(\Omega|_h^{n+1}\right)$ which implies that the weak formulation must be carried out in $\Omega|_h^{n+1}$.

3.4.2 The weak solution on a moving mesh

We denote $\Omega_1 = \Omega|_h^n$, $\Omega_2 = \Omega|_h^{n+1}$, $\partial\Omega_1 = \partial\Omega|_h^n$ and $\partial\Omega_2 = \partial\Omega|_h^{n+1}$. We associate the triangulations (curvilinear tetrahedral meshes) T_1 to Ω_1 and T_2 to Ω_2. In Figure 3.5 we show how the mesh T_1 is deformed into T_2 to conform to the moving interface between water and air.

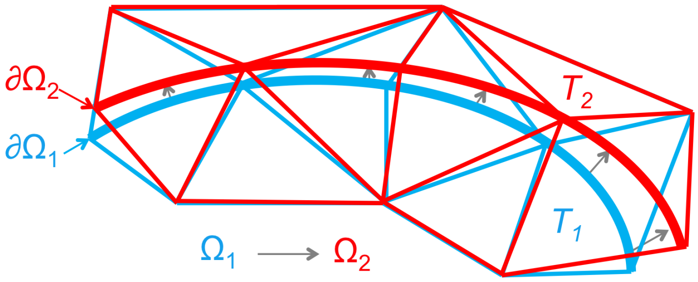

Figure 3.5.: The interface $\partial\Omega_1$ between water and air is deformed into $\partial\Omega_2$. The mesh T_1 is deformed into T_2 to conform to the moving interface.

In order to derive the weak formulation on a moving mesh such as the one shown in Figure 3.5, the Green's first identity is applied to the product $\langle \varphi_j, \mathsf{A}_\alpha \varphi_i\rangle$ with φ_i , $\varphi_j \in H^1(\Omega)$ yielding:

$$\langle \varphi_j, \mathsf{A}_\alpha \varphi_i\rangle = -\iiint_\Omega \varphi_j \vec{\nabla} \cdot \left(\alpha \vec{\nabla} \varphi_i\right) d\Omega \, , \tag{3.18}$$

$$\langle \varphi_j, \mathsf{A}_\alpha \varphi_i\rangle = \iiint_\Omega \vec{\nabla} \varphi_j \cdot \left(\alpha \vec{\nabla} \varphi_i\right) d\Omega - \iint_{\partial\Omega} \varphi_j \left(\alpha \vec{\nabla} \varphi_i\right) \cdot \vec{n} dS \, , \tag{3.19}$$

where the closed surface $\partial\Omega$ is oriented by the outward-pointing normal $\vec{n}$.
Thus, multiplying (3.15) by a test function $\varphi_j \in H^1\left(\Omega|_h^{n+1}\right)$ with support on the mesh element $\Omega_e \in \Omega|_h^{n+1}$ yields for the left hand side:

$$\mathsf{Lhs} = \iiint_{\Omega_e} \sum_{i=1}^{m} v_i \vec{\nabla}\varphi_j \cdot \left(\epsilon_+ \vec{\nabla}\varphi_i\right) d\Omega - \iint_{\partial\Omega_e} \sum_{i=1}^{m} v_i \varphi_j \left(\epsilon_+ \vec{\nabla}\varphi_i\right) \cdot \vec{n} dS \,, \tag{3.20}$$

where the m coefficients v_i are (unknown) degrees of freedom at t_{n+1} and with $\epsilon_+ = \epsilon + \frac{\sigma \mathrm{dt}}{2}$.
Similarly, the right hand side becomes :

$$\mathsf{Rhs} = \iiint_{\Omega_e} \vec{\nabla}\varphi_j \cdot \vec{D}\Big|^n d\Omega - \iint_{\partial\Omega_e} \varphi_j \vec{D}\Big|^n \cdot \vec{n} dS \,, \tag{3.21}$$

where the quantity $\vec{D}\Big|^n = \epsilon_- \vec{\nabla} V$ and $\epsilon_- = \epsilon - \frac{\sigma \mathrm{dt}}{2}$ are evaluated in the previous mesh $\Omega|_h^n$.
When the meshes $\Omega|_h^n$ and $\Omega|_h^{n+1}$ are identical the right hand side can be written in matrix form as follows:

$$\mathsf{Rhs} = \iiint_{\Omega_e} \sum_{i=1}^{m} v_i\Big|^n \vec{\nabla}\varphi_j \cdot \left(\epsilon_- \vec{\nabla}\varphi_i\right) d\Omega - \iint_{\partial\Omega_e} \sum_{i=1}^{m} v_i\Big|^n \varphi_j \left(\epsilon_- \vec{\nabla}\varphi_i\right) \cdot \vec{n} dS \,, \tag{3.22}$$

where the closed surface $\partial\Omega_e$ is oriented by the normal $\vec{n}$ pointing outward and $v_i\Big|^n$ are (known) degrees of freedom at t_n. It is important to note that $V|^n$ is piecewise smooth in $\Omega|_h^n$ but only piecewise continuous in $\Omega|_h^{n+1}$ (if both meshes do not coincide).

3.4.3 Approximation spaces on a moving mesh

The scalar potential V_{Ω_1} is approximated by polynomial shape functions. This is efficiently implemented by using hierarchical high order basis functions. Such basis functions for tetrahedral elements of variable and arbitrary order have been presented in [18]. The use of high spatial orders is necessary to accurately derive the scalar potential in order to calculate the Maxwell stress tensor and the electric force density. The advantage of polynomial spaces is that elementary integrals as appearing in (3.22) can be exactly computed by a Gauss quadrature of degree d where d is the order of the integrand.
The weak formulation (3.15) is performed in $\Omega_2 = \Omega|_h^{n+1}$, however the calculation of the right hand side $\langle \varphi_j, B|_h^n \rangle$ involves quantities approximated in $\Omega_1 = \Omega|_h^n$.
For instance, the scalar potential V_{Ω_1} is approximated by polynomial shape functions which are smooth in every element of Ω_1 but only continuous at material interfaces as shown in Figure 3.6. As the droplet interface is moved in order to conform to the new droplet shape, V_{Ω_1} is no longer piecewise smooth in the deformed mesh Ω_2 as shown in Figure 3.7. The loss of smoothness concerns only the mesh elements touching the droplet interface. In these mesh elements the numerical integration based on a Gauss quadrature of degree d is no longer exact for a polynomial of the same degree since V_{Ω_1} is only piecewise polynomial in these elements.

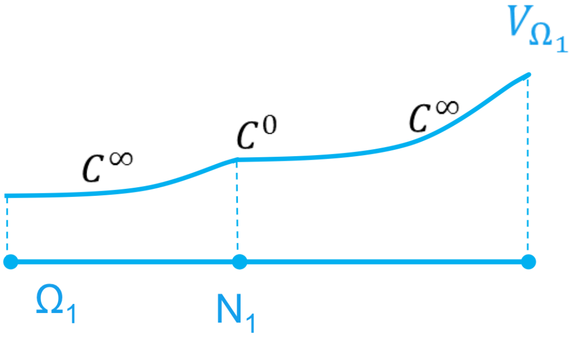

Figure 3.6.: Representation of V_{Ω_1} in Ω_1 as a piecewise smooth function. The approximation is differentiable within each element of Ω_1.

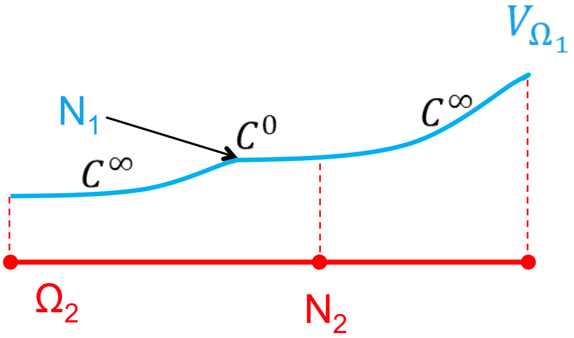

Figure 3.7.: Solution V_{Ω_1} on Ω_2. The kink of the old solution at N_1 can no longer be represented exactly on on Ω_2. The solution is no longer smooth in the elements of Ω_2 touching the droplet interface.

3.4.4 The geometrical discretization

Tetrahedral meshes are well suited to discretize computational domains including objects whose characteristic lengths differ by several orders of magnitudes. This is the case of the droplet between the pair of electrodes shown in Figure 3.2. The use of high geometrical orders (in our case quadratic) greatly reduces the number of tetrahedra needed to accurately discretize curved objects. This is important for problems of elliptic and parabolic type because the error is maximal on the boundaries.

The number of tetrahedra is further reduced by using p-adaptivity which allows to increase the order of the solution approximation in selected elements, typically at material interfaces. The combination of high geometrical and spatial orders enables an accurate derivation of the scalar potential to evaluate the Maxwell Stress Tensor and the electric force density.

The ten node quadratic tetrahedron is shown in Figure 3.8. It is based on the linear tetrahedron augmented by six side nodes placed at the midpoints of each edge. The position of the side nodes can deviate of the midpoints to allow for curved faces and sides.

The shape functions of the quadratic tetrahedron are quadratic and interpolatory:

$$\begin{aligned} N_i &= l_i\left(2l_i-1\right),\; 1\le i\le 4\,, && (3.23)\\ N_5 &= 4l_1l_2,\; N_6=4l_2l_3,\; N_7=4l_3l_1,\; N_8=4l_1l_4,\; N_9=4l_2l_4,\; N_{10}=4l_3l_4\,, && (3.24)\\ l_i &= \zeta_i,\; 1\le i\le 3 \text{ and } l_4=1-\zeta_1-\zeta_2-\zeta_3\,, && (3.25)\end{aligned}$$

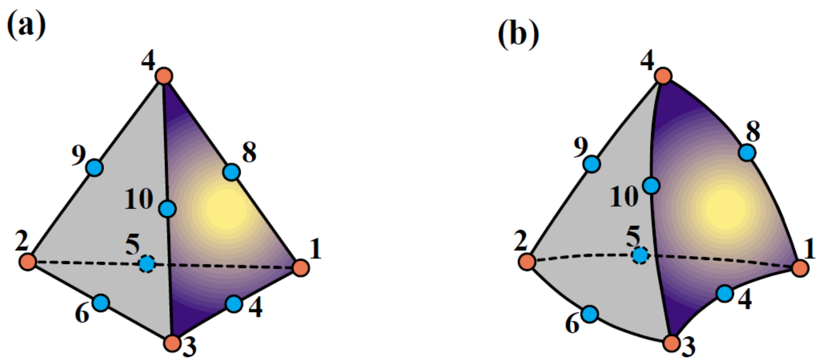

Figure 3.8.: The quadratic tetrahedron with planar (a) or curved faces (b), (image from [19]).

where the ζ_i, $1 \leq i \leq 3$ are the barycentric or local coordinates of the tetrahedron.
A projection method is used to map any point of the reference tetrahedral element whose coordinates are $\zeta = (\zeta_1, \zeta_2, \zeta_3)$ in the Cartesian frame $(O, \vec{e}_1, \vec{e}_2, \vec{e}_2)$ to a point whose coordinates are $x = (x_1, x_2, x_3)$ in an arbitrary tetrahedron T. This is achieved through the following transformation:

$$\begin{aligned} \mathsf{F}_T : [0,1]^3 &\rightarrow T && (3.26) \\ (\zeta_1, \zeta_2, \zeta_3) &\rightarrow (x_1, x_2, x_3) \text{ with } x_i = \sum_{j=1}^{10} x_{ij} N_j (\zeta_1, \zeta_2, \zeta_3), \; 1 \leq i \leq 3, && (3.27) \end{aligned}$$

where the $\left(x_{ij}\right)_{1 \leq j \leq 3}$ are the coordinates of the nodes M_i, $1 \leq i \leq 10$ forming the tetrahedron T.
The Jacobian J of the transformation F_T is:

$$\mathsf{J} = \begin{pmatrix} \frac{\partial x_1}{\partial \zeta_1} & \frac{\partial x_1}{\partial \zeta_2} & \frac{\partial x_1}{\partial \zeta_3} \\ \frac{\partial x_2}{\partial \zeta_1} & \frac{\partial x_2}{\partial \zeta_2} & \frac{\partial x_2}{\partial \zeta_3} \\ \frac{\partial x_3}{\partial \zeta_1} & \frac{\partial x_3}{\partial \zeta_2} & \frac{\partial x_3}{\partial \zeta_3} \end{pmatrix} = \begin{pmatrix} J_{.1} & J_{.2} & J_{.3} \end{pmatrix}, \tag{3.28}$$

where the $J_{.i}$ are the column vectors of J.
The second derivative of the vector-valued transformation F_T is an array of dimension $3 \times 3 \times 3$:

$$\begin{pmatrix} \mathsf{H}_1 & \mathsf{H}_2 & \mathsf{H}_3 \end{pmatrix} = \begin{pmatrix} \frac{\partial}{\partial \zeta_1}(\mathsf{J}) & \frac{\partial}{\partial \zeta_2}(\mathsf{J}) & \frac{\partial}{\partial \zeta_3}(\mathsf{J}) \end{pmatrix}. \tag{3.29}$$

An edge $d\zeta_i \vec{e}_i$ is transformed into $dx_i \vec{e}_i$ with $dx_i = d\zeta_i J_{.i}$. Therefore the volume

$$d\zeta_1 d\zeta_2 d\zeta_3 = d\zeta_1 \vec{e}_1 \cdot \left(d\zeta_2 \vec{e}_2 \times d\zeta_3 \vec{e}_3\right), \tag{3.30}$$

is transformed into:

$$dx_1 \vec{e}_1 \cdot \left(dx_2 \vec{e}_2 \times dx_3 \vec{e}_3\right) = d\zeta_1 d\zeta_2 d\zeta_3 J_{.1} \cdot \left(J_{.2} \times J_{.3}\right). \tag{3.31}$$

The identity between the scalar triple product and the determinant yields:

$$dx_1 dx_2 dx_3 = d\zeta_1 d\zeta_2 d\zeta_3 |\det \mathsf{J}|. \tag{3.32}$$

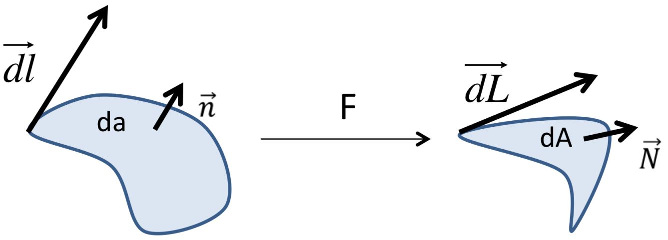

Figure 3.9.: Surface transformation

We now consider the oriented surface $\vec{da} = da\vec{n}$ extruded along $\vec{dl}$ and transform it into $\vec{dA} = dA\vec{N}$ extruded along $\vec{dL} = \mathsf{J}\vec{dl}$ as shown in Figure 3.9. The volume $dv = {}^t\vec{dl}\cdot\vec{da}$ becomes:

$$\begin{aligned} dV = {}^t\vec{dL}\cdot\vec{dA} &= |\mathrm{det}\mathsf{J}|dv\,, && (3.33)\\ {}^t\left(\mathsf{J}\vec{dl}\right)\cdot\vec{dA} &= |\mathrm{det}\mathsf{J}|\,{}^t\vec{dl}\cdot\vec{da}\,, && (3.34)\\ {}^t\vec{dl}\,{}^t\mathsf{J}\cdot\vec{dA} &= {}^t\vec{dl}|\mathrm{det}\mathsf{J}|\cdot\vec{da} \Rightarrow {}^t\mathsf{J}\cdot\vec{dA} = |\mathrm{det}\mathsf{J}|\vec{da}\,, && (3.35)\\ \Rightarrow \vec{dA} &= |\mathrm{det}\mathsf{J}|\,{}^t\mathsf{J}^{-1}\cdot\vec{da}\,. && (3.36)\end{aligned}$$

The gradient of the scalar potential V is written in the reference element as:

$$\vec{\nabla}_\zeta V = \begin{pmatrix} \frac{\partial V}{\partial \zeta_1}\\ \frac{\partial V}{\partial \zeta_2}\\ \frac{\partial V}{\partial \zeta_3}\end{pmatrix} = \begin{pmatrix} \frac{\partial V}{\partial x_1}\frac{\partial x_1}{\partial \zeta_1} + \frac{\partial V}{\partial x_2}\frac{\partial x_2}{\partial \zeta_1} + \frac{\partial V}{\partial x_3}\frac{\partial x_3}{\partial \zeta_1}\\ \frac{\partial V}{\partial x_1}\frac{\partial x_1}{\partial \zeta_2} + \frac{\partial V}{\partial x_2}\frac{\partial x_2}{\partial \zeta_2} + \frac{\partial V}{\partial x_3}\frac{\partial x_3}{\partial \zeta_2}\\ \frac{\partial V}{\partial x_1}\frac{\partial x_1}{\partial \zeta_3} + \frac{\partial V}{\partial x_2}\frac{\partial x_2}{\partial \zeta_3} + \frac{\partial V}{\partial x_3}\frac{\partial x_3}{\partial \zeta_3}\end{pmatrix}, \tag{3.37}$$

$$\vec{\nabla}_\zeta V = {}^t\mathsf{J}\cdot\begin{pmatrix} \frac{\partial V}{\partial x_1}\\ \frac{\partial V}{\partial x_2}\\ \frac{\partial V}{\partial x_3}\end{pmatrix} = {}^t\mathsf{J}\cdot\vec{\nabla}_x V\,, \tag{3.38}$$

where $\vec{\nabla}_x V$ is the gradient of the scalar potential V in the transformed element. When J is invertible:

$$\vec{\nabla}_x V = {}^t\mathsf{J}^{-1}\cdot\vec{\nabla}_\zeta V\,. \tag{3.39}$$

The Hessian of $V(\zeta)$ in the reference element is defined as:

$$\mathsf{H}_\zeta = \mathsf{H}(\zeta_1,\zeta_2,\zeta_3) = \begin{pmatrix} \frac{\partial^2 V}{\partial \zeta_1^2} & \frac{\partial^2 V}{\partial \zeta_1\partial \zeta_2} & \frac{\partial^2 V}{\partial \zeta_1\partial \zeta_3}\\ \frac{\partial^2 V}{\partial \zeta_2\partial \zeta_1} & \frac{\partial^2 V}{\partial \zeta_2^2} & \frac{\partial^2 V}{\partial \zeta_2\partial \zeta_3}\\ \frac{\partial^2 V}{\partial \zeta_3\partial \zeta_1} & \frac{\partial^2 V}{\partial \zeta_3\partial \zeta_2} & \frac{\partial^2 V}{\partial \zeta_3^2}\end{pmatrix}. \tag{3.40}$$

$$\frac{\partial^2 V}{\partial \zeta_i\partial \zeta_j} = \begin{pmatrix} \frac{\partial x_1}{\partial \zeta_i} & \frac{\partial x_2}{\partial \zeta_i} & \frac{\partial x_3}{\partial \zeta_i}\end{pmatrix}\cdot\begin{pmatrix} \frac{\partial^2 V}{\partial x_1^2} & \frac{\partial^2 V}{\partial x_1\partial x_2} & \frac{\partial^2 V}{\partial x_1\partial x_3}\\ \frac{\partial^2 V}{\partial x_2\partial x_1} & \frac{\partial^2 V}{\partial x_2^2} & \frac{\partial^2 V}{\partial x_2\partial x_3}\\ \frac{\partial^2 V}{\partial x_3\partial x_1} & \frac{\partial^2 V}{\partial x_3\partial x_2} & \frac{\partial^2 V}{\partial x_3^2}\end{pmatrix}\cdot\begin{pmatrix} \frac{\partial x_1}{\partial \zeta_j}\\ \frac{\partial x_2}{\partial \zeta_j}\\ \frac{\partial x_3}{\partial \zeta_j}\end{pmatrix} + \tag{3.41}$$

$$\begin{pmatrix} \frac{\partial^2 x_1}{\partial \zeta_i\partial \zeta_j} & \frac{\partial^2 x_2}{\partial \zeta_i\partial \zeta_j} & \frac{\partial^2 x_3}{\partial \zeta_i\partial \zeta_j}\end{pmatrix}\cdot\begin{pmatrix} \frac{\partial V}{\partial x_1}\\ \frac{\partial V}{\partial x_2}\\ \frac{\partial V}{\partial x_3}\end{pmatrix}. \tag{3.42}$$

Denoting H_x the Hessian of $V(x)$ in the transformed element:

$$\mathsf{H}_x = \mathsf{H}(x_1, x_2, x_3) = \begin{pmatrix} \frac{\partial^2 V}{\partial x_1^2} & \frac{\partial^2 V}{\partial x_1 \partial x_2} & \frac{\partial^2 V}{\partial x_1 \partial x_3} \\ \frac{\partial^2 V}{\partial x_2 \partial x_1} & \frac{\partial^2 V}{\partial x_2^2} & \frac{\partial^2 V}{\partial x_2 \partial x_3} \\ \frac{\partial^2 V}{\partial x_3 \partial x_1} & \frac{\partial^2 V}{\partial x_3 \partial x_2} & \frac{\partial^2 V}{\partial x_3^2} \end{pmatrix}, \tag{3.43}$$

we obtain:

$$\frac{\partial^2 V}{\partial \zeta_i \partial \zeta_j} = \begin{pmatrix} \frac{\partial x_1}{\partial \zeta_i} & \frac{\partial x_2}{\partial \zeta_i} & \frac{\partial x_3}{\partial \zeta_i} \end{pmatrix} \cdot \mathsf{H}_x \cdot \begin{pmatrix} \frac{\partial x_1}{\partial \zeta_j} \\ \frac{\partial x_2}{\partial \zeta_j} \\ \frac{\partial x_3}{\partial \zeta_j} \end{pmatrix} + \frac{\partial}{\partial \zeta_i} \begin{pmatrix} \frac{\partial x_1}{\partial \zeta_j} & \frac{\partial x_2}{\partial \zeta_j} & \frac{\partial x_3}{\partial \zeta_j} \end{pmatrix} \cdot \begin{pmatrix} \frac{\partial V}{\partial x_1} \\ \frac{\partial V}{\partial x_2} \\ \frac{\partial V}{\partial x_3} \end{pmatrix}. \tag{3.44}$$

Therefore:

$$\mathsf{H}_\zeta = {}^t\mathsf{J} \cdot \mathsf{H}_x \cdot \mathsf{J} + \left(\frac{\partial}{\partial \zeta_1} ({}^t\mathsf{J}) \cdot \begin{pmatrix} \frac{\partial V}{\partial x_1} \\ \frac{\partial V}{\partial x_2} \\ \frac{\partial V}{\partial x_3} \end{pmatrix} \quad \frac{\partial}{\partial \zeta_2} ({}^t\mathsf{J}) \cdot \begin{pmatrix} \frac{\partial V}{\partial x_1} \\ \frac{\partial V}{\partial x_2} \\ \frac{\partial V}{\partial x_3} \end{pmatrix} \quad \frac{\partial}{\partial \zeta_3} ({}^t\mathsf{J}) \cdot \begin{pmatrix} \frac{\partial V}{\partial x_1} \\ \frac{\partial V}{\partial x_2} \\ \frac{\partial V}{\partial x_3} \end{pmatrix} \right), \tag{3.45}$$

$$\mathsf{H}_\zeta = {}^t\mathsf{J} \cdot \mathsf{H}_x \cdot \mathsf{J} + \left({}^t\mathsf{H}_1 \cdot \vec{\nabla}_x V \quad {}^t\mathsf{H}_2 \cdot \vec{\nabla}_x V \quad {}^t\mathsf{H}_3 \cdot \vec{\nabla}_x V \right), \tag{3.46}$$

where H_1, H_2, H_3 are the second partial derivatives (3.29) of the geometrical transformation. Finally we recover the Hessian of $V(x)$ in the transformed element:

$$\mathsf{H}_x = {}^t\mathsf{J}^{-1} \cdot \mathsf{H}_\zeta \cdot \mathsf{J}^{-1} + {}^t\mathsf{J}^{-1} \cdot \left({}^t\mathsf{H}_1 \cdot {}^t\mathsf{J}^{-1} \cdot \vec{\nabla}_\zeta V \quad {}^t\mathsf{H}_2 \cdot {}^t\mathsf{J}^{-1} \cdot \vec{\nabla}_\zeta V \quad {}^t\mathsf{H}_3 \cdot {}^t\mathsf{J}^{-1} \cdot \vec{\nabla}_\zeta V \right) \cdot {}^t\mathsf{J}^{-1} \tag{3.47}$$

H_x is dependent on the degrees of the freedom through $\vec{\nabla}_\zeta V = \vec{\nabla} V(\zeta_1, \zeta_2, \zeta_3)$.
In the case of the linear tetrahedon (3.47) reduces to:

$$\mathsf{H}_x = {}^t\mathsf{J}^{-1} \cdot \mathsf{H}_\zeta \cdot \mathsf{J}^{-1}. \tag{3.48}$$

A finite element expression of the Kelvin polarization force density (3.50) is thus obtained for any spatial and geometrical order:

$$\vec{f_K} = (\epsilon - \epsilon_0) \begin{pmatrix} \frac{\partial V}{\partial x_1} \frac{\partial^2 V}{\partial x_1^2} + \frac{\partial V}{\partial x_2} \frac{\partial^2 V}{\partial x_2 \partial x_1} + \frac{\partial V}{\partial x_3} \frac{\partial^2 V}{\partial x_3 \partial x_1} \\ \frac{\partial V}{\partial x_1} \frac{\partial^2 V}{\partial x_1 \partial x_2} + \frac{\partial V}{\partial x_2} \frac{\partial^2 V}{\partial x_2^2} + \frac{\partial V}{\partial x_3} \frac{\partial^2 V}{\partial x_3 \partial x_2} \\ \frac{\partial V}{\partial x_1} \frac{\partial^2 V}{\partial x_1 \partial x_3} + \frac{\partial V}{\partial x_2} \frac{\partial^2 V}{\partial x_2 \partial x_3} + \frac{\partial V}{\partial x_3} \frac{\partial^2 V}{\partial x_3^2} \end{pmatrix}, \tag{3.49}$$

$$\vec{f_K} = (\epsilon - \epsilon_0) \begin{pmatrix} \vec{\nabla}_{x1} V \mathsf{H}_{x11} + \vec{\nabla}_{x2} V \mathsf{H}_{x21} + \vec{\nabla}_{x3} V \mathsf{H}_{x31} \\ \vec{\nabla}_{x1} V \mathsf{H}_{x12} + \vec{\nabla}_{x2} V \mathsf{H}_{x22} + \vec{\nabla}_{x3} V \mathsf{H}_{x32} \\ \vec{\nabla}_{x1} V \mathsf{H}_{x13} + \vec{\nabla}_{x2} V \mathsf{H}_{x23} + \vec{\nabla}_{x3} V \mathsf{H}_{x33} \end{pmatrix}. \tag{3.50}$$

The left hand side (3.20) of the weak formulation can be numerically integrated over the reference element for each tetrahedron T of the computational domain as follows:

$$\mathsf{Lhs} = \iiint_{\substack{0\leq\zeta_1,\zeta_2\leq 1\\ 0\leq\zeta_3\leq 1-\zeta_1-\zeta_2}} \sum_{i=1}^{m} v_i \vec{\nabla}\varphi_j \cdot \left(\epsilon_+ \vec{\nabla}\varphi_i\right) |\mathsf{detJ}| d\zeta_1 d\zeta_2 d\zeta_3 - \tag{3.51}$$

$$\sum_{j=1}^{4} \left(\iint_{\substack{0\leq\zeta_{j_1}\leq 1\\ 0\leq\zeta_{j_2}\leq 1-\zeta_{j_1}\\ \zeta_{j_3}=0}} \sum_{i=1}^{m} v_i \varphi_j \left(\epsilon_+ \vec{\nabla}\varphi_i\right) \cdot |\mathsf{detJ}|\, {}^t\mathsf{J}^{-1} \cdot \vec{n} d\zeta_{j_1} d\zeta_{j_2} \right) . \tag{3.52}$$

The indices j_1, j_2, j_3 identify the vertices of the face j of the tetrahedron T oriented by the outward pointing normal $\vec{n}$. detJ is the determinant of the Jacobian of geometrical transformation F_T which transforms the reference element into T.

Similarly and with the same notation, the right hand side (3.21) is numerically integrated as follows:

$$\mathsf{Rhs} = \iiint_{\substack{0\leq\zeta_1,\zeta_2\leq 1\\ 0\leq\zeta_3\leq 1-\zeta_1-\zeta_2}} \vec{\nabla}\varphi_j \cdot \vec{D}\Big|^{n} |\mathsf{detJ}| d\zeta_1 d\zeta_2 d\zeta_3 - \tag{3.53}$$

$$\sum_{j=1}^{4} \left(\iint_{\substack{0\leq\zeta_{j_1}\leq 1\\ 0\leq\zeta_{j_2}\leq 1-\zeta_{j_1}\\ \zeta_{j_3}=0}} \varphi_j \vec{D}\Big|^{n} \cdot |\mathsf{detJ}|\, {}^t\mathsf{J}^{-1} \cdot \vec{n} d\zeta_{j_1} d\zeta_{j_2} \right) . \tag{3.54}$$

The determinant detJ of the quadratic geometrical transformation is a cubic polynomial. The order of the integrand is therefore $2\left(p-1\right)+3 = 2p+1$ where p is the order of the basis functions used for V.

The numerical integration is carried out by using a Gaussian quadrature rule exact for the order of the integrand. As discussed in section 3.4.3, the quantity $\vec{D}\Big|^{n}$ is not piecewise smooth in the elements touching a material interface that has been deformed between two successive time steps. In these elements the numerical integration is not exact.

We denote Q a point of the Gaussian quadrature used for the numerical integration of the right hand side. Its barycentric coordinates Q_ζ in the reference element are transformed by F_T into its physical coordinates Q_x. The algorithm presented in appendix A.2 finds the tetrahedron $T^{'}$ belonging to the previous mesh $\Omega|_h^n$ which contains Q_x. The knowledge of $T^{'}$ permits to recover the material properties at Q_x at the previous time step.

In addition, the algorithm described in appendix A.1 calculates the barycentric coordinates $Q_{\zeta'}$ in $T^{'}$ allowing to reconstruct the quantity $\vec{D}\Big|^{n} = \epsilon_- \vec{\nabla} V$ with $\epsilon_- = \epsilon - \frac{\sigma \mathrm{dt}}{2}$.

The contributions from the left and right hand side of each mesh elements are assembled into a global matrix and vector, respectively. After collecting the terms from the Dirichlet and Neumann boundary conditions, we obtain a linear system:

$$\mathsf{A} \cdot V|^{n+1} = b, \tag{3.55}$$

where A is a sparse matrix and retains the symmetry and positive definiteness of the div-grad operator (3.9).
The linear system (3.55) must be assembled at each time step to reflect the deformation of the mesh elements. This is a strong argument against the use of a direct solver since the matrix would have to be re-factorized at each time step which would be very costly. However, because the mesh connectivity doesn't change, the numbering of the degrees of freedom and the data structure of the linear system can be reused which makes the use of an iterative solver efficient. The linear solver is solved by the preconditioned conjugate gradient method initialized by the result from the previous time step. The implementation of the finite element assembly and the solution of the linear system is based on the computational toolkit PETSc [20].

This section is devoted to the verification of the time stepping scheme presented in the section 3.3. Simulation results of a parallel plate capacitor are compared to the analytical solution. The capacitor consists of two materials stacked in three layers as shown in Figure 3.10.

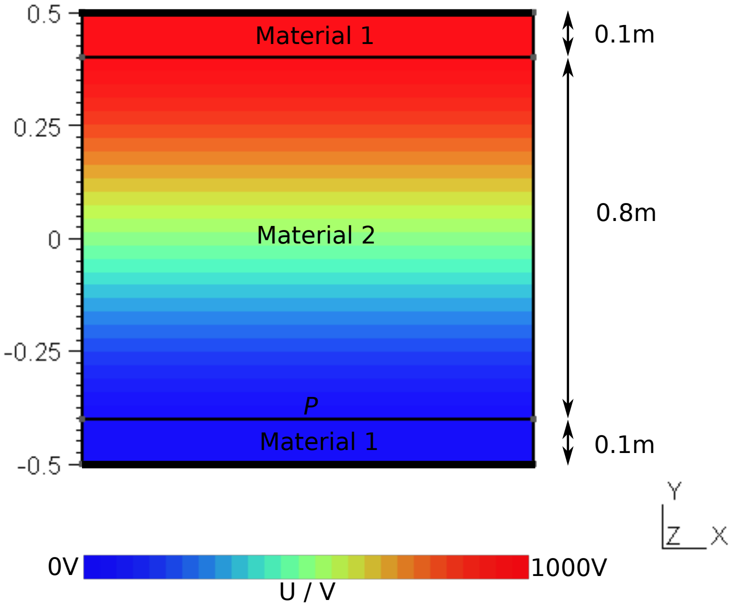

Figure 3.10.: Parallel plate capacitor annotated with the position of the comparison point P.

Material 1 and material 2 have a permittivity of $\varepsilon_1 = \varepsilon_0$ and $\varepsilon_2 = 100\varepsilon_0$, respectively, and a conductivity of $\sigma_1 = 5.7e^{-9}$ S/m and $\sigma_2 = 5.7e^{-10}$ S/m, respectively. The bottom plate potential is set to $0V$ whereas the top plate is excited by a ramp function shown in Figure 3.11 and enforced by using Dirichlet boundary conditions. Homogeneous Neumann boundary conditions are set on the lateral sides.

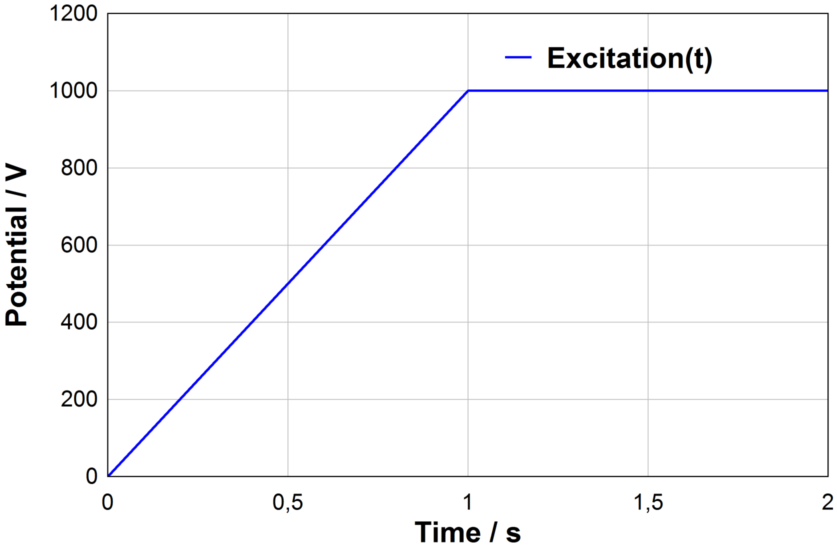

Figure 3.11.: Ramp function exciting the capacitor top plate.

In order to calculate the analytical solution of the electro-quasistatic equation (2.2) at point P, each layer of the parallel plate capacitor is modeled in the frequency domain as a capacitor in parallel to a resistor. The three layers are connected in series forming a voltage divider whose transfer function applied to the ramp function (3.11) is transformed into the time domain by using a Laplace transform yielding the potential $U(t)$ at point P:

$$\begin{aligned} 0 \leq t \leq 1,\; U(t) &= U_{max} \frac{C_2\left(G_1\left(1-e^{-t\frac{G}{C}}\right)\right)+G_2\left(C_1\left(e^{-t\frac{G}{C}}-1\right)+Gt\right)}{G^2}\,, \\ 1 < t \leq 2,\; U(t) &\leftarrow U(t)-U(t-1)\,, \\ 2 < t,\; U(t) &\leftarrow U(2)\,, \end{aligned}$$

with $C = C_1 + 2C_2$, $G = G_1 + 2G_2$, $C_1 = \frac{\varepsilon_1}{d_1}$, $C_2 = \frac{\varepsilon_2}{d_2}$, $G_1 = \frac{\sigma_1}{d_1}$, $G_2 = \frac{\sigma_2}{d_2}$, $d_1 = 0.1m$, $d_2 = 0.8m$, $U_{max} = 1000V$.
The exact potential $U(t)$ is shown in Figure 3.12: The comparison point $P(0.5, 0.1, 0.5)$ is

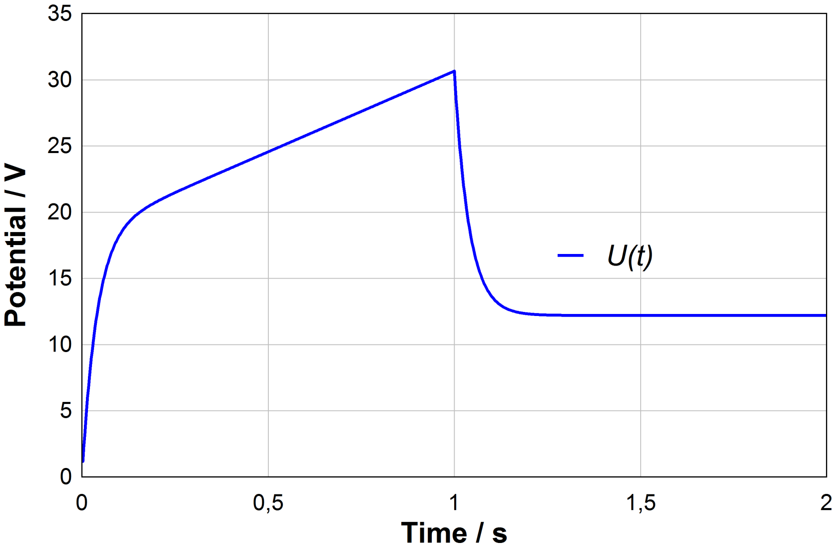

Figure 3.12.: Analytical solution for the electric potential at point P.

positioned at the interface between the two dielectric media where the error on the potential is the largest. The error between the analytical solution and the simulation result is measured for increasingly smaller time steps dt using the discrete relative L∞ error norm defined as:

$$\text{L}\infty\text{-relative} = \max_{0 \leq t \leq 2} \frac{|U(t) - U_{dt}(t)|}{|U(t)|}\,. \tag{3.56}$$

The results of temporal convergence study are presented in Figure 3.13 and confirm that the time stepping scheme (3.3) is of order 2.

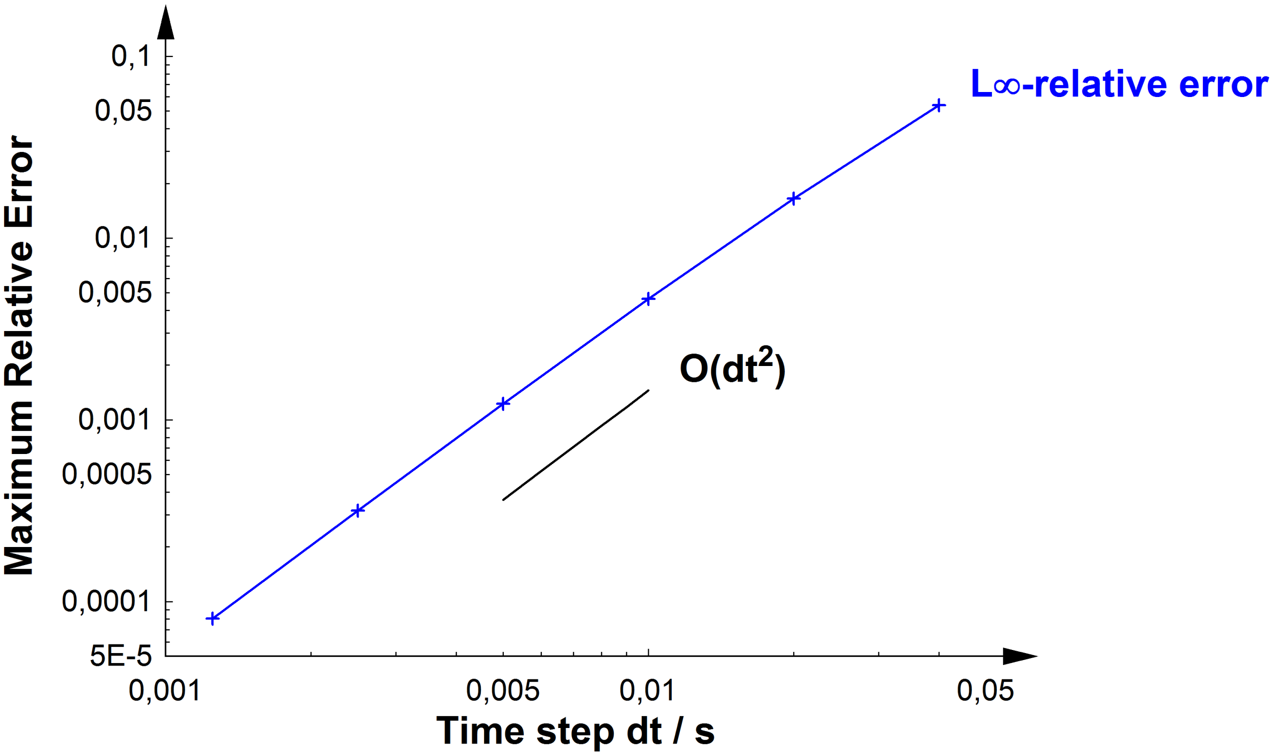

Figure 3.13.: Temporal convergence study at point P showing a second order convergence rate.

3.6 Error of the spatial discretization: polynomial and spectral convergence

This section is devoted to the verification of the finite element discretization presented in section 3.4.4. Simulation results of a spherical capacitor are compared to the analytical solution. The capacitor consists of two concentric layers made of two different materials as shown in Figure 3.14. The radius of the inner boundary is $r_i = 1m$, the radius of the outer boundary is $r_o = 4m$

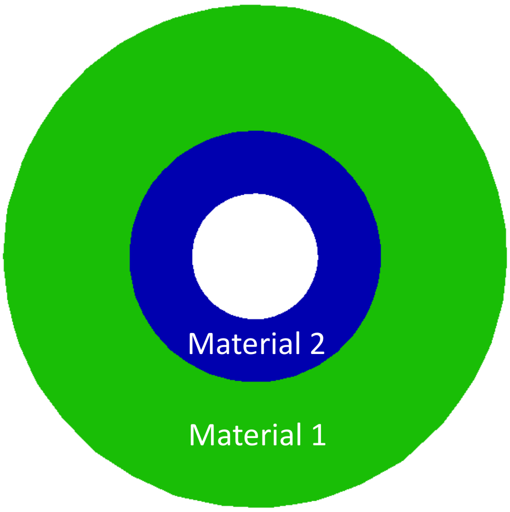

Figure 3.14.: Cross-sectional view of spherical capacitor.

and the radius of the interface between the two materials is $r_f = 2m$. Material 1 and material 2 have a permittivity of $\varepsilon_1 = 2\varepsilon_0$ and $\varepsilon_2 = 80\varepsilon_0$, respectively. Both materials are assumed to be lossless so that potentials calculated at successive time steps are independent from each other, thus removing the influence of the time integration scheme on the accuracy of the solution. The potentials $V_i = 1000V$ on the inner and $V_o = 2500V$ on the outer boundary (peak values) are excited at 50Hz and are enforced by using Dirichlet boundary conditions. The quadratic finite element mesh is shown in Figure 3.15.

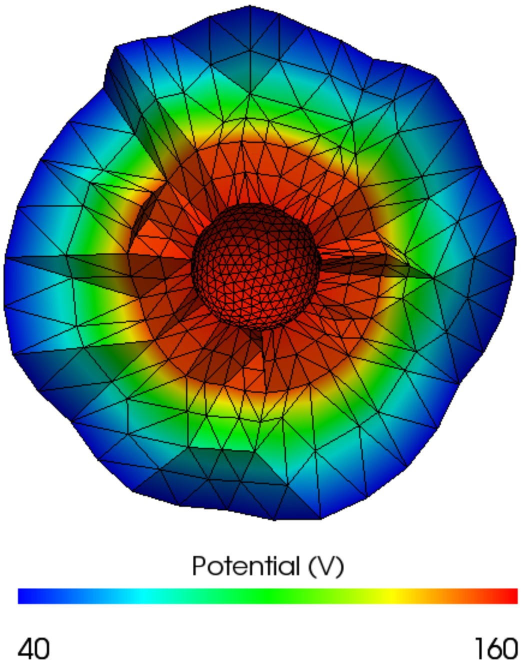

Figure 3.15.: Potential overlaid on a cross section of the quadratic tetrahedral mesh.

In order to calculate the analytical solution of this problem, the electro-quasistatic equation (2.2) is solved in the frequency domain in the spherical coordinates system $(\Omega, r, \vartheta, \varphi)$ of origin $\Omega = (\Omega_1, \Omega_2, \Omega_3)$. The expressions of the potential U, of the electric field $\vec{E} = (E_1, E_2, E_3)$ and of the electric force density $\vec{F} = (F_1, F_2, F_3)$ calculated at the point (x_1, x_2, x_3) in the Cartesian coordinate system of computational domain are:

$$U = \frac{A}{r} + B\,, \tag{3.57}$$

$$E_j = A\left(x_j - \Omega_j\right) r^{-3},\ 1 \leq j \leq 3\,, \tag{3.58}$$

$$F_j = -2\left(\varepsilon - \varepsilon_0\right) A^2 \left(x_j - \Omega_j\right) r^{-6},\ 1 \leq j \leq 3\,, \tag{3.59}$$

where A and B are constant in each material. We denote $s = \frac{\sigma_1 + j\omega\varepsilon_1}{\sigma_2 + j\omega\varepsilon_2}$ where ω is the angular frequency of the excitation. In the material 1:

$$A_1 = \frac{V_i - V_o}{s\left(\frac{1}{r_i} - \frac{1}{r_f}\right) + \frac{1}{r_f} - \frac{1}{r_o}}\,, \tag{3.60}$$

$$B_1 = V_o - \frac{A_1}{r_o}\,, \tag{3.61}$$

and in material 2:

$$A_2 = sA_1\,, \tag{3.62}$$

$$B_2 = A_1\frac{1-s}{r_f} + B_1\,. \tag{3.63}$$

The global errors between the analytical solutions and the simulated results are measured by using the discrete relative L2 error norm defined over the N nodes of the mesh as:

$$\text{L2-relative}(U) = \frac{\sqrt{\sum_{i=1}^{N} |U^{(i)} - U_h^{(i)}|^2}}{\sqrt{\sum_{i=1}^{N} |U^{(i)}|^2}}\,, \tag{3.64}$$

where $U^{(i)}$ and $U_h^{(i)}$ are the analytical and simulated potentials at the node index i, respectively.

$$\text{L2-relative}\left(\vec{E}\right) = \frac{\sqrt{\sum_{\Omega_e\in\Omega_h} ||\vec{E}^{(e)} - \vec{E}_h^{(e)}||^2}}{\sqrt{\sum_{\Omega_e\in\Omega_h} ||\vec{E}^{(e)}||^2}} \text{ and } \text{L2-relative}\left(\vec{F}\right) = \frac{\sqrt{\sum_{\Omega_e\in\Omega_h} ||\vec{F}^{(e)} - \vec{F}_h^{(e)}||^2}}{\sqrt{\sum_{\Omega_e\in\Omega_h} ||\vec{F}^{(e)}||^2}}\,, \tag{3.65}$$

where $\vec{E}^{(e)}, \vec{E}_h^{(e)}, \vec{F}^{(e)}, \vec{F}_h^{(e)}$ are evaluated at the barycentric coordinates $\left(\frac{1}{4}, \frac{1}{4}, \frac{1}{4}\right)$ of the element Ω_e.

Denoting p the order of the basis functions and h the maximum element length, we derive from the asymptotic error estimate (3.17).

$$||U - U_h||_{L^2(\Omega)} = O\left(h^{p+1}\right) \quad \text{when} \quad h \to 0\,, \tag{3.66}$$

and the following asymptotic error estimates for small mesh size:

$$\frac{||U - U_h||_{L^2(\Omega)}}{||U||_{L^2(\Omega)}} \sim \text{L2-relative}(U) = O\left(h^{p+1}\right) \tag{3.67}$$

$$\frac{||\vec{E} - \vec{E}_h||_{L^2(\Omega)}}{||\vec{E}||_{L^2(\Omega)}} \sim \text{L2-relative}\left(\vec{E}\right) = O\left(h^{p}\right) \tag{3.68}$$

$$\frac{||\vec{F} - \vec{F}_h||_{L^2(\Omega)}}{||\vec{F}||_{L^2(\Omega)}} \sim \text{L2-relative}\left(\vec{F}\right) = O\left(h^{p-1}\right) \tag{3.69}$$

The results of a spatial convergence study carried out at order $p = 2$ with the global error norms previously defined are presented in Figure 3.16. These results are obtained for increasingly fine and uniform quadratic tetrahedral meshes parametrized by the element length h.

The Maxwell stress tensor coefficients correspond to the product of the electric field components. It has therefore the same order of convergence as the electric field and is not included in the convergence study.

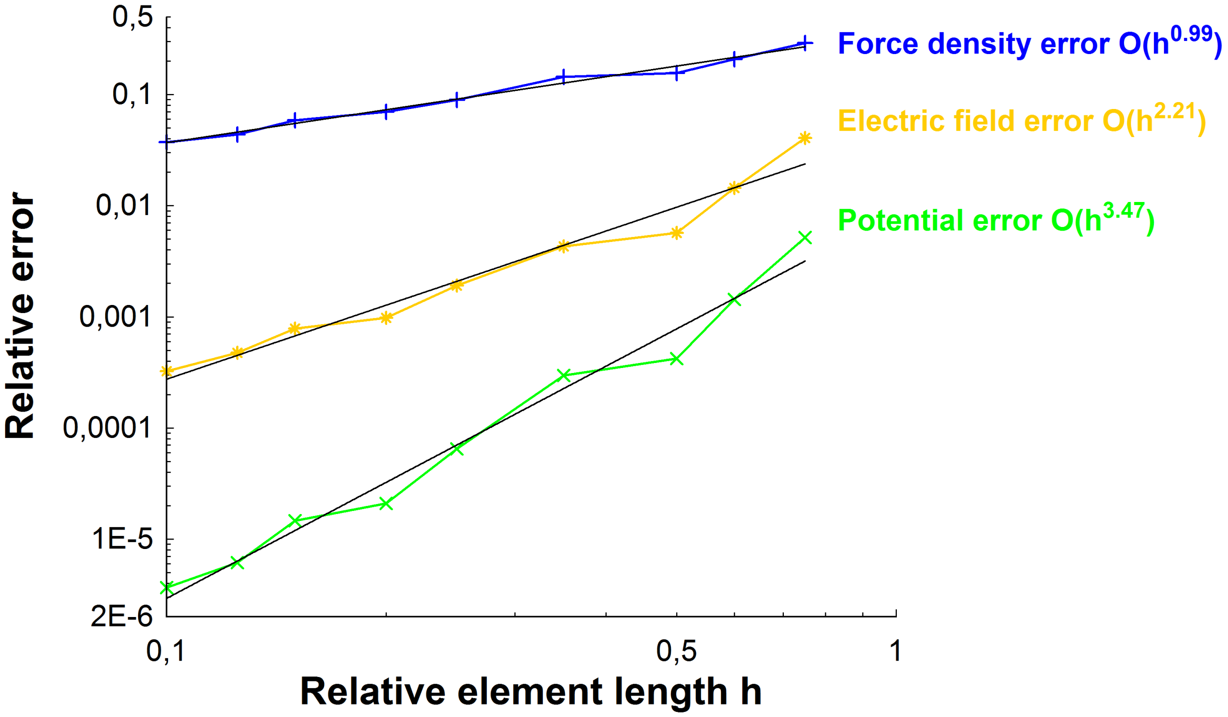

Figure 3.16.: Spatial convergence of the potential, electric field and force density for order $p = 2$.

A log-log scaling is used to display the relative errors as a function of the element length h. In this scaling, the errors are fitted linearly to estimate the orders of convergence of the potential, electric field and electric force density. The converge orders are $p = 3.47$ for the potential, $p = 2.21$ for the electric field and $p = 0.99$ for the electric force which are consistent with the theoretical asymptotic values of $p = 3$, $p = 2$ and $p = 1$, respectively. It is important to notice the slow convergence and much larger error of the electric force density compared to the electric field and potential. On the finest mesh which includes more than 820000 tetrahedras, the potential relative error is $3.6.10^{-6}$, the electric field relative error is $3.25.10^{-4}$ which is two orders of magnitude larger and the electric force density relative error is 0.037 which is again two orders of magnitude larger. These results indicate that it is more efficient to use high order basis functions for the potential (i.e. cubic) than to use a very fine mesh when calculating the electric force density and the electric field. This finding is consistent with the error estimate which shows that the solution converges exponentially with respect to the approximation order. For comparison, a spectral convergence study is carried out on a very coarse curvilinear (quadratic) tetrahedral mesh including 1588 elements. Contrarily to the previous meshes used for the spatial convergence studies which were as uniform as possible, this mesh is fine at the interfaces and coarse everywhere else which reduces significantly the number of elements.
The results of the spectral convergence study for the electric field and force density are presented in Figure 3.17. A linear fit shows a correlation larger than 0.99 for both curves as predicted by the error estimate.

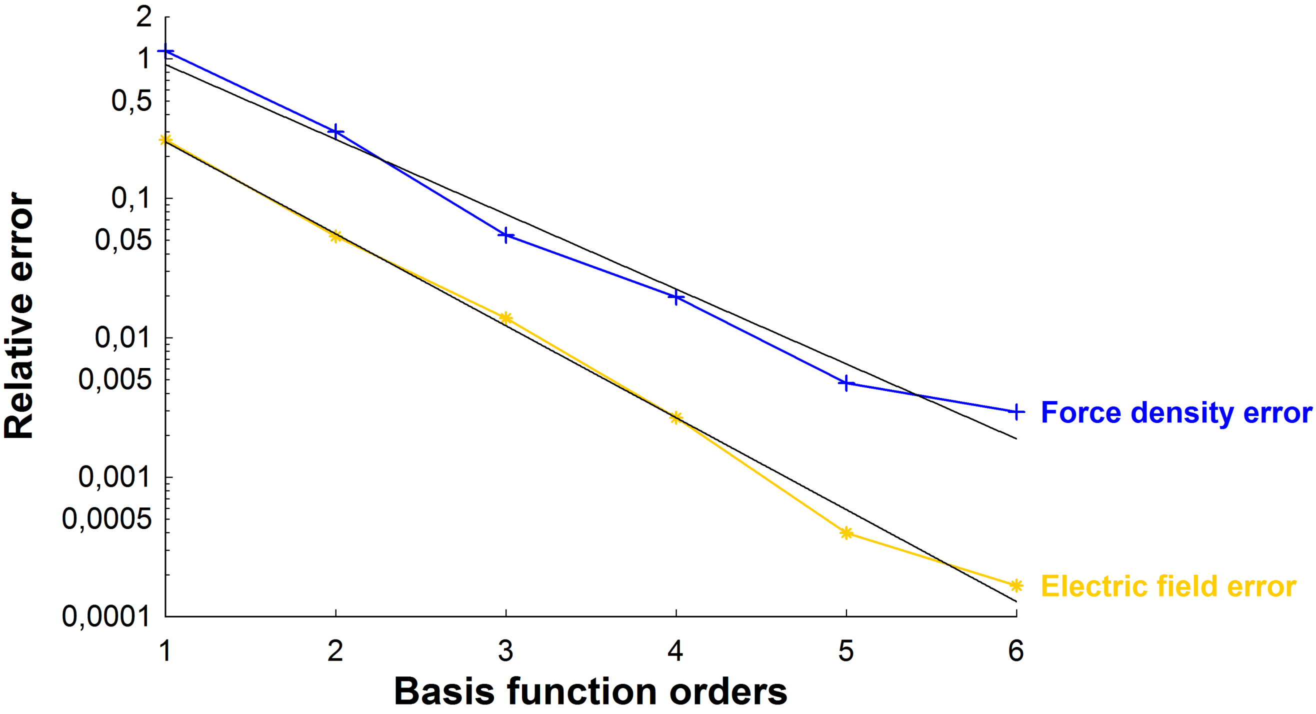

Figure 3.17.: Spectral convergence of the electric field and of the electric force density

4 The fluid dynamic solver

This chapter is devoted to the solver employed to solve the fluid dynamic problem. It is based on the multiphase flow solver interFoam included in the simulation framework OpenFoam 1.7.0 [2] and documented in [21]. In this work, interFoam has been modified to include the divergence of the Maxwell stress tensor as a source term in the momentum equation. The customized interFoam solver is applied to the fluid dynamic model presented in 2.2 to simulate in a time accurate manner the deformation of the water droplet in the presence of time-varying electric fields.

4.1 Interface capturing for multiphase flows

The interface between water and air is a free surface and is tracked by using the Volume of Fluid method [22]. Each phase of the flow is described by the fraction γ of the control volume it occupies. γ is defined as the integral of the fluid's characteristic function in the control volume. The time evolution of the phase fraction is given by the following transport equation which guarantees the volume conservation in the simulation:

$$\frac{\partial \gamma}{\partial t} + \vec{\nabla} \cdot (\gamma \vec{u}) = 0 \quad \text{with } \gamma = \begin{cases} 0 & \text{in air,} \\ 0 < \gamma < 1 & \text{at the interface,} \\ 1 & \text{in water.} \end{cases} \tag{4.1}$$

The water fraction γ is used to evaluate in the momentum equation the density ϱ and the kinematic viscosity μ in a control volume:

$$\varrho = (1-\gamma)\, \varrho_{air} + \gamma \varrho_{water}\,, \tag{4.2}$$

$$\mu = (1-\gamma)\, \mu_{air} + \gamma \mu_{water}\,. \tag{4.3}$$

The contrast between the air and water densities, respectively, $\varrho_{air} = 1.2 kg/m^3$ and $\varrho_{water} = 998 kg/m^3$ at $20°C$ is very large. Small errors in the fraction could lead to large errors in the calculation of the material properties which require special care to ensure proper conservation of the phase fraction. This issue is critical, implementation dependent and will be further addressed in section 4.1.1 devoted to the Volume Of Fluid method. The equation (4.1) is solved by using the geometrical reconstruction approach presented in [22] in order to avoid the difficulties arising from the discontinuous nature of γ.

4.1.1 The Volume of Fluid method

In a control volume, the water fraction γ is defined as follows:

$$\gamma = \frac{1}{v} \iiint_{\Omega_v} \begin{cases} 0 & \text{in air,} \\ 1 & \text{in water,} \end{cases} d\Omega \tag{4.4}$$

where v is the volume of Ω_v.
The two fluids water and air are not miscible and are modeled as a single fluid whose physical properties are calculated as the average of air and water weighted by the water fraction of the volume they occupy in a cell as shown:

$$\begin{aligned} \varrho &= \gamma\left(\varrho_{water} - \varrho_{air}\right) + \varrho_{air} \,, && (4.5)\\ \mu &= \gamma\left(\mu_{water} - \mu_{air}\right) + \mu_{air} \,. && (4.6)\end{aligned}$$

The conservation of mass yields:

$$\begin{aligned} \frac{\partial \varrho}{\partial t} + \vec{\nabla}\cdot\left(\varrho\vec{u}\right) &= 0, && (4.7)\\ \left(\varrho_{water} - \varrho_{air}\right)\frac{\partial \gamma}{\partial t} + \left(\varrho_{water} - \varrho_{air}\right)\vec{\nabla}\cdot\left(\gamma\vec{u}\right) + \varrho_{air}\vec{\nabla}\cdot\vec{u} &= 0. && (4.8)\end{aligned}$$

Since the flow is incompressible $\vec{\nabla}\cdot\vec{u} = 0$, one obtains the following transport equation:

$$\frac{\partial \gamma}{\partial t} + \vec{\nabla}\cdot\left(\gamma\vec{u}\right) = 0\,. \qquad (4.9)$$

The equation (4.9) is solved simultaneously with the momentum equation. The discretization of (4.9) yields a numerical scheme which is usually too diffusive to preserve the sharpness of the interface. Thus, the following compression term $\vec{\nabla}\cdot\gamma\left(1-\gamma\right)\vec{u}_c$ is added which leads to a modified transport equation:

$$\frac{\partial \gamma}{\partial t} + \vec{\nabla}\cdot\left(\gamma\vec{u}\right) + \vec{\nabla}\cdot\gamma\left(1-\gamma\right)\vec{u}_c = 0\,, \qquad (4.10)$$

where $\vec{u}_c$ is an artificial velocity whose direction is normal and oriented toward the interface and whose magnitude is controlled by a user-defined parameter. It is important to note that the compression term is only active in partially filled cells where $\gamma\left(1-\gamma\right) \neq 0$. The boundedness of γ is ensured independently of the underlying numerical scheme by the Multidimensional Universal Limiter for Explicit Solutions (MULES) described in [21].

4.1.2 Surface Tensions

The Volume of Fluid method is used in conjunction with the Continuum Surface Force model [23] to model the surface tension and to estimate the mean surface curvature K. In this model the interface between two immiscible fluids is not modelled as a sharp discontinuity. Rather one assumes a continuous transition from one fluid to another and the interface is considered to have a thickness corresponding to one or two cells. Consequently, the surface tension force $\vec{f}_s$ and the mean curvature K are evaluated as:

$$\begin{aligned} K &= -\vec{\nabla}\cdot\left(\frac{\vec{\nabla}\gamma}{\|\vec{\nabla}\gamma\|}\right), && (4.11)\\ \vec{f}_s &= \sigma_s K\vec{\nabla}\gamma. && (4.12)\end{aligned}$$

The thickness of the transition is $O\left(h\right)$ where h is the characteristic cell size at the interface. As the mesh gets finer, the transition region gets thinner and the fluid interface gets sharper.

4.1.3 The contact line model

At the interface where water is in contact with the polymer a no-slip boundary condition is enforced as shown in figure 4.1.

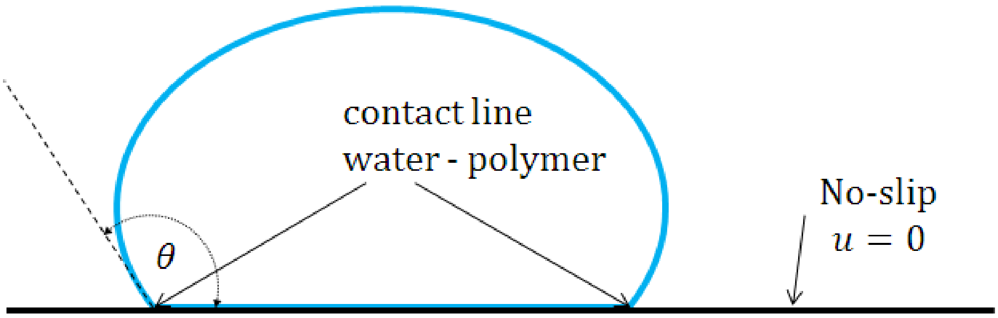

Figure 4.1.: Contact line model.

OpenFoam offers several empirical models to describe the behavior of the surface tension at walls. The model does not attempt to properly describe the displacement of the contact line as no surface-force balance is applied, but offer ways to constraint the contact angle. In this work, a dynamic contact model is used which ensures that the contact angle stays within a user-defined range $\vartheta_{min} \leq \vartheta \leq \vartheta_{max}$ determined experimentally by the hydrophobicity of the polymer. At the surface of the polymer we limit the calculated γ to ensure that it stays bounded.

4.2 Solution of the momentum equation

The droplet deformation is governed by the following incompressible Navier-Stokes equations:

$$\begin{aligned} \frac{\partial \varrho \vec{u}}{\partial t} + \vec{\nabla} \cdot \left(\varrho \vec{u} \otimes \vec{u} \right) - \mathrm{div}\left(\mathsf{T}_{\mathrm{v}} \right) &= -\vec{\nabla} p + \varrho \vec{g} + \vec{f}_s + \mathrm{div}\left(\mathsf{T} \right), && (4.13) \\ \mathsf{T}_{\mathrm{v}} &= \mu \left(\vec{\nabla} \vec{u} + {}^t \vec{\nabla} \vec{u} \right) , && (4.14) \\ \vec{\nabla} \cdot \vec{u} &= 0 , && (4.15) \end{aligned}$$

where $\vec{u}$ is the fluid velocity, p is the pressure, ϱ is the mass density, μ is the dynamic viscosity, T_{v} is the deviatoric viscous stress tensor, $\vec{g}$ is the gravitational force density, $\vec{f}_s$ is the water droplet surface tension force. The electrical problem and the fluid dynamics problem are coupled through the divergence of the Maxwell stress tensor T whose expression is given in 2.1.4.
In interFoam, the pressure $p\left(x\right)$ is replaced by the sum of the hydrostatic pressure (due to the force of gravity) and of dynamic pressure as follows:

$$\begin{aligned} p' &= p - \varrho \vec{g} \cdot \vec{x} , && (4.16) \\ \vec{\nabla} p' &= \vec{\nabla} p - \varrho \vec{g} - \vec{\nabla} \varrho \left(\vec{g} \cdot \vec{x} \right) . && (4.17) \end{aligned}$$

This approach assumes a derivable density gradient which is consistent with the Continuum Surface Force model and the Volume of Fluid method described in the previous sections. Thus, the density gradient is large and piece-wise continuous at the transition between air and water and is zero elsewhere.

The viscous term is transformed by using the vector identity:

$$\begin{aligned}
\mathsf{div}\left(\mathsf{T_v}\right) &= \vec{\nabla}\cdot\mu\vec{\nabla}\vec{u}+\vec{\nabla}\cdot\mu^{t}\vec{\nabla}\vec{u}\,, && (4.18)\\
\mathsf{div}\left(\mathsf{T_v}\right) &= \vec{\nabla}\cdot\mu\vec{\nabla}\vec{u}+\vec{\nabla}\mu\cdot\vec{\nabla}\vec{u}+\mu\vec{\nabla}\left(\vec{\nabla}\cdot\vec{u}\right)\,, && (4.19)\\
\mathsf{div}\left(\mathsf{T_v}\right) &= \vec{\nabla}\cdot\mu\vec{\nabla}\vec{u}+\vec{\nabla}\mu\cdot\vec{\nabla}\vec{u}\,. && (4.20)
\end{aligned}$$

Finally the momentum equation becomes:

$$\frac{\partial\varrho\vec{u}}{\partial t}+\vec{\nabla}\cdot\left(\varrho\vec{u}\otimes\vec{u}\right)=\vec{\nabla}\cdot\left(\mu\vec{\nabla}\vec{u}\right)+\vec{\nabla}\mu\cdot\vec{\nabla}\vec{u}-\vec{\nabla}p'-\vec{\nabla}\varrho\left(\vec{g}\cdot\vec{x}\right)+\sigma_{s}K\vec{\nabla}\gamma+\vec{\nabla}\cdot\mathsf{T}\,. \tag{4.21}$$

Integrating (4.21) in the control volume Ω_v yields:

$$\begin{aligned}
\iiint_{\Omega_v}\frac{\partial\varrho\vec{u}}{\partial t}d\Omega+\iint_{\partial\Omega_v}\left(\varrho\vec{u}\otimes\vec{u}\right)d\vec{S}=\iint_{\partial\Omega_v}\left(\mu\vec{\nabla}\vec{u}\right)d\vec{S}+\iiint_{\Omega_v}\left(\vec{\nabla}\mu\cdot\vec{\nabla}\vec{u}\right)d\Omega+\\
\iiint_{\Omega_v}-\vec{\nabla}p'-\vec{\nabla}\varrho\left(\vec{g}\cdot\vec{x}\right)d\Omega+\iiint_{\Omega_v}\left(\sigma_{s}K\vec{\nabla}\gamma\right)d\Omega+\iint_{\partial\Omega_v}\mathsf{T}d\vec{S}\,.
\end{aligned} \tag{4.22}$$

The momentum equation is solved by using the Pressure-Implicit Split-Operator method (PISO) [24] which solves iteratively the momentum equation by using a predictor-corrector strategy. It consists of predicting a velocity field and then correcting it with an implicit pressure correction procedure and the continuity equation. To that end, the momentum equation (4.22) is first rewritten by dropping all the terms that are not dependent of the velocity yielding:

$$\iiint_{\Omega_v}\frac{\partial\varrho\vec{u}}{\partial t}d\Omega+\iint_{\partial\Omega_v}\left(\varrho\vec{u}\otimes\vec{u}\right)d\vec{S}=\iint_{\partial\Omega_v}\left(\mu\vec{\nabla}\vec{u}\right)d\vec{S}+\iiint_{\Omega_v}\left(\vec{\nabla}\mu\cdot\vec{\nabla}\vec{u}\right)d\Omega\,. \tag{4.23}$$

Then, (4.23) is linearized and discretized in time between t_n and t_{n+1}:

$$\begin{aligned}
\frac{\varrho^{n+1}\vec{u}^{*}-\varrho^{n}\vec{u}^{n}}{\Delta t}V+\iint_{\partial\Omega_v}\left(\varrho^{n}\vec{u}^{n}\otimes\vec{u}^{*}\right)d\vec{S}=\iint_{\partial\Omega_v}\left(\mu^{n+1}\vec{\nabla}\vec{u}^{*}\right)d\vec{S}\,,\\
+\iiint_{\Omega_v}\left(\vec{\nabla}\mu^{n+1}\cdot\vec{\nabla}\vec{u}^{n}\right)d\Omega\,,
\end{aligned} \tag{4.24}$$

where $\vec{u}^{*}$ is a predicted velocity field. The known and predicted velocity fields are separated as follows:

$$\frac{\varrho^{n+1}\vec{u}^{*}}{\Delta t}V+\iint_{\partial\Omega_v}\left(\varrho^{n}\vec{u}^{n}\otimes\vec{u}^{*}\right)d\vec{S}-\iint_{\partial\Omega_v}\left(\mu^{n+1}\vec{\nabla}\vec{u}^{*}\right)d\vec{S}=\frac{\varrho^{n}\vec{u}^{n}}{\Delta t}V+\iiint_{\Omega_v}\left(\vec{\nabla}\mu^{n+1}\cdot\vec{\nabla}\vec{u}^{n}\right)d\Omega\,, \tag{4.25}$$

and the contributions of each control volume are assembled into the following linear system:

$$\left[\mathsf{a_{ii}}+\mathsf{a_{ij}}\right]\mathsf{u}^{*}=\mathsf{b}\,, \tag{4.26}$$

where the matrices $[\mathsf{a_{ii}}]$ and $[\mathsf{a_{ij}}]$ contain the diagonal and non diagonal terms of the contribution of the left-hand side of (4.25), respectively. The vector b contains the contribution of the right-hand side of 4.25 accounting for the last known velocity field and dynamic viscosity. The system (4.26) is further rearranged as follows:

$$\begin{aligned} [\mathsf{a_{ii}}]\mathsf{u}^* &= \mathsf{b} - [\mathsf{a_{ij}}]\mathsf{u}^n = \mathsf{H}(\mathsf{u}^n)\,, && (4.27)\\ \mathsf{A}\mathsf{u}^* &= \mathsf{H}(\mathsf{u}^n)\,, && (4.28) \end{aligned}$$

where $\mathsf{A} = [\mathsf{a_{ii}}]$ is a diagonal matrix. The contribution of the pressure, surface tensions, gravity forces and Maxwell stress tensor are added to the linear system (4.28) by using their last known values. This leads to the linear system (4.29) corresponding to a linearized and explicit momentum equation.

$$\mathsf{A}\mathsf{u}^* = \mathsf{H}(\mathsf{u}^n) - \nabla(\mathsf{p}^n) + \mathsf{S}\,, \tag{4.29}$$

where $\nabla(\mathsf{p}) = \sum \iiint_{\Omega_v} \vec{\nabla} p' d\Omega$ accounts for the pressure contribution of each control volume assembled over the computational domain. Similarly,

$$\mathsf{S} = \sum \iiint_{\Omega_v} -\vec{\nabla}\varrho^{n+1}\left(\vec{g}\cdot\vec{x}\right) d\Omega + \sum \iiint_{\Omega_v} \left(\sigma_s K \vec{\nabla}\gamma\right)^{n+1} d\Omega + \sum \iint_{\partial\Omega_v} \mathsf{T}^{n+\frac{1}{2}} d\vec{S}\,, \tag{4.30}$$

accounts for the contributions of the density gradient, surface tensions and Maxwell stress tensor of each control volume assembled over the computational domain.
Since the fluid fraction γ is known at t_{n+1}, the densities can be evaluated at t_{n+1} by using the expression $\varrho = (1-\gamma)\,\varrho_{air} + \gamma\varrho_{water}$.
The solution of equation (4.29) based on the last known pressure and velocity fields corresponds to the first step of the PISO method and yields a predicted velocity field noted u^* which doesn't satisfy the continuity equation.
In a second step, a new predicted velocity field noted u^{**} which satisfies the continuity equation is sought, along a revised pressure field noted p^* yielding the following system:

$$\begin{aligned} \mathsf{A}\mathsf{u}^{**} &= \mathsf{H}(\mathsf{u}^*) - \nabla\left(\mathsf{p}^*\right) + \mathsf{S}\,, && (4.31)\\ \nabla\cdot\mathsf{u}^{**} &= 0\,. && (4.32) \end{aligned}$$

The divergence of equation (4.31) is taken, leading to the Poisson equation (4.33) in which all terms appearing in the right hand side are known:

$$\nabla\cdot\nabla\left(\mathsf{p}^*\right) = \Delta\left(\mathsf{p}^*\right) = \nabla\cdot\mathsf{H}\left(\mathsf{u}^*\right) + \nabla\cdot\mathsf{S}\,. \tag{4.33}$$

The equation (4.33) is the pressure corrector equation and its solution p^* is used into (4.31) to recover u^{**}. The solution of equation (4.31) is cheap since the matrix A is diagonal. The equation (4.31) is known as the momentum corrector equation.
In a third step, a new predicted velocity field noted u^{***} which satisfies the continuity equation is sought along a revised pressure field noted p^{**} yielding the following system:

$$\begin{aligned} \mathsf{A}\mathsf{u}^{***} &= \mathsf{H}(\mathsf{u}^{**}) - \nabla\left(\mathsf{p}^{**}\right) + \mathsf{S}\,, && (4.34)\\ \nabla\cdot\mathsf{u}^{***} &= 0\,. && (4.35) \end{aligned}$$

The divergence of equation (4.34) is taken, leading to the Poisson equation (4.36) in which all terms appearing in the right hand side are known:

$$\nabla \cdot \nabla \left(\mathsf{p}^{**}\right) = \Delta \left(\mathsf{p}^{**}\right) = \nabla \cdot \mathsf{H}\left(\mathsf{u}^{**}\right) + \nabla \cdot \mathsf{S}\,. \tag{4.36}$$

The solution p^{**} of the Poisson equation (4.36) is then used in (4.34) to recover u^{***} .
The first step of this algorithm can be interpreted as a predictor step whereas the second and third steps can be interpreted as a corrector step. The corrector step can be performed repeatedly for a prescribed number of times. In this work three corrector steps were sufficient to reach convergence. The Poisson equations (4.33) and (4.36) are solved by using the preconditioned conjugate gradient method.

4.3 Calculation of the droplet shape in equilibrium

In the absence of electric field, the water droplet on the horizontal surface of the insulator is in equilibrium. This corresponds to the initial condition of the multiphase simulation.
The equilibrium droplet shape depends on the droplet volume, density, surface tension and contact angle. It is governed by the Young-Laplace equation (4.37) and the Young-Dupré equation (4.38) at the contact line:

$$p_{droplet} - p_{air} = \sigma_s \vec{\nabla}_s \cdot \vec{n}\,, \tag{4.37}$$

$$\cos\vartheta_0 = \frac{W_a}{\sigma_s} - 1\,, \tag{4.38}$$

where $\vec{\nabla}_s$ is taken at the interface, ϑ_0 is the contact angle, W_a is the work of adhesion per unit area, $\vec{n}$ is the pointing outward normal to the droplet surface, σ_s is the surface tension, $p_{droplet}$ and p_{air} are the pressure in the droplet and in the air, respectively.
Since the insulator surface is horizontal, the droplet geometry has an azimuthal symmetry around its vertical axis and can be represented in the polar system shown in Figure 4.2.

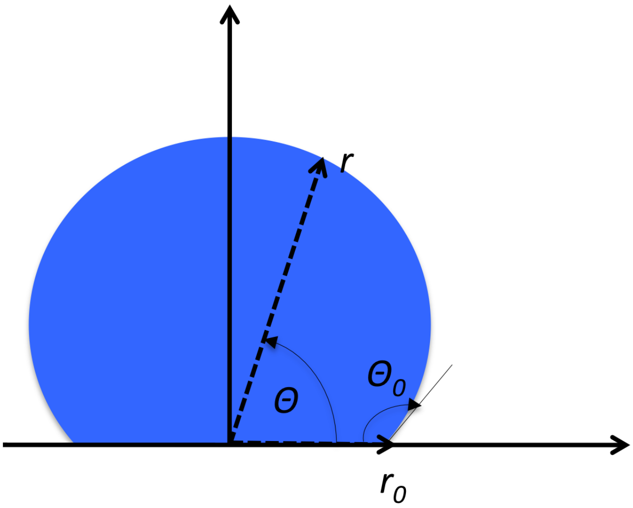

Figure 4.2.: Polar representation of the droplet, its contact radius and its contact angle.

The method described in [25] is applied to calculate the equilibrium profile of the droplet. It simplifies the solution of the Young-Laplace equation (4.37) by transforming the boundary value problem to an initial value problem which can be solved by the Newton-Raphson method or another shooting method. After transformation, the Young-Laplace equation is rewritten in the polar coordinate system as:

$$\frac{\mathrm{d}}{\mathrm{d}\vartheta}\left(\frac{r r' \cos\vartheta}{\sqrt{r^2+r'^2}}\right) - \frac{2r^2+r'^2}{\sqrt{r^2+r'^2}}\cos\vartheta = \left[c_a r \sin\vartheta - 2\left(\frac{\sin\vartheta_0}{r_0} + \frac{c_a v}{2\pi r_0^2}\right)\right] r^2 \cos\vartheta \tag{4.39}$$

with $0 \le \vartheta < 90°$ due to the droplet azimuthal symmetry and where $c_a = \frac{g\varrho}{\sigma_s}$ is the capillary constant, $g = 9.81 m/s^2$ is the gravity, $\sigma_s = 0.0707 N/m$ is the surface tension, $\varrho = 998 kg/m^3$ is the water density, ϑ_0 is the contact angle and v is the droplet volume.
The boundary conditions of the droplet in equilibrium are as follows:

$$r(0) = r_0\,, \tag{4.40}$$

$$\frac{\mathrm{d}r}{\mathrm{d}\vartheta}(0) = -r_0 \frac{\cos\vartheta_0}{\sin\vartheta_0}\,, \tag{4.41}$$

$$\frac{\mathrm{d}r}{\mathrm{d}\vartheta}(90°) = 0\,, \tag{4.42}$$

with r_0 and ϑ_0 the contact radius and contact angle, respectively.
It is important to note that the equation (4.39) is an ordinary differential equation parametrized only by the contact radius r_0 . For a given value r_0, the equation (4.39) is solved for $0 \le \vartheta < 90°$ by an explicit Runge-Kutta method whose initial condition are (4.40) and (4.41). The Newton-Raphson method is then employed to find iteratively the value of r_0 for which the solution of equation (4.39) has the flattest slope at the apex $\vartheta \to 90°$ which correspond to the condition (4.42).
The Newton-Raphson method is initialized with $r_0 = R\sin\vartheta_0$ where R is the radius of the sphere of same volume as the droplet. This procedure is implemented in Mathematica [26] and calculates the droplet equilibrium profile as a (discretized) level set function as shown in Figure 4.3. The level set function is then used to initialize the discretization of the droplet by the procedure described in 5.2.

4.4 The multiphase simulation set-up

Unless specified otherwise, the customized flow solver uses the same default settings as interFoam.
At a temperature of $20°C$, the kinematic viscosity of water and air are $\mu_{water} = 1e^{-6} m^2/s$ and $\mu_{air} = 1.48e^{-5} m^2/s$, respectively, and their density are $\varrho_{water} = 998 kg/m^3$ and $\varrho_{air} = 1.2 kg/m^3$, respectively. The surface tension of water is $\sigma_s = 0.0707 N/m$ and is assumed uniform, constant in time and independent from the electric field.
As seen in section 2.2, the small Weber number indicates that the problem is dominated by surface tension effects rather than by the inertia of the fluid. For this reason, the flow is considered laminar despite its high Reynolds number.

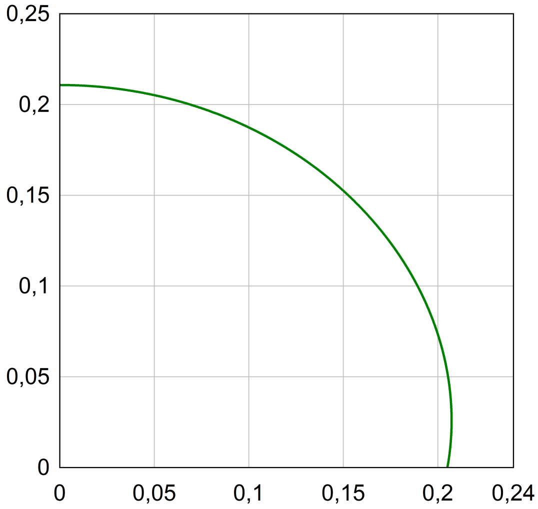

Figure 4.3.: Profile numerically calculated of a $20\mu l$ water droplet in equilibrium lying on a solid support with a contact angle of $100°$.

4.4.1 The boundary conditions

The water droplet is surrounded by air and lies on the polymer insulator. To simulate an open domain, we place the outer boundary of the computational domain at a distance from the droplet which is sufficiently large to neglect the variations of the velocity and pressure in the direction normal to the outer boundary. A distance $d = 0.43925$ mm and $2d$ are used in the horizontal and vertical directions, respectively. The velocity boundary condition for an open boundary is:

$$\begin{aligned} \frac{\partial(\vec{u}\cdot\vec{n})}{\partial n} &= 0\,, && (4.43)\\ \frac{\partial(\vec{u}\cdot\vec{t})}{\partial n} &= 0 \text{ for outflow}\,, && (4.44)\\ \vec{u}\cdot\vec{t} &= 0 \text{ for inflow}\,, && (4.45) \end{aligned}$$

where $\vec{n}$ and $\vec{t}$ are normal and tangent vectors to the surface, respectively.
The pressure boundary condition for an open boundary is:

$$\begin{aligned} p &= p_0 \text{ for outflow}\,, && (4.46)\\ p &= p_0 - \frac{1}{2}\vec{u}\cdot\vec{u} \text{ for inflow}\,, && (4.47) \end{aligned}$$

where p_0 is the total pressure, p is the static pressure and $\frac{1}{2}\vec{u}\cdot\vec{u}$ is the dynamic pressure.
At the surface of the polymer a no-slip boundary condition is assumed yielding:

$$\vec{u} - \vec{u}_{polymer} = 0\,, \tag{4.48}$$

The pressure boundary condition at the polymer surface sets the pressure flux to zero as follows:

$$\iint_{\partial polymer} p d\vec{S} = 0\,. \tag{4.49}$$

The simulation settings used to run the flow solver are described in the appendix A.4.

5 The electrohydrodynamics solver

Water droplets in presence of a strong stationary electrostatic field elongate parallel to the field direction until surface tensions equilibrate the electric force. On the contrary, in presence of a non stationary electrostatic field, an equilibrium can not be reached which causes the droplet to vibrate. This phenomenon is a coupled problem governed by the electro-quasistatic and Navier-Stokes equations.
The methods and solvers used to solve both set of equations were presented in chapters 3 and 4. This chapter is devoted to the time domain solution of the coupled problem.

5.1 Coupling scheme

It has been reported in [3] and [6] that vibration frequencies of an uncharged water droplet in a AC electric field are approximately a multiple of the frequency of the externally applied electric field f_{AC} and that the frequency corresponding to the most visible and largest vibration mode is $2f_{AC}$. Therefore, to sample the droplet deformations with sufficient temporal resolution we choose a coupling time step $\Delta t = \frac{1}{80 f_{AC}}$ which is suitable for vibration frequencies up to $6f_{AC}$.
We denote $\left(t_p\right)_{p\in\mathbb{Z}}$ the sequence of time step $t_p = p\Delta t$, $p \geq -\frac{1}{2}$ and $2p \in \mathbb{Z}$. The proposed coupling scheme performs the time integration of the fluid dynamic solvers in the intervals $\left[t_{n-\frac{1}{2}}\, ,\, t_{n+\frac{1}{2}}\right]_{n\in\mathbb{N}}$ and the time integration of the electro-quasistatic solver in the intervals $\left[t_n\, ,\, t_{n+1}\right]_{n\in\mathbb{N}}$.
The shape of the droplet is described by the water fraction γ which is calculated by the fluid dynamic solver. The finite element discretization of the droplet is updated by processing $\gamma\big|_n$ the water fraction taken at $t_n = n\Delta t$ according to the mesh adaptation procedure described in the section 5.2.
The fluid dynamic solver starts at $t_{-\frac{1}{2}}$ with the following initial conditions:

$$\begin{aligned} \vec{u}|_{-\frac{1}{2}} &= 0\,, && (5.1)\\ \gamma\big|_{-\frac{1}{2}} &= \gamma_{equilibrium}\,, && (5.2) \end{aligned}$$

where $\gamma_{equilibrium}$ is the water fraction corresponding to the equilibrium state without electric fields. $\gamma_{equilibrium}$ is calculated analytically by the procedure presented in the section 4.3:
The electro-quasistatic solver starts at t_0 with the following initial conditions

$$\begin{aligned} V|_0 &= 0\,, && (5.3)\\ \Omega|_0 &\hookleftarrow \gamma\big|_0\,, && (5.4) \end{aligned}$$

where $\Omega|_0$ is the finite element mesh at t_0 and $\hookleftarrow$ indicates that $\Omega|_0$ is updated by processing the water fraction at the same instant.

We denote Ω_v and Ω_e two control volumes of the fluid dynamic and electro-quasistatic computational domain, respectively. The proposed coupling scheme is as follows:

$$\vec{\nabla} \cdot \vec{u} \;=\; 0\,, \tag{5.5}$$

$$\int_{t_{n-\frac{1}{2}}}^{t_{n+\frac{1}{2}}} \left(\iiint_{\Omega_v} \frac{\partial \gamma}{\partial t} + \vec{\nabla} \cdot \left(\gamma \vec{u}\right)\, d\Omega \right) dt \;=\; 0\,, \tag{5.6}$$

$$\int_{t_{n-\frac{1}{2}}}^{t_{n+\frac{1}{2}}} \left(\iiint_{\Omega_v} \frac{\partial \varrho \vec{u}}{\partial t} + \vec{\nabla} \cdot \left(\varrho \vec{u} \vec{u}\right) - \mathrm{div}\left(\mathsf{T}_{\mathsf{v}}\right) + \vec{\nabla} p - \sigma \vec{g} - \vec{f}_s \, d\Omega \right) dt = \left(t_{n+\frac{1}{2}} - t_{n-\frac{1}{2}}\right) \iint_{\partial \Omega_v} \mathsf{T}|_n \cdot d\vec{S}\,, \tag{5.7}$$

where $\vec{u}$ is the fluid velocity, p is the pressure, ϱ is the mass density, μ is the dynamic viscosity, $\mathsf{T}_{\mathsf{v}} = \mu\left(\vec{\nabla}\vec{u} + {}^{t}\vec{\nabla}\vec{u}\right)$ is the stress deviator tensor, $\vec{g}$ is the gravitational force density, $\vec{f}_s$ is the surface tension, γ is the water fraction, $\mathsf{T}|_n$ is the Maxwell stress tensor at t_n assumed to vary linearly in time in the interval $\left[t_{n-\frac{1}{2}}\,,\; t_{n+\frac{1}{2}}\right]$.

The fluid velocity, pressure and water fraction are advanced in time by calling the fluid dynamic solver sequentially over the intervals $\left[t_{n-\frac{1}{2}}\,,\; t_{n+\frac{1}{2}}\right]_{n\in\mathbb{N}}$. This approach makes the temporal coupling scheme independent from the time stepping procedure employed by the fluid dynamic solver.

The electro-quasistatic equation is coupled to the momentum equation by adding the contribution of the flux of the Maxwell Stress Tensor through the faces of the control volume. Since the droplet interface is not modeled sharply (see section 4.1), the Maxwell Stress Tensor is preferred to the electric force densities which are difficult to evaluate accurately as they involved quantities which are discontinuous at interfaces.

The electro-quasistatic solver advances in time the scalar potential as follows:

$$\Omega|_n \;\hookleftarrow\; \gamma\Big|_n\,, \tag{5.8}$$

$$\sum_{j=1}^{r} \int_{t_{n+\frac{j-1}{r}}}^{t_{n+\frac{j}{r}}} \left(\iiint_{\Omega_e} -\vec{\nabla} \cdot \left(\left. \frac{\partial \epsilon \vec{\nabla} V}{\partial t} \right|_{x,y,z} \right) - \vec{\nabla} \cdot \left(\sigma \vec{\nabla}\right)\, d\Omega \right) dt \;=\; 0\,, \tag{5.9}$$

where r is the number of subintervals, V is the scalar potential, ϵ is the permittivity and σ is the conductivity, $\Omega|_n$ is the finite element mesh at t_n and $\hookleftarrow$ indicates that the mesh $\Omega|_n$ is updated by processing the water fraction taken at the same instant.

The integration of the electro-quasistatic solver over the interval $\left[t_n\,,\; t_{n+1}\right]_{n\in\mathbb{N}}$ is carried out by applying the time stepping scheme (3.1) sequentially to each subinterval $\left[t_{n+\frac{j-1}{r}}\,,\; t_{n+\frac{j}{r}}\right]_{n,j\in\mathbb{N},\, j\leq r}$ with the time step $\frac{\Delta t}{r}$.

The first benefit of this approach is the ability to control the time step of the electro-quasistatic solver independently from the coupling time step. Indeed, the simulation of a conductive droplet typically requires for accuracy reasons a significantly smaller time step than the coupling time step.

The second benefit is that the weak formulation is carried on the same mesh for all except the first subinterval $\left[t_n\,,\,t_{n+\frac{1}{r}}\right]_{n\in\mathbb{N}}$. On the first subinterval, the weak formulation is performed on two different meshes by using the equation (3.21) whereas it is performed by using the equation (3.22) on the next subintervals. Not only (3.22) has a lower computational cost but also errors introduced in (3.21) by the inexact numerical integration described in section 3.4.5 and integrated over a time step are proportional to $\frac{\Delta t}{r}$ instead of Δt. Thus this approach lowers the contribution to the global error of the numerical integration error due to the moving mesh.
The electric field and stress tensor are derived from the scalar potential obtained at the instant t_{n+1} as follows:

$$\begin{aligned} \vec{E}\Big|_{n+1} &= -\vec{\nabla}V\Big|_{n+1}\,, \qquad (5.10)\\ \mathsf{T}|_{n+1} &= \left.\begin{pmatrix} D_xE_x-\varepsilon_0\frac{E^2}{2} & D_yE_x & D_zE_x \\ D_xE_y & D_yE_y-\varepsilon_0\frac{E^2}{2} & D_zE_y \\ D_xE_z & D_yE_z & D_zE_z-\varepsilon_0\frac{E^2}{2} \end{pmatrix}\right|_{n+1}. \qquad (5.11) \end{aligned}$$

5.2 Mesh adaptation

The proposed coupling scheme updates the finite element discretization of the water droplet at every time step $t_n = n\Delta t$. The coupling time step $\Delta t = \frac{1}{80 f_{AC}}$ is small enough to sample the droplet deformations with sufficient temporal resolution which ensures that successive changes in the droplet shape are gradual.
Curvilinear tetrahedral meshes can efficiently discretize curved surfaces and can be deformed to match the changing droplet shape which avoids to locally refine the mesh and to change the mesh connectivity. In order to do so, quadratic tetrahedrons whose nodes belong to the droplet surface are deformed to match the new droplet shape. Nodes belonging to the droplet surface (and whose position coincided with the air-water interface at the previous time step) are snapped onto the new air-water interface whereas nodes located inside the droplet or inside the air are moved so that the finite element mesh remains valid and its quality is conserved. The mesh quality improvement procedure is described in the section 5.3.
The node snapping procedure is critical to maintain a consistent representation of the droplet in the finite element mesh used by the electro-quasistatic solver and in the Cartesian grid used by the fluid dynamic solver. Both discretizations are shown in Figure 5.1.
The water droplet and the surrounding air are discretized by the fluid dynamic solver by applying the Volume of Fluid method [22] on a Cartesian grid. This interface capturing method tracks the water-air interface by following the time evolution of the water fraction γ which is defined over the cell Ω_v as follows:

$$\gamma = \frac{1}{v}\iiint_{\Omega_v} \begin{cases} 0 & \text{in air}\,, \\ 1 & \text{in water}\,, \end{cases} d\Omega \qquad (5.12)$$

where v is the volume of Ω_v.
The water fraction is zero in cells of air, one in cells of water and in-between in partially filled cells. The transition between water and air typically occurs over a few cells as shown in Figure

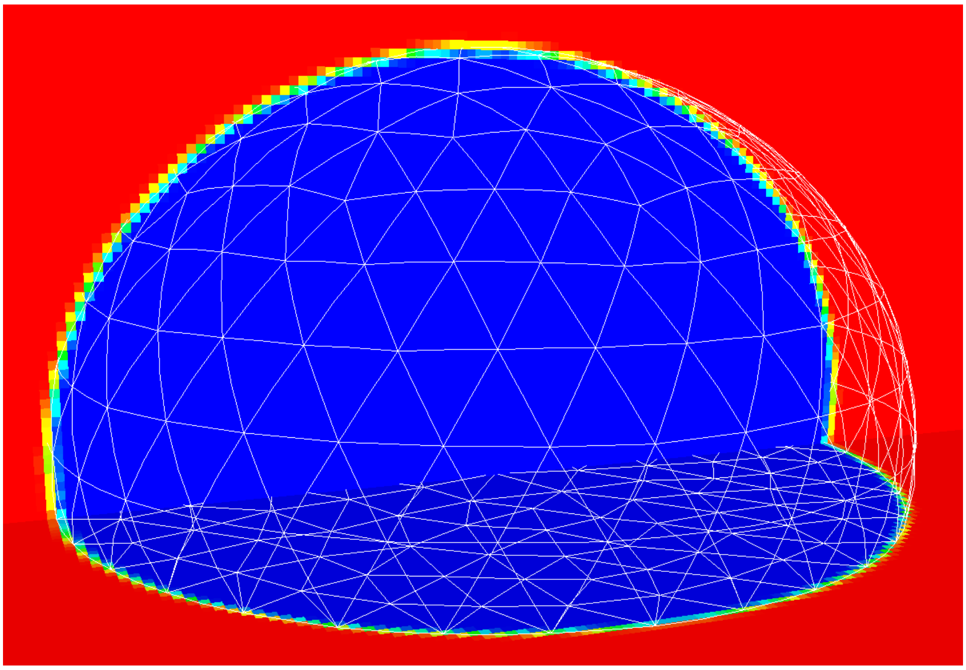

Figure 5.1.: Discretizations of the droplet in the finite element mesh and in the Cartesian grid.

5.1 where the cells of water are colored in blue, the cells of air are in red and the transition cells are in yellow or green.

A key feature of the Volume of Fluid method is its inherent ability to exactly conserve mass and therefore volume in the case of incompressible flow. This is critical in this work since the vibrations of the droplet depends on its volume. We show in Figure 5.2 that the droplet volume calculated during a typical simulation in the finite element mesh and in the VOF grid deviates from the prescribed droplet volume of $20\mu l$ by less than 0.15% and 0.003515%, respectively.

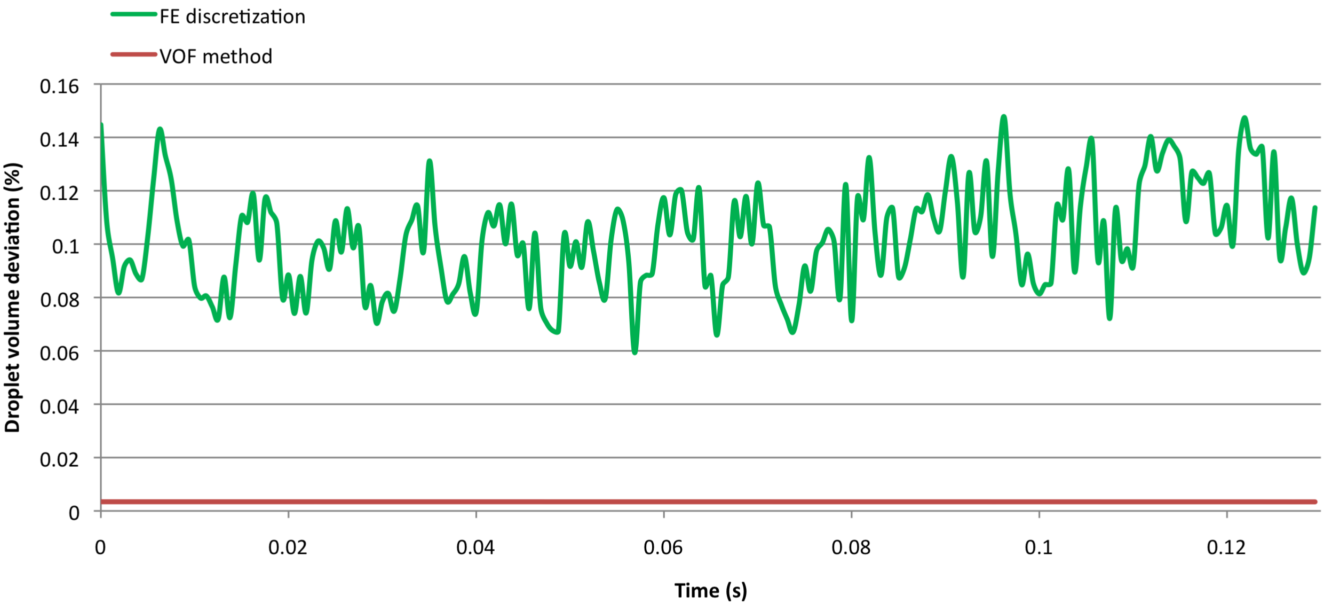

Figure 5.2.: Deviation of the discretized droplet volume with respect to the prescribed droplet volume calculated in the finite element mesh and in the VOF grid.

The initial shape of the water droplet is calculated by solving the Young-Laplace equation by the procedure 4.3 described in the previous chapter. The resulting profile corresponds to the shape of an axisymmetrical water droplet of volume V lying on a solid support with a contact angle ϑ in equilibrium (in the absence of electrical field). The equilibrium profile is used to calculate in each cell of the Cartesian grid the corresponding water fraction $\gamma_{equilibrium}$ analytically.
The continuous nature of the water fraction causes the air-water interface to be spread over two to three cells. Within this transition region we reconstruct the sharp droplet interface numerically. The water fraction of each cell is assigned to its barycenter and is approximated in each direction x independently by two piecewise linear functions connected to the barycenter of its neighboring cells. The location x^* of the sharp interface in the direction x is the solution of $\gamma(x^*) = 0.5$ as shown in Figure 5.3:

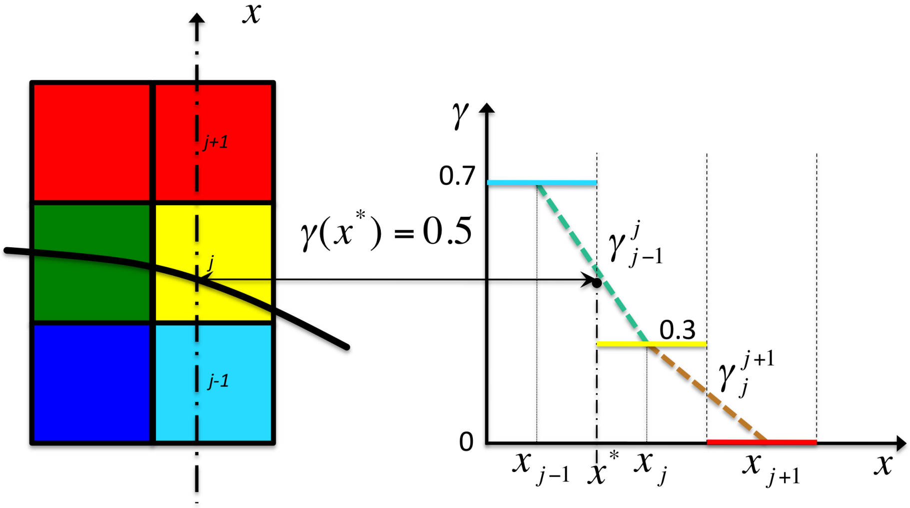

Figure 5.3.: Piecewise linear approximations γ_{j-1}^{j} and γ_{j}^{j+1} of the water fraction within partially filled cells.

The nodes belonging to the droplet surface (also including the midpoints of each edge of the quadratic tetrahedron) are snapped to the droplet shape by performing a linear search in the direction normal to the surface. The solution of the linear search satisfies $\gamma(I^*) = 0.5$ as shown in Figure 5.4.
The normal to the surface calculated at a node is taken as the average of the normals of the linearized triangular face owning this node weighted by the face area. Projecting normally the surface nodes prevent two adjacent nodes from being snapped to the same location while weighting by the face area keeps the surface mesh density as uniform as possible which also improves the surface mesh quality.

5.3 Mesh quality control

Following the mesh adaptation procedure described in the previous section, tetrahedra in contact with the droplet surface have been deformed which may locally degrade the quality of the mesh or render it invalid.
In order to prevent these two outcomes, we propose to apply to the quadratic tetrahedra a mesh improvement procedure which iteratively diffuses the surface mesh deformation into the volume

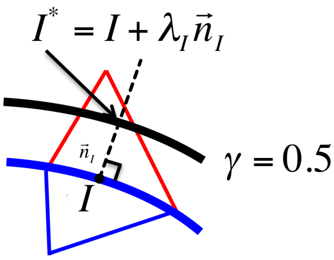

Figure 5.4.: Snapping of I onto the new droplet surface. The new position I^* is obtained by performing a linear search parametrized by λ_I in the direction normal to the surface.

mesh. This is achieved by maximizing the mesh quality with respect to the local cost function (5.13).

Nodes which are on the droplet surface mesh (including the contact line) or belong to a boundary condition (including outer boundaries) are excluded from this procedure. Nodes which are on the polymer insulator surface are only allowed to move tangentially to the polymer surface.

The cost function associated to the node Q is defined over the polyhedron formed by the union of all tetrahedra owning Q. We show in the Figure 5.5 the cost function definition domain in 2D. The cost function is applied to the quadratic tetrahedra after it has been linearized by ignoring its midpoints. The position of the nodes connected to Q is kept constant while the cost function is minimized with respect to the position of Q. The cost function is evaluated as follows:

$$\mathsf{C}(Q) = \frac{1}{N}\sum_{f=1}^{N}\left(\mathsf{AR}\left(Q_{f_1}, Q_{f_2}, Q_{f_3}, Q\right) - 1\right) \tag{5.13}$$

$$\mathsf{AR} = \frac{\sqrt{2}}{12V}\sqrt{\left(\frac{1}{6}\sum_{e=1}^{6} l_e^2\right)^3} \tag{5.14}$$

where N is the number of tetrahedra owning Q, f are the opposing faces of the tetrahedra owing Q, $\mathsf{AR}\left(Q_{f_1}, Q_{f_2}, Q_{f_3}, Q\right)$ is the aspect ratio of the tetrahedron formed by Q and the nodes Q_{f_1}, Q_{f_2}, Q_{f_3} belonging to the opposing face f, V is the volume of the tetrahedron and l_e its edge lengths.

The definition domain of the cost function is the union of all tetrahedra owing Q. It is designed so that it reaches its minimum of zero when all tetrahedra owning Q are equilateral (aspect ratios are 1) which maximizes their quality.

Since the cost function is not linear, we minimize it by applying a nonlinear optimization technique based on the downhill simplex method [27]. This procedure is described in detail in appendix A.3. It finds in the definition domain of the cost function the minimum position Q'. This ensures that moving Q in Q' maximizes the aspect ratio of all tetrahedra owning Q', which smooths the mesh. Before this mesh smoothing procedure is applied, the nodes are sorted so that nodes closest to the most deformed tetrahedra are processed first and that the farthest nodes are processed last. The procedure is applied to the sorted nodes a number of times equal to the largest topological distance between the droplet and the outer boundary. As a result, the deformation is diffused from the droplet surface to the outer boundary which smooths the mesh. Not only this mesh smoothing procedure prevents the mesh to become invalid but its also prevents the conditioning number of the linear system (3.55) from increasing which would hinder

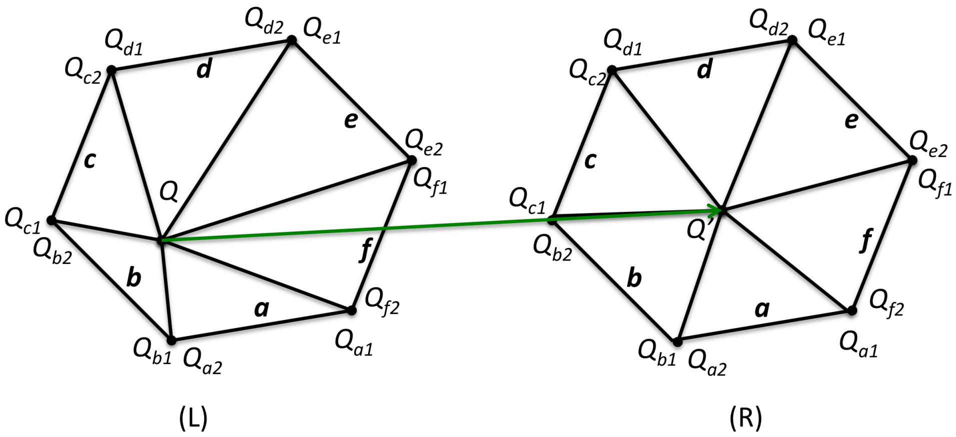

Figure 5.5.: 2D sketch of the 3D definition domain of the cost function associated to the node Q. The domain is a polyhedron formed by all tetrahedra owning Q. The cost function is minimized when Q is moved to Q' .

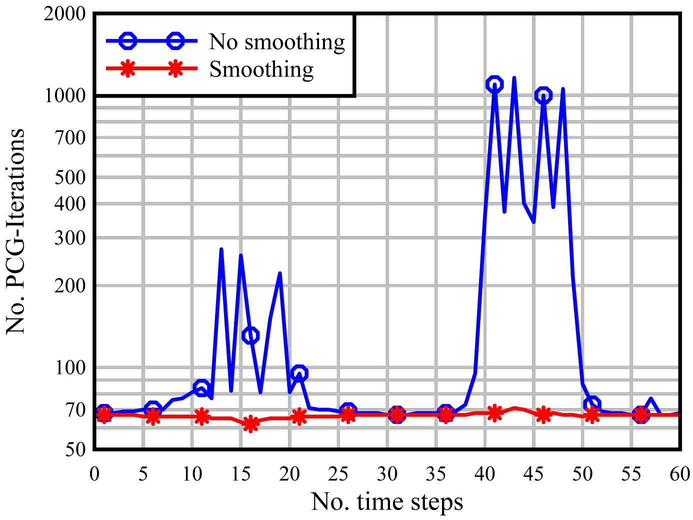

Figure 5.6.: Number of preconditioned conjugate gradient iterations per time steps with and without mesh smoothing.

the convergence of the preconditioned conjugate gradient solver. The benefit of the mesh smoothing procedure is shown in Figure 5.6 for a prescribed downward - upward droplet motion. Without mesh smoothing, the number of PCG iterations increases dramatically when the amplitude of the deformation increases: the first peaks in Figure 5.6 corresponds to a downward motion whereas the second peaks corresponds to an upward motion with a larger amplitude. When the mesh smoothing procedure is enabled, the number of PCG iterations stays the same.

6 Applications

This chapter is devoted to the applications of the electrohydrodynamics (EHD) solver. We apply the EHD solver to simulate the vibrations of rainwater droplets in a strong AC electric field. A sessile rainwater droplet on an insulating surface is exposed to strong AC fields which may be either horizontally or vertically oriented. The shape of the droplet is dynamically deformed under the influence of dielectric forces resulting, typically, in a complicated oscillatory motion which can be simulated by the EHD solver.

In the first part of this chapter, we validate the EHD solver by comparing the oscillatory motion of a simulated droplet to the oscillatory motion of an actual droplet placed on an insulator surface and exposed to strong AC fields. In the second part, we discuss the simulation results and identify the resonance frequencies of the oscillating water droplet.

6.1 Validation

Unless specified otherwise, all experimental data used in this work have been measured by M.Sc. Mohammad H. Nazemi in the framework of his graduate studies at the High Voltage Lab of TU Darmstadt under the supervision of Prof. Dr.-Ing. Volker Hinrichsen.

The experimental set-up consisting of two arrangements is presented in section 3.1 on Figure 3.1 .

In the horizontal field configuration two high voltage electrodes are embedded in an insulating plate at opposite sides [12, 13] and generate a nearly horizontal electric field at the droplet location. Possible electrical discharges will develop only between the two electrodes, since the electric field is concentrated mostly in the region between the electrodes. A water droplet is placed on the insulating plate in the horizontal field region.

To generate a vertical field stress, two circular electrodes are embedded in an insulating material and arranged in a certain distance to each other, thus, providing a small air gap. Embedding the electrodes in the insulator avoids partial discharges occurring at the edges or flashovers between the electrodes. The gap distance can easily be changed to adjust the appropriate E-field at the water droplet. In order to obtain the same electric field stress at both horizontal and vertical arrangements, the applied voltage (RMS value) between the electrodes is $7.5kV$ and $3.35kV$ in the horizontal and the vertical configuration, respectively. The simulated field strength resulting for the two configurations when no water droplet is discussed in section 3.2 and is shown in Figure 3.3. For both configurations, a $20\mu l$ water droplet is used.

The oscillation of the water droplet under the applied electric field stress is captured by a SHIMADZU Hyper Vision (HPV2) high speed camera with 1000 frames per second. After each measurement the insulator surface is cleaned and a new water droplet is placed on the surface. The Figure 6.1 shows the experimental set-up for both arrangements.

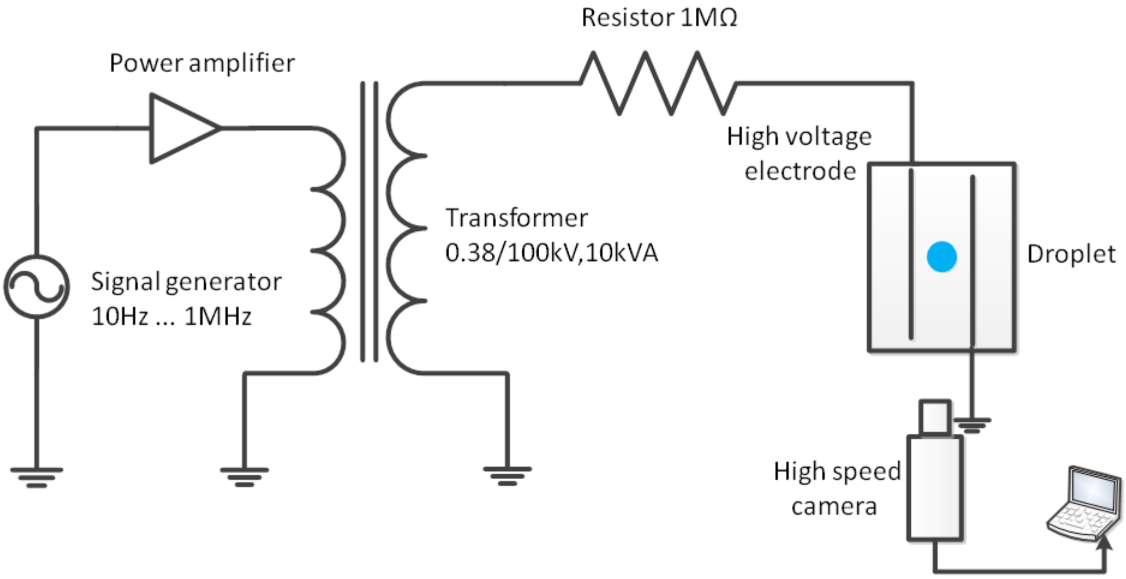

Figure 6.1.: Experimental set-up, (image from [13])

6.1.1 Experimental results

The analysis of the experimental results carried out at the High Voltage Lab of TU-Darmstadt agrees with the findings reported in [6] for the horizontal arrangement and extends them to the vertical arrangement.

The first finding is that the droplet motion consists of several modes of resonance. The main mode, corresponding to the largest deformation, has in most cases a resonance frequency double the frequency of the applied AC voltage.

The second finding concerns those cases where the main mode has a resonance frequency about the same as the applied AC voltage. This result is attributed in [6] to the accidental charging of the water droplet, e.g., by low charge partial discharges.

6.1.2 Simulation set-up

The computational domains corresponding to the horizontal and vertical arrangements include the insulator block, the $20\mu l$ water droplet and the two electrodes modeled as described in the previous section. In both cases, the fluid flow simulation ignore the two electrodes and the insulator block which are rigid bodies.

The shape of the droplet at the initial time of the simulation is found by calculating its equilibrium shape according to the algorithm described in section 4.3. In this calculation, one assumes a contact angle of $100°$. This equilibrium contact angle is measured on the video recordings of the droplet at the start of the experiment. The initial droplet shape is shown in Figure 6.2.

The initial droplet equatorial radius and initial height are $R_{max} = 2.58903mm$ and $R_{apex} = 2.1068mm$, respectively. The droplet is centered in a rectangular computational domain of dimensions $6 \times 6 \times 3mm$. For comparison, the radius of a semi-spherical droplet of $20\mu l$ is $R = 2.1215mm$.

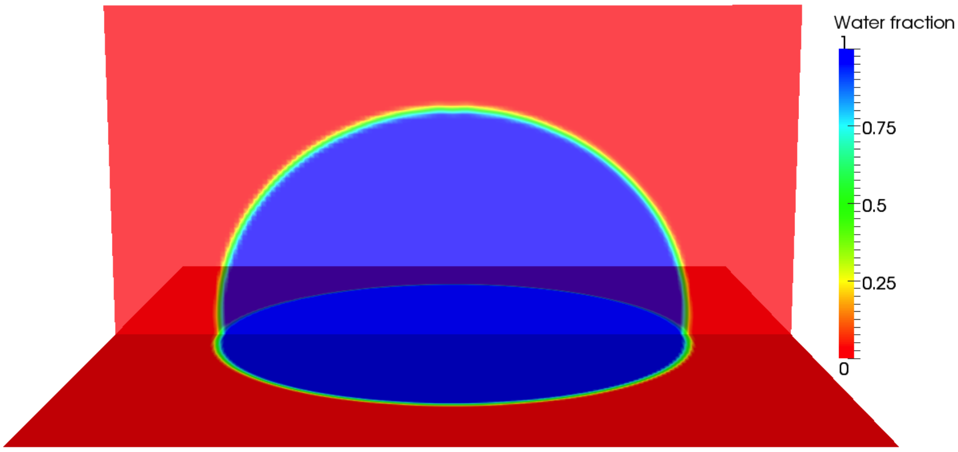

Figure 6.2.: Profile numerically calculated of a $20\mu l$ water droplet in equilibrium lying on a solid support with a contact angle of $100°$.

The computational domain is discretized using a fixed Cartesian grid with an equal grid spacing of $\Delta = \frac{3}{70}mm$ in all directions . This corresponds to a $140 \times 140 \times 70$ grid size.

The water fraction is initialized in each grid cell by calculating the exact water fraction $\gamma_{equilibrium}$ over each cell Ω_v as follows:

$$\gamma_{equilibrium} = \frac{1}{\Delta^3} \iiint_{\Omega_v} 1_{[0,R(\Theta)]} \left(M\left(r, \Theta, \Phi\right)\right) dxdydz \, . \tag{6.1}$$

where $1_{[0,R(\Theta)]}$ is the indicator function defined in spherical coordinates and corresponding to the profile of an axisymmetrical droplet in equilibrium.

6.1.3 Simulation results

In both arrangements, the applied AC voltage is modeled in the time domain by a ramped sinus profile of the same frequency. The risetime of the applied voltage has a duration of 5 periods as shown in figure 6.3:

The water droplet is simulated in the vertical and horizontal arrangements with an applied AC voltage of frequency $f_{AC} = 50Hz$ and $f_{AC} = 100Hz$. These frequencies are chosen to match the frequencies used in the experimental set-up described in section 6.1.

We characterize the droplet vibrations by recording the droplet height over the duration of the simulation. The latter is defined as the distance between the center of the contact line and the droplet surface in the direction normal to the insulator surface. In a first step the droplet height is recorded as a function of time over the duration of the simulation. In a second step the

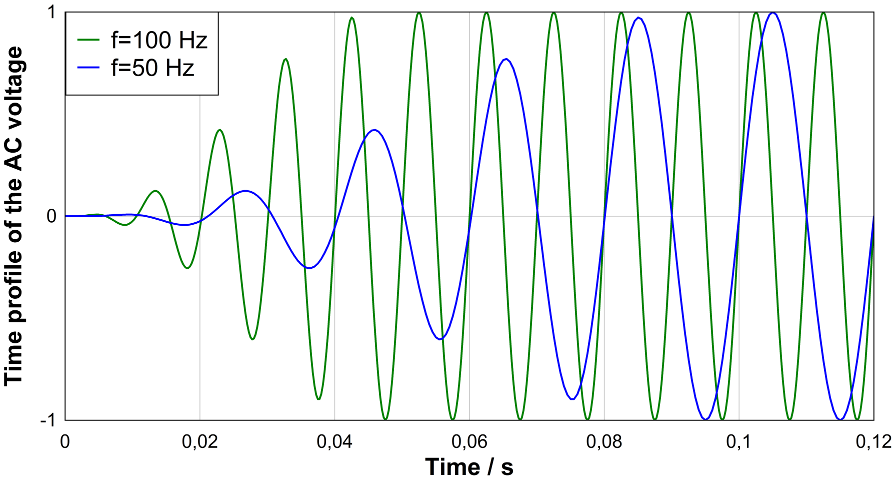

Figure 6.3.: Normalized time profile of the applied AC voltage at $50Hz$ and $100Hz$.

variation of the droplet height is calculated over the duration of the simulation as the relative deviation of the droplet height with respect to its mean height.

Low light conditions in the case of the vertical arrangement greatly reduced the contrast of the droplet snapshots which prevented from performing accurate visual comparisons.

6.1.3.1 Results at 100 Hz

A visual comparison between simulation and experimental results in the case of the horizontal arrangement is illustrated in Figure 6.4. The simulated 3D droplet shape at three different time instants separated by $1.25ms$ (top) and the corresponding droplet image recorded in the experiment (bottom) are compared. The simulation is able to capture the correct shape deformation in the course of the droplet oscillation.

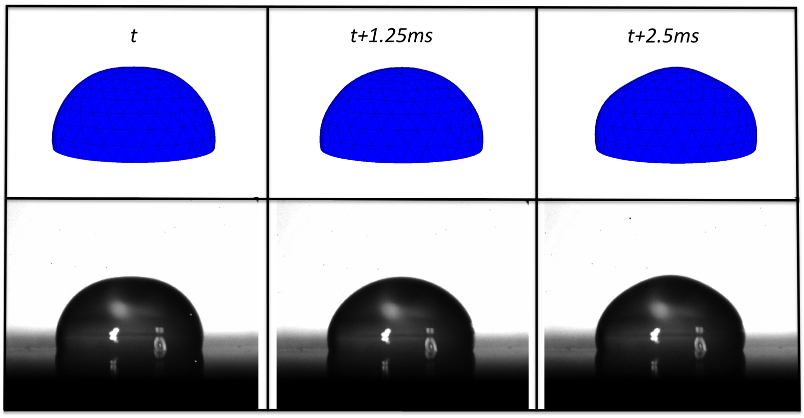

Figure 6.4.: Simulation and experimental results for the oscillation of $20\mu l$ water droplet under horizontal 100 Hz electric field stress; simulation (top) and experimental results (bottom); snapshots are separated by $1.25ms$. (Bottom images from [13])

The variation of the droplet height is shown for the vertical and horizontal arrangement in Figures 6.5 and 6.6, respectively. For both arrangements, one observes that the deformation of the droplet is nearly periodic and consists of different harmonics.

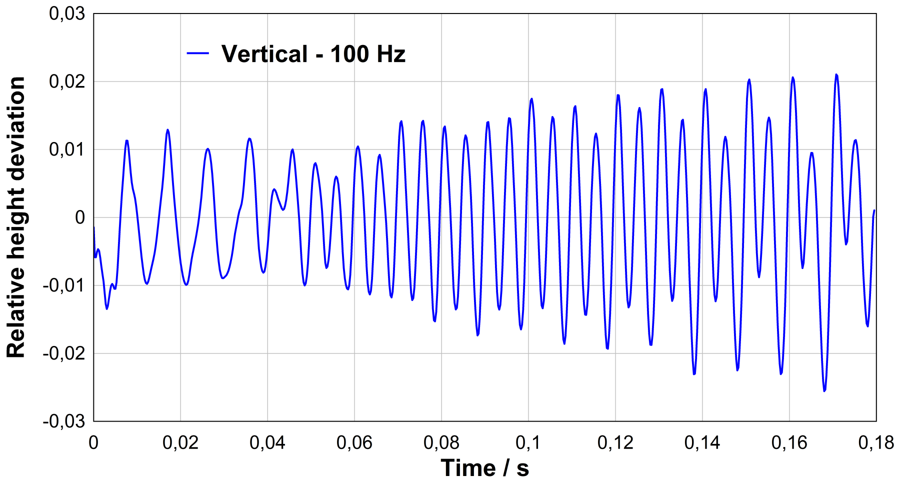

Figure 6.5.: Relative droplet height deviation w.r.t. its mean height for the vertical field arrangement.

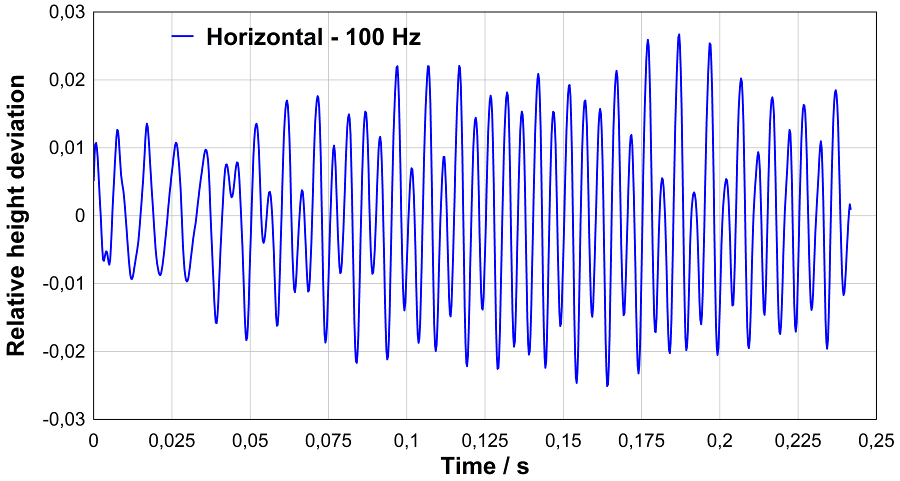

Figure 6.6.: Relative droplet height deviation w.r.t. its mean height for the horizontal field arrangement.

The droplet resonance frequencies are calculated by performing a Fourier transform of the relative droplet height deviation with respect to its mean height. The normalized vibration response spectrum is shown in the Figures 6.7 and 6.8 for the vertical and horizontal arrangements, respectively. For both vertical and horizontal arrangements the frequency of the main resonance is exactly double the frequency of the applied AC voltage . This is in full agreement with the experimental data. In addition, the main resonance coexists with resonances at lower and higher frequencies which are the same for both arrangements. A resonance appears near $100Hz$ in both arrangements as a double peak due to the low spectral resolution.

6.1.3.2 Results at 50 Hz

A visual comparison between simulation and experimental results in the case of the horizontal arrangement is illustrated in Figure 6.9. The simulated 3D droplet shape at three different time

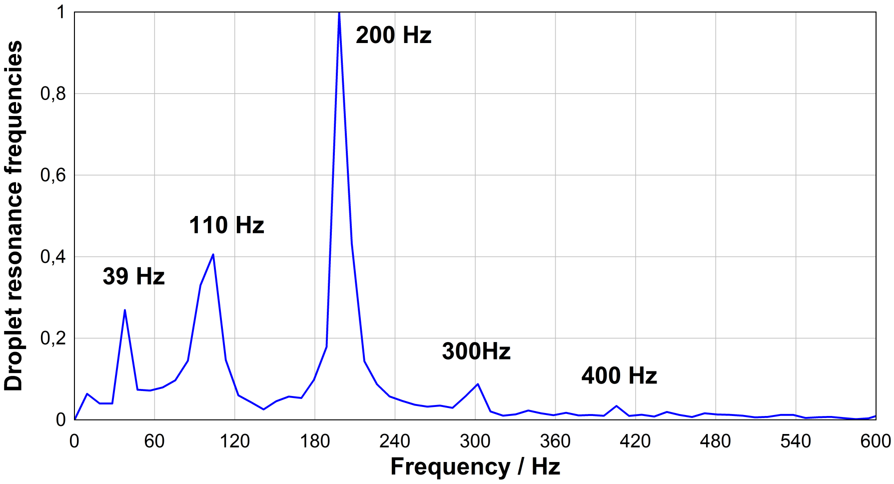

Figure 6.7.: Normalized vibration response spectrum for the vertical field arrangement at $100Hz$.

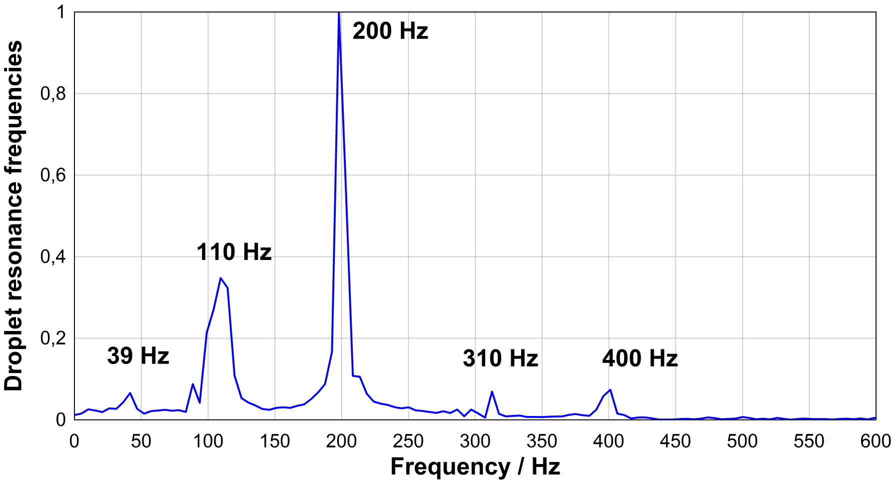

Figure 6.8.: Normalized vibration response spectrum for the horizontal field arrangement at $100Hz$.

instants separated by $2ms$ (top) and the corresponding droplet image recorded in the experiment (bottom) are compared. The simulation is able to capture the correct shape deformation in the course of the droplet oscillation.

The variation of the droplet height is shown for the vertical and horizontal arrangement in the Figures 6.10 and 6.11, respectively. For both arrangements, one observes that the deformation of the droplet consists of different harmonics.

The droplet resonance frequencies are calculated by performing a Fourier transform of the relative droplet height deviation with respect to its mean height. The normalized vibration response spectrum is shown in the Figures 6.12 and 6.13 for the vertical and horizontal arrangements, respectively. For both arrangements, the frequency of the main resonance is exactly double the frequency of the applied AC voltage. This is in full agreement with the experimental data. In the case of the horizontal field arrangement, a lowest and strongest resonance is observed at about double the external voltage frequency.

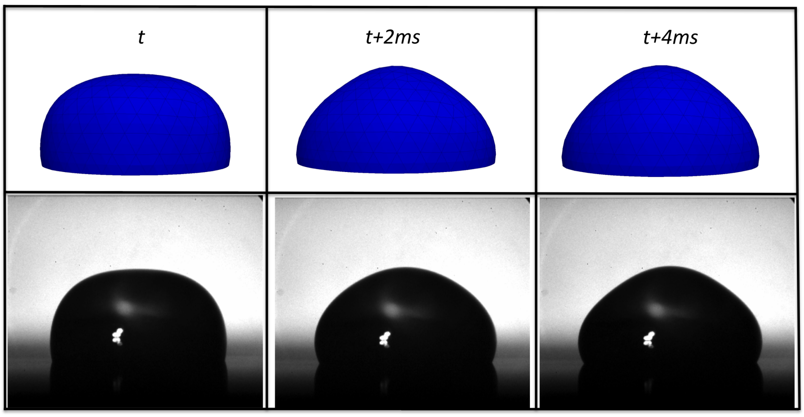

Figure 6.9.: Simulation and experimental results for the oscillation of $20\mu l$ water droplet under horizontal 50 Hz electric field stress;snapshots are separated by $2ms$; simulation (top) and experimental results (bottom) separated by $2ms$. (Bottom images from [13])

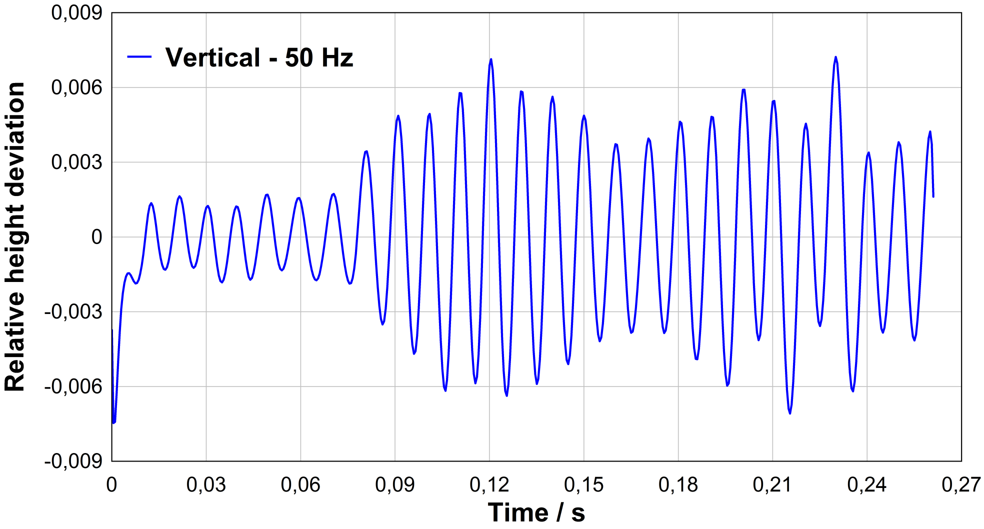

Figure 6.10.: Relative droplet height deviation w.r.t. its mean height for the vertical field arrangement.

6.2 Discussion

This section is devoted to the analysis of the vibrations of water droplets. In the first part, we apply the linear mechanical model of water droplet vibration proposed in [6] to study the steady-state regime. We refine the model to characterize the transient regime and show that the droplet oscillations are strongly underdamped. We find that its relaxation time is about one and a half minute which is large enough for the transient response to influence the simulation as well as the experimental results.

In the second part, we study the transient response of the droplet. We calculate numerically the resonance frequencies of the droplet oscillating freely in the absence of electric field and show that these free oscillation modes may contribute to the vibration response spectrum of the electrically driven cases.

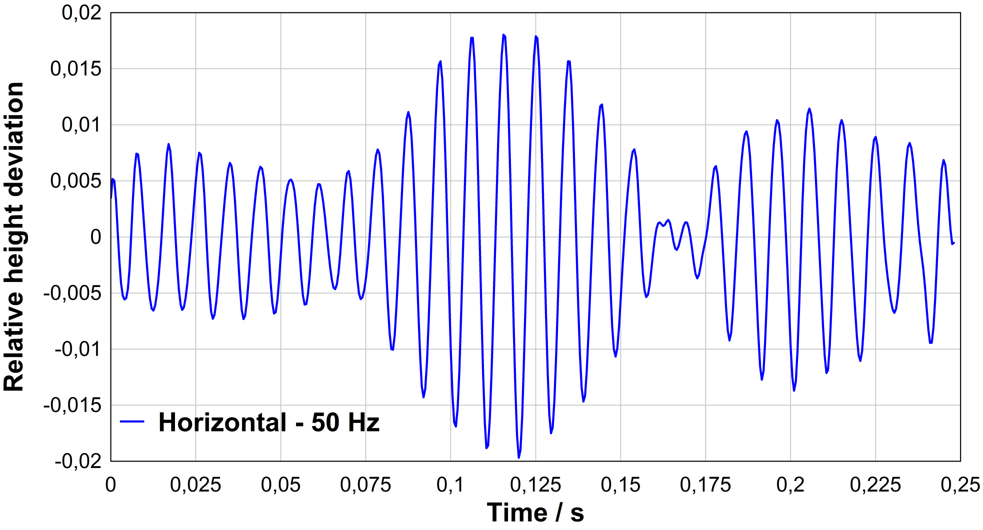

Figure 6.11.: Relative droplet height deviation w.r.t. its mean height for the horizontal field arrangement.

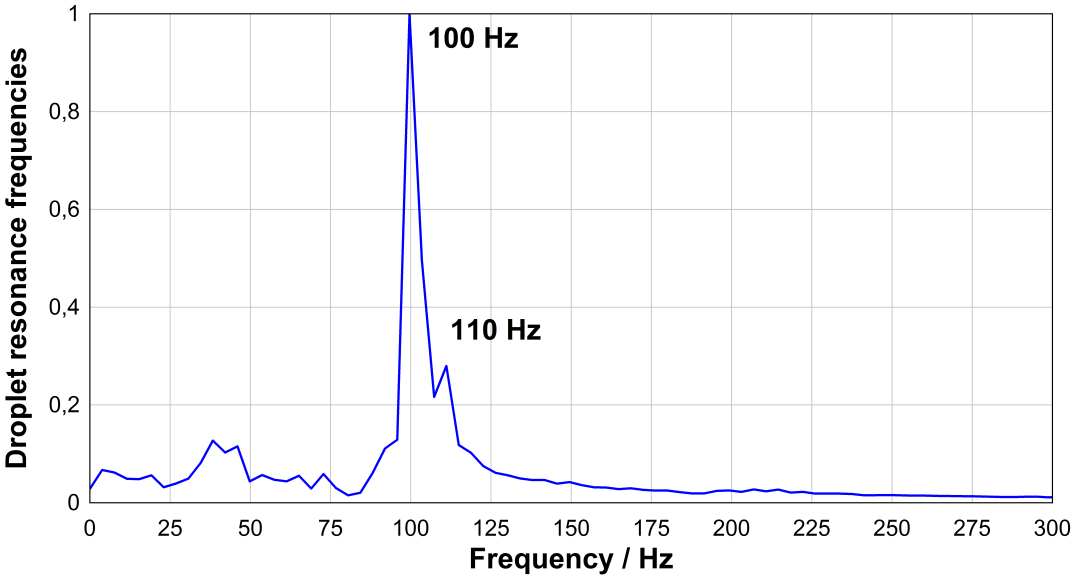

Figure 6.12.: Normalized vibration response spectrum for the vertical field arrangement at $50Hz$.

6.2.1 Linear model of the droplet deformations

A linear analysis of the droplet deformation has been carried out in [6]. It considers only the steady-state response and assumes that the deformation of the droplet can be described by a driven harmonic oscillator model.
The equation describing the motion of the driven harmonic oscillator is as follows:

$$M\frac{d^2x}{dt^2} = f - D\frac{dx}{dt} - Kx, \tag{6.2}$$

where M is the mass, x is displacement of the point of interest on the water droplet, t is the time, f is the driving force, D is the damping constant and K is the spring constant.

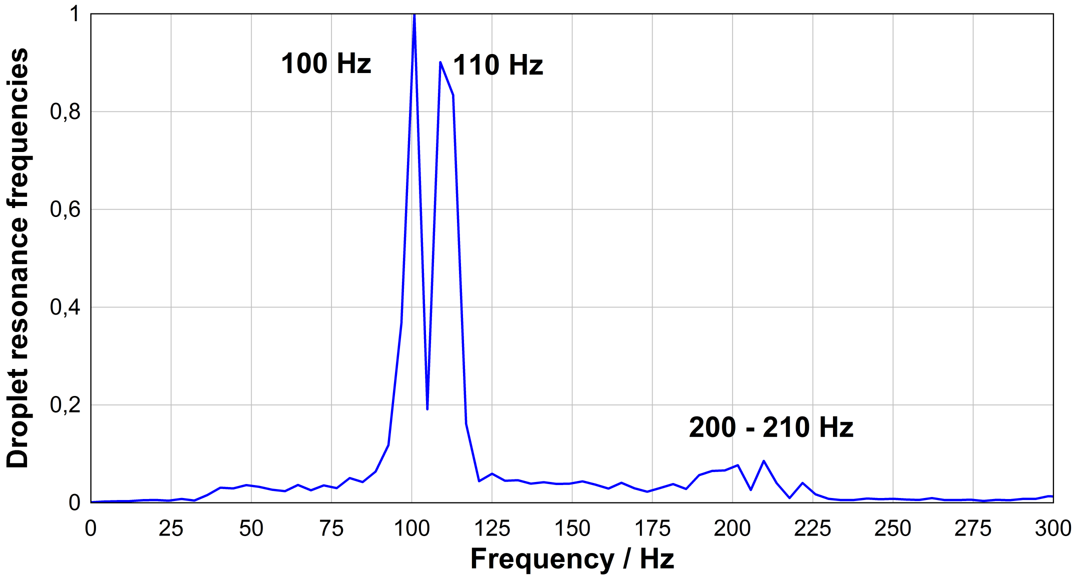

Figure 6.13.: Normalized vibration response spectrum for the horizontal field arrangement at $50Hz$.

The equation (6.2) can be rewritten as:

$$\frac{d^2x}{dt^2} + 2\zeta w_0 \frac{dx}{dt} + w_0^2 x = \frac{f}{M}, \tag{6.3}$$

where $w_0 = \sqrt{\frac{K}{M}}$ is the undamped angular frequency of the oscillator and $\zeta = \frac{D}{2\sqrt{MK}}$ is the damping ratio.

In the case of water droplets, the driving force is given by the electric force density (section 2.1.4) which takes the following form:

$$\vec{f_v} = \frac{1}{2}\left(\varepsilon - \varepsilon_0\right) \vec{\nabla}\left(\vec{E}\cdot\vec{E}\right). \tag{6.4}$$

In the case of an AC applied voltage, the electric field can be written as $\vec{E} = \vec{E}_0 \sin\left(w_{AC} t\right)$, with $w_{AC} = 2\pi f_{AC}$ and where f_{AC} is the frequency of the externally applied AC voltage. Thus, the driving force is:

$$f = F_0 \sin^2\left(w_{AC} t\right) = \frac{F_0}{2}\left(1 - \cos(2w_{AC} t)\right), \tag{6.5}$$

where the driving amplitude F_0 is proportional to the medium's permittivity and to the gradient of the squared electric field in the droplet.

The steady-state solution of the equation (6.3) is:

$$x\left(t\right) = \frac{F_0}{2w_{AC} M Z} \sin\left(2w_{AC} t + \varphi\right), \tag{6.6}$$

where φ is a phase shift and $Z = \sqrt{\left(2\zeta w_0\right)^2 + \frac{1}{4w_{AC}^2}\left(w_0^2 - 4w_{AC}^2\right)}$.

The steady-state solution (6.6) accounts for deformations occurring at twice the frequency of the externally applied voltage. The simulation results presented in the section 6.1.3 show, as expected, that the main frequency of $2f_{AC}$ corresponds to the frequency of the driving force. However the simulation results and the experimental results reported in section 6.1.1 show that resonances at frequencies lower than $2f_{AC}$ may be present.

In order to understand this behavior, we provide the following estimation for the parameters of equation (6.2) based on the characteristics of the water droplet: M is the mass $\varrho_{water}V$ of the water droplet where $\varrho_{water} = 998kg/m^3$ and $V = 20\mu l$, K is the surface tension of water $\sigma = 0.07071N/m$ and the damping constant is the coefficient of the frictional force exerted by the surrounding air as the droplet oscillates. We approximate the frictional force acting on the droplet by applying Stokes' law on a sphere of same radius $r = 2.1215mm$ which yields the drag force $F_d = 6\pi r\mu_{air}\frac{dx}{dt}$ where $\mu_{air} = 1.83e^{-5}kg/m/s$ is the dynamic viscosity of air. Since the water droplet may be approximately represented by a half sphere we take $D \approx 3\pi r\mu_{air}$.

The model (6.3) applied to the water droplet yields $w_0 = 59rad/s$ and a very low damping ratio $\zeta = 1.5e^{-4} \ll 1$ which indicates that the oscillations are strongly underdamped. The relaxation time is $\tau = \frac{1}{\zeta w_0} = 109s$ which is much larger than the simulated time and is large enough to influence the experimental results as well if there is not enough time to dampen the droplet oscillations due to the initial conditions before the start of the video recording. Thus, the steady-state solution (6.6) of the model equations may not be sufficient to explain the full vibration spectrum observed in the experiments as well as computed in the simulations.

6.2.2 Free oscillations of the sessile water droplet

In the absence of electric field, the water droplet on the horizontal surface of the insulator is in equilibrium. When a small perturbation is applied, for instance by a small puff of air, the droplet returns to its original state in a oscillating manner. We apply the EHD solver to simulate the free oscillations of the water droplet and to determine their resonant modes. The simulation set-up only differs from the electrically driven case described in section 6.1.2 by the absence of electric field (i.e., the externally applied AC voltage is set to 0) and by a different initial droplet shape. At the initial time of the simulation the shape of the water droplet is assumed to be a small pertubation of the equilibrium shape previously calculated in section 4.3. The profile of the pertubated droplet is shown in Figure 6.14.

The variation of the droplet height as the droplet returns to the equilibrium is shown in Figure 6.15. As expected one observes that the oscillations of the droplet are nearly periodic and consists of different harmonics. Furthermore, for the simulated time of $0.27s$, the droplet oscillation appears to be almost undamped.

The free droplet resonance frequencies are calculated by performing a Fourier transform of the relative droplet height deviation with respect to its mean height. The normalized vibration response spectrum is shown in the Figure 6.16. We note that the frequency of the resonance with the largest amplitude occurs at $110Hz$.

The free oscillations of a liquid sphere immersed in a fluid have been determined analytically by Lamb [28]. In the case of a liquid sphere of density ϱ_i surrounded by an outer fluid of density

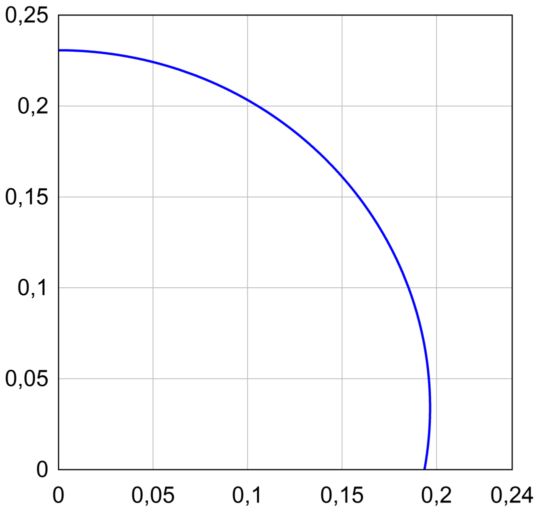

Figure 6.14.: Axisymmetrical profile of a $20\mu l$ water droplet with an initial displacement from the equilibrium and lying on a solid support with a contact angle of $100°$.

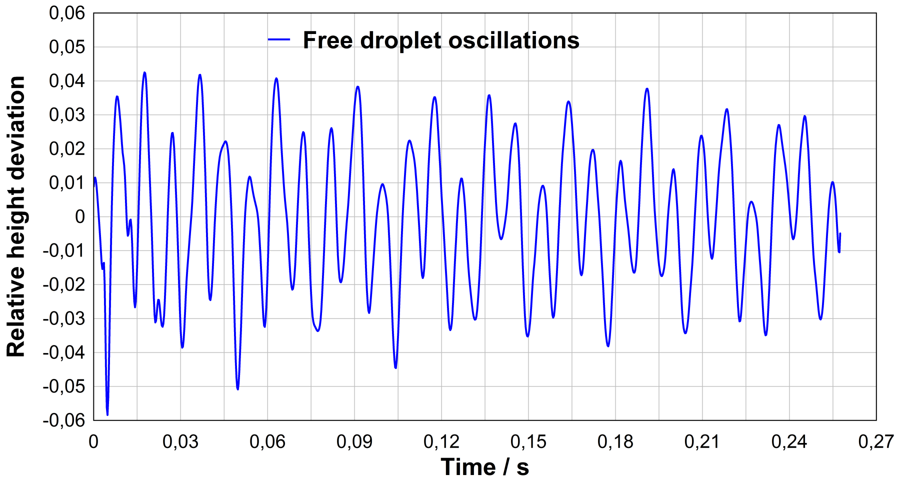

Figure 6.15.: Relative droplet height deviation w.r.t. its mean height when the droplet is oscillating freely.

ϱ_e, both fluids being inviscid, Lamb obtained the following frequencies of the resonance modes n with $n \geq 2$:

$$f_n = \frac{1}{2\Pi}\sqrt{\frac{n(n-1)(n+1)(n+2)}{(n+1)\varrho_i + n\varrho_e}\frac{\sigma}{r^3}}, \tag{6.7}$$

where σ is the surface tension and r is the radius of the sphere.
Assuming $\varrho_i = 998kg/m^3$, $\varrho_e = 1.2kg/m^3$, $\sigma = 0.0707N/m$ and $r = 0.0021215m$, the lowest three resonance frequencies of a water droplet freely oscillating in air according to Lamb's model are shown in Figure 6.17.
The case of a droplet immersed in an outer fluid and in partial contact with a spherical solid support has been investigated analytically by Strani and Sabetta [29]. They showed that the

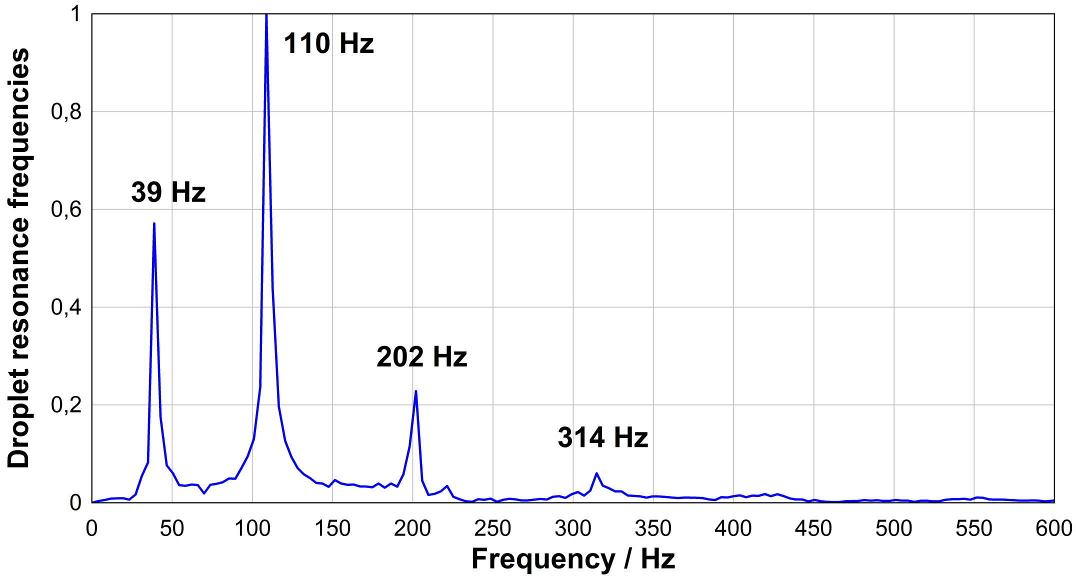

Figure 6.16.: Normalized vibration response spectrum when the droplet is oscillating freely.

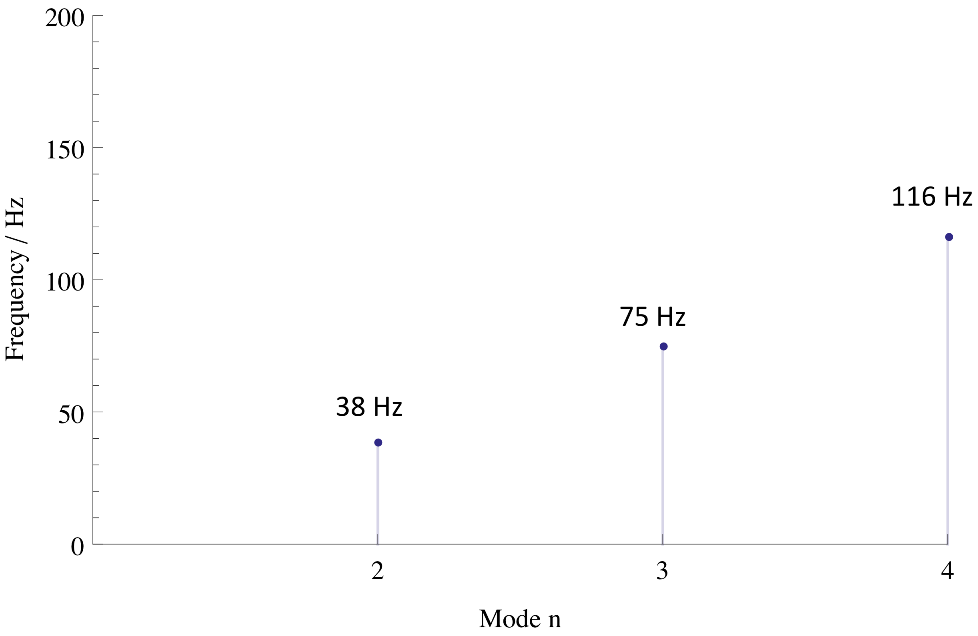

Figure 6.17.: Lowest resonance frequencies of a water droplet freely oscillating in air according to Lamb's model [28].

solid support introduces a new low frequency mode and increases the mode frequencies for all higher modes with respect to the cases without contact to a solid support (shown in Figure

6.17). Moreover, when the size of the supported portion of the droplet tends to zero, the first mode tends to a zero-frequency rigid displacement while the other mode frequencies (i.e. $n \geq 2$) tend to the resonant frequencies obtained by Lamb [28].
Recently Kim, Yang and Chung [30] have developed a simple semi-analytical model fitted to experimental results which provides a rough estimate of the nth mode resonant frequency as a function of the contact angle ϑ:

$$f_n = \frac{0.72}{2\Pi}\sqrt{\Pi^3(n-\frac{1}{2})^3\frac{1}{\vartheta^3}\frac{\sigma}{\varrho r^3}}, \tag{6.8}$$

where ϱ is the droplet density.

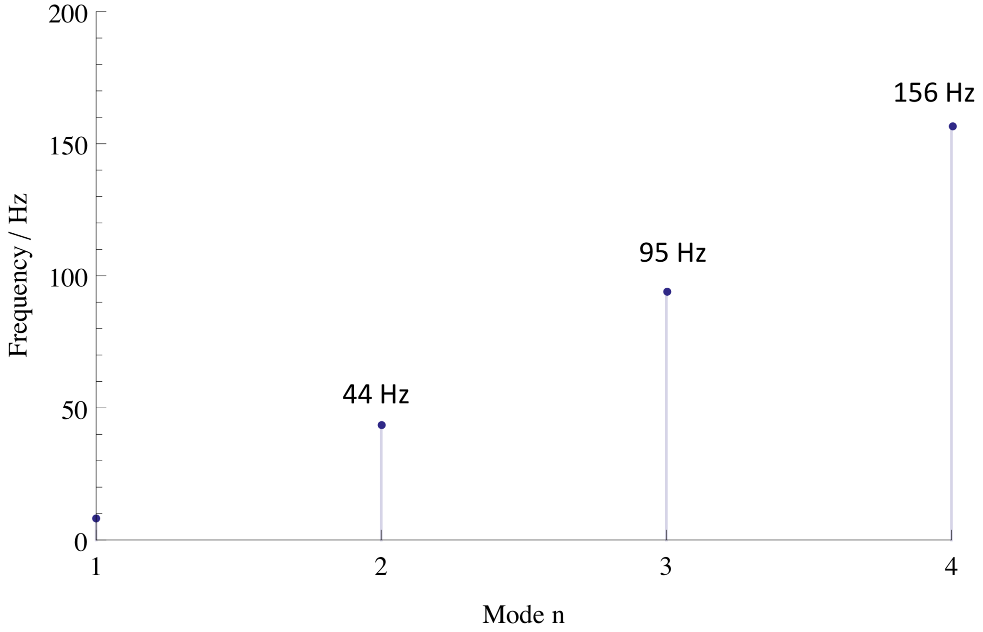

Figure 6.18.: Lowest three resonance frequencies of the water droplet freely oscillating on a solid support with an initial contact angle of $100°$ according to the semi-analytical model by Kim et al. [30].

The model (6.8) is found to be within five percent of the theoretical values calculated by Strani and Sabetta for a contact angle in the range of $\vartheta = 15 - 80°$. Despite its simplicity, we expect the model to provide a reasonable estimate of the resonant frequencies for the contact angle $\vartheta = 100°$ used as the initial contact angle in the simulation of the free oscillating water droplet. Assuming $\varrho = 998kg/m^3$, $\vartheta = 100°$, $\sigma = 0.0707N/m$ and $r = 0.002125m$, the frequencies of the resonant modes calculated by the semi-analytical model (6.8) are $44Hz$, $95Hz$ and 156, respectively (see Figure 6.18). They agree reasonably well with the frequencies of the resonant modes $39Hz$, $110Hz$, and $202Hz$ respectively, obtained from the simulation of the free oscillating water droplet as shown in Figure 6.16.

The resonant modes of the free oscillating water droplet with the largest and second largest amplitude occur at $110Hz$ and $39Hz$, respectively. In the electrically driven cases the driving frequency is either $2f_{AC} = 100Hz$ or $2f_{AC} = 200Hz$. The resonant mode whose frequency is the farthest from the driving frequency will be comparatively attenuated the most. Thus, it is expected that only the resonant mode occuring at $110Hz$ appears in the vibration response spectrum of the electrically driven cases. Indeed, it coincides with the low frequency resonance appearing in the Figures 6.7, 6.8, 6.12 and 6.13.

We have shown that the vibrations of the droplet occuring at frequencies below $2f_{AC}$ are not necessarily due to the presence of free charges induced by phenomena such as ionization or accidental charging of the water droplet, e.g., by low charge partial discharges as suggested in [6]. Rather, they may be caused by underdamped droplet oscillations which originate in the transient regime. This finding is further supported by the fact that their frequencies correspond to the resonance frequencies of the sessile droplets oscillating freely.

7 Summary

In this thesis, a computational method has been proposed to solve numerically in the time domain the coupled system composed of the full sets of electro-quasistatics and Navier-Stokes equations. The method has been experimentally validated by simulating the complicated oscillatory motion of a water droplet placed on the surface of an insulator in presence of a strong electric field.

This novel method makes it possible for the first time to simulate the water droplet deformations under the influence of transient high-voltage electric fields.

A mathematical model for the electrohydrodynamic problem of rainwater droplet vibrations on polymer insulators has been presented. In particular, we offer three expressions based on the volume force densities, the surface force densities and the Maxwell Stress Tensor to calculate the electric force causing the droplet deformations. The choice of the force calculation depends mostly on how the water droplet interface is modeled. A calculation based on the volume or surface force densities is well-suited when the droplet interface is modeled by a sharp interface whereas a calculation based on the Maxwell Stress Tensor is better suited when the droplet interface is modeled by an interface capturing scheme.

We have described how to apply the Finite Element Method to solve the electro-quasistatics equation on a moving curvilinear mesh and how to derive the electric force without loss of accuracy with respect to the FEM approximation.

An overview of the multiphase flow solver employed to solve the fluid dynamics problem has been given. The Navier-Stokes equation are solved by using the finite volume mesh on a fixed Cartesian grid, the time-evolution of the droplet interface is computed by using an interface capturing scheme based on the volume of fluid method. The behavior of the droplet surface tension at the insulator surface is taken into account by a dynamic contact line model.

The solution of the coupled electrical and fluid mechanical problem is achieved in a time-accurate manner by leapfrogging the electro-quasistatics and the multiphase flow solver in a synchronized manner. A novel mesh adaptation procedure was devised to maintain a consistent representation of the droplet shape in the finite element mesh used by the electro-quasistatic solver as well as in the Cartesian grid used by the fluid dynamic solver.

The proposed computational method is validated by showing that the predicted resonance frequencies of the droplet vibrations agree with the experimental resonance frequencies. The simulation results are further analyzed by applying a one-dimensional mechanical model of water droplet deformation based on the linear harmonic oscillator. This model is used to characterize the steady-state as well as the transient oscillation regime of the free droplet. It is shown that droplet vibrations occuring at frequencies below the driving frequency are not necessarily due to the accidental charging of the water droplet as it is sometimes suggested in the literature. Rather, they may be caused by underdamped droplet oscillations which originate in the transient regime. This finding is further supported by the fact that their frequencies correspond to the resonance frequencies of the sessile water droplets oscillating freely.

A Appendix

A.1 Global to local coordinate mapping

We present an algorithm to find the local coordinates $\zeta = (\zeta_1, \zeta_2, \zeta_3)$ in a quadratic tetrahedron T of the point having coordinates $x = (x_1, x_2, x_3)$ in the computational domain. The quadratic tetrahedron T is shown in figure A.1:

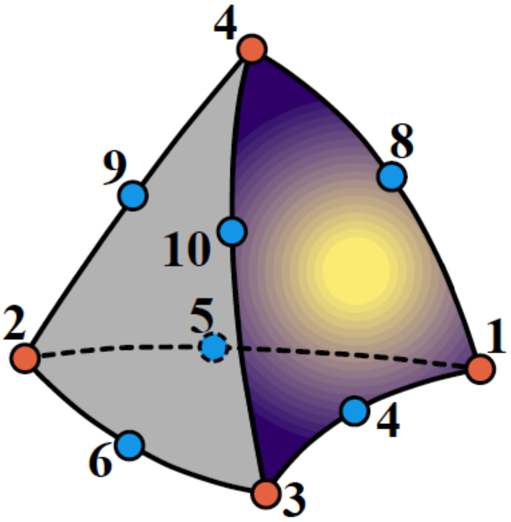

Figure A.1.: The quadratic tetrahedron, (image from [19])

We define the following shape functions on the quadratic tetrahedron:

$$N_i = l_i (2l_i - 1), \; 1 \leq i \leq 4 \tag{A.1}$$

$$N_5 = 4l_1 l_2, \; N_6 = 4l_2 l_2, \; N_7 = 4l_3 l_1, \; N_8 = 4l_1 l_4, \; N_9 = 4l_2 l_4, \; N_{10} = 4l_3 l_4 \tag{A.2}$$

$$l_i = \zeta_i, \; 1 \leq i \leq 3 \text{ and } l_4 = 1 - \zeta_1 - \zeta_2 - \zeta_3 \tag{A.3}$$

where the ζ_i, $1 \leq i \leq 3$ are the barycentric or local coordinates of the tetrahedron.
The geometrical transformation F_T defined in the Cartesian frame $(O, \vec{e}_1, \vec{e}_2, \vec{e}_2)$ maps any point of the reference tetrahedral element $\zeta = (\zeta_1, \zeta_2, \zeta_3)$ to $x = (x_1, x_2, x_3)$ in the tetrahedron T of the computational domain:

$$\mathsf{F}_T : [0,1]^3 \rightarrow T \tag{A.4}$$

$$(\zeta_1, \zeta_2, \zeta_3) \rightarrow (x_1, x_2, x_3) \text{ with } x_i = \sum_{j=1}^{10} x_{ij} N_j (\zeta_1, \zeta_2, \zeta_3), \; 1 \leq i \leq 3 \tag{A.5}$$

where the $(x_{ij})_{1 \leq j \leq 3}$ are the coordinates of the nodes M_i, $1 \leq i \leq 10$ forming the tetrahedron T.

The Jacobian J of the geometrical transformation F_T is:

$$\mathsf{J} \;=\; \begin{pmatrix} \sum\limits_{j=1}^{10} x_{1j}\vec{\nabla}N_j \\ \sum\limits_{j=1}^{10} x_{2j}\vec{\nabla}N_j \\ \sum\limits_{j=1}^{10} x_{3j}\vec{\nabla}N_j \end{pmatrix} \tag{A.6}$$

and its second derivative is:

$$\begin{pmatrix}\mathsf{H}_1 & \mathsf{H}_2 & \mathsf{H}_3\end{pmatrix} \;=\; \begin{pmatrix} \frac{\partial}{\partial \zeta_1}(\mathsf{J}) & \frac{\partial}{\partial \zeta_2}(\mathsf{J}) & \frac{\partial}{\partial \zeta_3}(\mathsf{J}) \end{pmatrix} \tag{A.7}$$

$$\begin{pmatrix}\mathsf{H}_1 & \mathsf{H}_2 & \mathsf{H}_3\end{pmatrix} \;=\; \left(\begin{pmatrix} \sum\limits_{j=1}^{10} x_{1j}\frac{\partial}{\partial \zeta_1}\vec{\nabla}N_j \\ \sum\limits_{j=1}^{10} x_{2j}\frac{\partial}{\partial \zeta_1}\vec{\nabla}N_j \\ \sum\limits_{j=1}^{10} x_{3j}\frac{\partial}{\partial \zeta_1}\vec{\nabla}N_j \end{pmatrix} \begin{pmatrix} \sum\limits_{j=1}^{10} x_{1j}\frac{\partial}{\partial \zeta_2}\vec{\nabla}N_j \\ \sum\limits_{j=1}^{10} x_{2j}\frac{\partial}{\partial \zeta_2}\vec{\nabla}N_j \\ \sum\limits_{j=1}^{10} x_{3j}\frac{\partial}{\partial \zeta_2}\vec{\nabla}N_j \end{pmatrix} \begin{pmatrix} \sum\limits_{j=1}^{10} x_{1j}\frac{\partial}{\partial \zeta_3}\vec{\nabla}N_j \\ \sum\limits_{j=1}^{10} x_{2j}\frac{\partial}{\partial \zeta_3}\vec{\nabla}N_j \\ \sum\limits_{j=1}^{10} x_{3j}\frac{\partial}{\partial \zeta_3}\vec{\nabla}N_j \end{pmatrix} \right) \tag{A.8}$$

where the first and second partial derivatives of the shape functions are:

$$\vec{\nabla}N_1 = \begin{pmatrix}4l_1-1 & 0 & 0\end{pmatrix}, \qquad \frac{\partial}{\partial \zeta_i}\vec{\nabla}N_1 = 4\begin{pmatrix}\delta_{i1} & 0 & 0\end{pmatrix} \tag{A.9}$$

$$\vec{\nabla}N_2 = \begin{pmatrix}0 & 4l_2-1 & 0\end{pmatrix}, \qquad \frac{\partial}{\partial \zeta_i}\vec{\nabla}N_2 = 4\begin{pmatrix}0 & \delta_{i2} & 0\end{pmatrix} \tag{A.10}$$

$$\vec{\nabla}N_3 = \begin{pmatrix}0 & 0 & 4l_3-1\end{pmatrix}, \qquad \frac{\partial}{\partial \zeta_i}\vec{\nabla}N_3 = 4\begin{pmatrix}0 & 0 & \delta_{i3}\end{pmatrix} \tag{A.11}$$

$$\vec{\nabla}N_4 = -\begin{pmatrix}4l_1+1 & 4l_2+1 & 4l_3+1\end{pmatrix}, \qquad \frac{\partial}{\partial \zeta_i}\vec{\nabla}N_4 = -4\begin{pmatrix}\delta_{i1} & \delta_{i2} & \delta_{i3}\end{pmatrix} \tag{A.12}$$

$$\vec{\nabla}N_5 = 4\begin{pmatrix}l_2 & l_1 & 0\end{pmatrix}, \qquad \frac{\partial}{\partial \zeta_i}\vec{\nabla}N_5 = 4\begin{pmatrix}\delta_{i2} & \delta_{i1} & 0\end{pmatrix} \tag{A.13}$$

$$\vec{\nabla}N_6 = 4\begin{pmatrix}0 & l_3 & l_2\end{pmatrix}, \qquad \frac{\partial}{\partial \zeta_i}\vec{\nabla}N_6 = 4\begin{pmatrix}0 & \delta_{i3} & \delta_{i2}\end{pmatrix} \tag{A.14}$$

$$\vec{\nabla}N_7 = 4\begin{pmatrix}l_3 & 0 & l_1\end{pmatrix}, \qquad \frac{\partial}{\partial \zeta_i}\vec{\nabla}N_7 = 4\begin{pmatrix}\delta_{i3} & 0 & \delta_{i1}\end{pmatrix} \tag{A.15}$$

$$\vec{\nabla}N_8 = -4\begin{pmatrix}(l_1-l_4) & l_1 & l_1\end{pmatrix}, \qquad \frac{\partial}{\partial \zeta_i}\vec{\nabla}N_8 = -4\begin{pmatrix}1+\delta_{i1} & \delta_{i1} & \delta_{i1}\end{pmatrix} \tag{A.16}$$

$$\vec{\nabla}N_9 = -4\begin{pmatrix}l_2 & (l_2-l_4) & l_2\end{pmatrix}, \qquad \frac{\partial}{\partial \zeta_i}\vec{\nabla}N_9 = -4\begin{pmatrix}\delta_{i2} & 1+\delta_{i2} & \delta_{i2}\end{pmatrix} \tag{A.17}$$

$$\vec{\nabla}N_{10} = -4\begin{pmatrix}l_3 & l_3 & (l_3-l_4)\end{pmatrix}, \qquad \frac{\partial}{\partial \zeta_i}\vec{\nabla}N_{10} = -4\begin{pmatrix}\delta_{i3} & \delta_{i3} & 1+\delta_{i3}\end{pmatrix} \tag{A.18}$$

where $l_i = \zeta_i$, $1 \leq i \leq 3$ and $l_4 = 1 - \zeta_1 - \zeta_2 - \zeta_3$

In the following, the coordinates of the nodes M_i, $1 \leq i \leq 10$ forming the tetrahedron T are divided by the maximum edge length in order to work with normalized quantities.
Finding the local coordinates of $x = (x_1, x_2, x_3)$ in the tetrahedra can be formulated as the following root finding problem:

$$\begin{aligned} \zeta &\in T \Leftrightarrow 0 \leq \zeta_i \leq 1,\ 1 \leq i \leq 3 \text{ and } 0 \leq 1 - \zeta_1 - \zeta_2 - \zeta_3 \leq 1 && \text{(A.19)} \\ \exists \zeta &\in T,\ \mathsf{F}_T(\zeta) = x && \text{(A.20)} \end{aligned}$$

In the case where the tetrahedon is linear the equation (A.20) admits a unique root in T or not at all. However, this is not the case for the quadratic tetrahedron because the Jacobian of geometrical transformation F_T can become singular. Therefore (A.20) may admit several roots outside of T. Alternatively, the problem of finding the local coordinates of $x = (x_1, x_2, x_3)$ in T can be formulated as a minimization problem:

$$\begin{aligned} g(\zeta) &= \sum_{i=1}^{3} \left(\mathsf{F}_T(\zeta)_i - x_i\right)^2 && \text{(A.21)} \\ \zeta^* &= \underset{\substack{0 \leq \zeta_i \leq 1,\ 1 \leq i \leq 3 \\ 0 \leq 1 - \zeta_1 - \zeta_2 - \zeta_3 \leq 1}}{\operatorname{argmin}} g(\zeta) && \text{(A.22)} \end{aligned}$$

where the gradient of g is:

$$\vec{\nabla} g = 2 \begin{pmatrix} \sum_{i=1}^{3} \left(\mathsf{F}_T(\zeta)_i - x_i\right) \mathsf{J}_{i1} \\ \sum_{i=1}^{3} \left(\mathsf{F}_T(\zeta)_i - x_i\right) \mathsf{J}_{i2} \\ \sum_{i=1}^{3} \left(\mathsf{F}_T(\zeta)_i - x_i\right) \mathsf{J}_{i3} \end{pmatrix} \qquad \text{(A.23)}$$

and its Hessian $\mathsf{H}(g)$ is:

$$\mathsf{H}(g)_{ij} = 2 \sum_{k=1}^{3} \mathsf{J}_{ki} \mathsf{J}_{kj} + \left(\mathsf{F}_T(\zeta)_k - x_k\right) \mathsf{H}_{k_{ij}},\ 1 \leq i, j \leq 3 \qquad \text{(A.24)}$$

The minimization problem is not equivalent to the root finding problem since it always admits at least one minimum which is not necessarily a root. Its interest lies with the numerical properties of the Hessian $\mathsf{H}(g)$ which is symmetrical, real and therefore always diagonalizable. This makes it possible to build an efficient pseudo-inverse when the Hessian is singular.
The proposed algorithm is based on the Newton-Raphson method applied to the root finding problem (A.20) or to the minimization problem (A.22) depending on the existence of the derivative. If the Jacobian becomes singular at a root estimate, the Hessian of the minimization problem is used. If the Hessian matrix is also singular, a pseudo-inverse of the Hessian is used to calculate the next estimate. The pseudo-inverse is constructed by replacing the zero eigenvalues of the Hessian by 1. In order to avoid starting the iterative scheme outside the basins of attractions of a possible root in T the initial estimate ζ^0 is chosen as the best estimate among a small number of points including the ten nodes of the tetrahedron and its barycenter.

```
$\zeta^0 = \underset{\substack{\zeta_i=j/3,\,0\le j\le 3,\,1\le i\le 3\\ 0\le 1-\zeta_1-\zeta_2-\zeta_3\le 1}}{\operatorname{argmin}} \|\mathsf{F}_T(\zeta)-x\|^2$
for $i \leftarrow 1$ to $i_{max}$ do          /* Iterate until eventual convergence or $\zeta^{n+1} \notin T$ */
    $\mathsf{J} \leftarrow \vec{\nabla}\mathsf{F}_T(\zeta^n)$
    if $|\det\mathsf{J}| > 10^{-3}$ then          /* Root finding approach */
        $\zeta^{n+1} \leftarrow \zeta^n - \mathsf{J}^{-1} \cdot \left(\mathsf{F}_T(\zeta^n) - x\right)$
    else
        $\mathsf{H} \leftarrow \mathsf{H}(g)$
        if $|\det\mathsf{H}| > 10^{-6}$ then          /* Minimization approach */
            $\zeta^{n+1} \leftarrow \zeta^n - \mathsf{H}^{-1} \cdot \vec{\nabla} g$
        else
                    /* $\mathsf{H}^{-1}$ is replaced by its pseudo-inverse $\mathsf{H}^{+}$ */)
            $\zeta^{n+1} \leftarrow \zeta^n - \mathsf{H}^{+} \cdot \vec{\nabla} g$
        end
    end
        /* Iterations stop if $\zeta^{n+1}$ falls outside $T$ or if $(\zeta^n)$ is converging */)
    if $\|\zeta^{n+1} - \zeta^n\| \le 10^{-9}$or $\neg\left(0 \le \zeta_i \le 1,\ 1 \le i \le 3 \text{ and } 0 \le 1 - \zeta_1 - \zeta_2 - \zeta_3 \le 1\right)$ then
        break while loop
    else
                    /* Linear search between $\zeta^n$ and $\zeta^{n+1}$ */)
        $\zeta^{n+1} \leftarrow \underset{\substack{\zeta=\zeta^n+\alpha\left(\zeta^{n+1}-\zeta^n\right)\\ 0\le\alpha\le 1}}{\operatorname{argmin}} \|\mathsf{F}_T(\zeta)-x\|^2$
    end
end
if $\|\mathsf{F}_T\left(\zeta^{n+1}\right) - x\| < 10^{-6}$and $\left(0 \le \zeta_i \le 1,\ 1 \le i \le 3 \text{ and } 0 \le 1 - \zeta_1 - \zeta_2 - \zeta_3 \le 1\right)$ then
                    /* $x \in T$ and its local coordinate are $\zeta^{n+1}$ */)
    return $\zeta^{n+1}$
else
                    /* $x \notin T$ */)
    return $\varnothing$
end
```

We present an algorithm to efficiently search through a tetrahedral mesh the tetrahedron T containing an arbitrary point P. In a preliminary step, the oriented normals $\vec{n}$ and the barycenters I of all faces are calculated. For this calculation the quadratic tetrahedron are linearized by only considering their four vertices.This makes it possible to use the face normals as search directions. A sketch of the algorithm for a triangular mesh is shown in Figures A.2 and A.3.

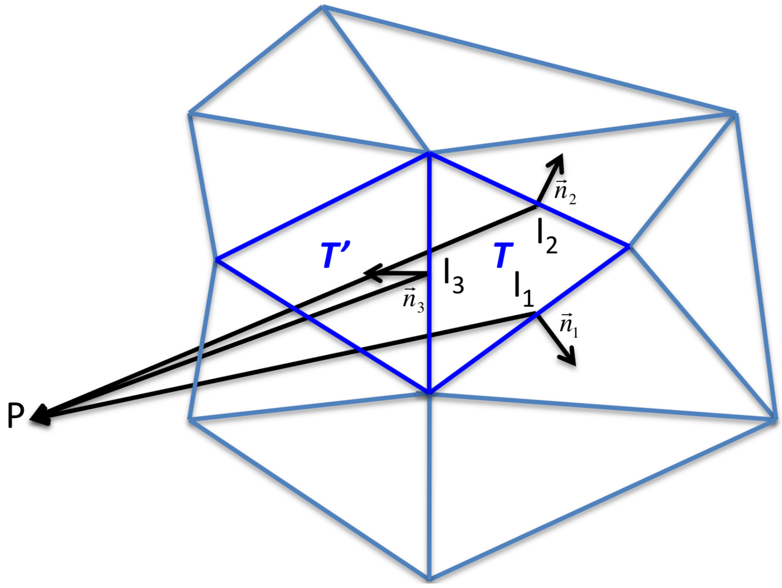

Figure A.2.: Selection of the best search direction toward P

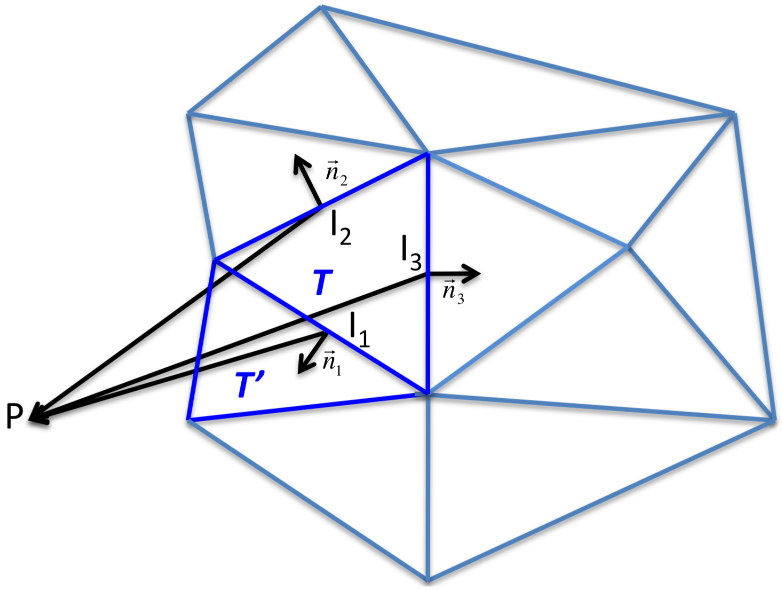

Figure A.3.: Selection of the next best search direction toward P

An important aspect of this algorithm is that it allows to visit the same tetrahedron several times without trying the same direction twice. This is necessary to handle the curved faces of quadratic tetrahedrons which are not determined by a unique normal. The algorithm typically converges in fewer than forty iterations. It is used in section 3.4.5 (finite element assembly) to locate in the previous mesh the quadrature point of the numerical integration of the right hand side. It is used similarly to locate in the current finite element mesh the quadrature point of the numerical integration of the Maxwell Stress Tensor performed in the Cartesian grid of the fluid dynamics solver.

```
Data: The point $P$ and a candidate tetrahedron $T$
Result: The tetrahedron $T$ containing P or $\varnothing$
Tested $\leftarrow \{\varnothing\}$
Visited $\leftarrow \{\varnothing\}$
while $T \neq \varnothing$ do
    if $P \in T$ then        /* Test if $P$ is in $T$ by using the algorithm described in appendix A.1 */
        return $T$
    else
        Tested $\leftarrow$ Tested $\cup\, T$
    end
    for $i \leftarrow 1$ to $4$ do                    /* Iterate on the faces $i$ of $T$ */
        $\alpha_i \leftarrow \vec{n}_i \cdot \overrightarrow{I_i P}$
    end
    $\alpha_{i_1} > \alpha_{i_2} > \alpha_{i_3} > \alpha_{i_4}$                    /* Decremental sort */
    $T' \leftarrow \varnothing$
    for $j \leftarrow i_1$ to $i_4$ do
                                /* $T_j$ is the neighbour of $T$ sharing the face $j$ */
        if $T_j \notin$ Tested then
            if $P \in T_j$ then                    /* Test if $P$ is in $T_j$ */
                $T \leftarrow T_j$
                return $T$
            else
                Tested $\leftarrow$ Tested $\cup\, T_j$
            end
        end
        if $T_j \notin$ Visited then
            $T' \leftarrow T_j$
            Visited $\leftarrow$ Visited $\cup\, T_j$
            break for loop
        end
    end
    $T \leftarrow T'$
end
```

A.3 Mesh smoothing algorithm

This algorithm is used to control the quality of the deformed mesh (see section 5.3).

```
Data: The point $Q$
Result: The point $Q'$ minimizing the cost function $\mathsf{C}$
$Q_0 \leftarrow Q$ , $Tol \leftarrow 5.10^{-3}$ , $\alpha \leftarrow 1$ , $\gamma \leftarrow 2$
for $i \leftarrow 1$ to $N$ do                /* Iterate on the $N$ faces of the polyhedron */
    $Q_i \leftarrow \frac{1}{2}\left(Q + G_i^f\right)$    /* $Q_i$ is an initial guess between $Q$ and the center $G_i^f$ of
    the face $i$ */
end
$\mathsf{C}\left(Q_{j_0}\right) < \ldots < \mathsf{C}\left(Q_{j_N}\right)$                /* Incremental sort */
for $i \leftarrow 1$ to $N$ do                /* Reassign from the best to the worst guess */
    $Q_i \leftarrow Q_{j_i}$
end
while $|\mathsf{C}\left(Q_0\right) - \mathsf{C}\left(Q_N\right)| \geq Tol \frac{|\mathsf{C}(Q_0)+\mathsf{C}(Q_N)|}{2}$ do    /* Calculation of the barycenter $G$
of all points except the one with the largest value */
    $G \leftarrow 0$
    for $i \leftarrow 0$ to $N-1$ do
        $G \leftarrow G + Q_i$
    end
    $G \leftarrow \frac{1}{N} G$
    $Q_r \leftarrow G + \alpha\left(G - Q_N\right)$                /* Reflection */
    if $\mathsf{C}\left(Q_r\right) < \mathsf{C}\left(Q_0\right)$ then                /* Expansion */
        $Q_e \leftarrow G + \gamma\left(G - Q_N\right)$
        if $\mathsf{C}\left(Q_e\right) < \mathsf{C}\left(Q_r\right)$ then
            $Q_N \leftarrow Q_e$
        else
            $Q_N \leftarrow Q_r$
        end
    else if $\mathsf{C}\left(Q_r\right) \geq \mathsf{C}\left(Q_{N-1}\right)$ then                /* Contraction */
        $Q_c \leftarrow Q_N + \frac{1}{\gamma}\left(G - Q_N\right)$
        if $\mathsf{C}\left(Q_c\right) < \mathsf{C}\left(Q_N\right)$ then
            $Q_N \leftarrow Q_c$
        else
            for $i \leftarrow 1$ to $N$ do                /* Reduction */
                $Q_i \leftarrow Q_0 + \frac{1}{\gamma}\left(Q_i - Q_0\right)$
            end
        end
    else
        $Q_N \leftarrow Q_r$
    end
end
$Q' \leftarrow Q_0$
```

A.4 Simulation settings of the fluid dynamic solver

We include the two main dictionaries which specify the run parameters of the flow solvers. These parameters are extensively described in [2] and have been kept unchanged for all coupled simulations. Of particular interest is the evaluation of the divergence of the Maxwell Stress Tensor div(T) in each control volume which is specified in the subsection divSchemes.

```
FoamFile
{
    version     2.0;
    format      ascii;
    class       dictionary;
    location    "system";
    object      fvSchemes;
}
// * * * * * * * * * * * * * * * * * * * * * * * * * * * * * * * * * * * * * //

ddtSchemes
{
    default         Euler;
}

gradSchemes
{
    default         Gauss linear;
}

divSchemes
{
    div(rho*phi,U)   Gauss limitedLinearV 1;
    div(phi,alpha)    Gauss vanLeer;
    div(phirb,alpha) Gauss interfaceCompression;
    div(T)                Gauss linear;
}

laplacianSchemes
{
    default         Gauss linear corrected;
}

interpolationSchemes
{
    default         linear;
}

snGradSchemes
```

```
{
    default         corrected;
}

fluxRequired
{
    default         no;
    p_rgh;
    pcorr;
    alpha1;
}


// *************************************************************************

FoamFile
{
    version     2.0;
    format      ascii;
    class       dictionary;
    location    "system";
    object      fvSolution;
}
// * * * * * * * * * * * * * * * * * * * * * * * * * * * * * * * * * * * * *

solvers
{
    pcorr
    {
        solver          PCG;
        preconditioner  DIC;
        tolerance       1e-10;
        relTol          0;
    }

    p_rgh
    {
        solver          PCG;
        preconditioner  DIC;
        tolerance       1e-07;
        relTol          0.05;
    }

    p_rghFinal
    {
        $p_rgh;
```

```
        tolerance       1e-07;
        relTol          0;
    }

    U
    {
        solver          PBiCG;
        preconditioner  DILU;
        tolerance       1e-06;
        relTol          0;
    }
}

PISO
{
    momentumPredictor no;
    nCorrectors     3;
    nNonOrthogonalCorrectors 0;
    nAlphaCorr      1;
    nAlphaSubCycles 2;
    cAlpha          1;
}


// ************************************************************************* //
```

List of Symbols

A	operator A
c	speed of light
c_a	capillary constant
dt	time step
detJ	Jacobian determinant
D	damping constant
$\vec{d}$	distance
$\vec{D}$	displacement current
ε	electrical permittivity
$\vec{E}$	electric field
f	frequency
F_d	drag force amplitude
$\vec{f_e}$	electric force density
$\vec{f_K}$	Kelvin force polarization density
$\vec{f_{KH}}$	Korteweg-Helmholtz force density
$\vec{f_s}$	surface tension force
$\vec{F_e}$	electric force
$\vec{g}$	gravitational force
γ	water fraction
h	length
H	Hessian
J	Jacobian
$J_{.i}$	Jacobian column vectors
K	spring constant
μ	kinematic viscosity
$\vec{\nabla}$	gradient
$\vec{\nabla}_s$	surface gradient
$\vert^n$	at instant n
Ω	computational domain
Ω_h	discretized computational domain
p	static pressure
$\vec{p}$	electric dipole moment
$\vec{P}$	electric dipole moment density
∂	partial derivative
Q	electrical charge
r	droplet radius
R_e	Reynolds number
ϱ_f	free charge density
ϱ_{f_s}	free surface charge density

σ	electrical conductivity
t	time
t_n	instant n
T	tetrahedron
T	Maxwell stress tensor
ϑ	angle
U	scalar potential
$\vec{u}$	fluid velocity
v	volume
(v_i)	scalar potential degrees of freedom i
V	scalar potential
χ	electric susceptibility
w	angular frequency
W	electrostatic energy density
W_a	work of adhesion per unit area
W_e	Weber number
x	global coordinates
ζ	local coordinates

Bibliography

[1] NGsolve. http://sourceforge.net/projects/ngsolve. (Cited on page 11.)

[2] OpenFoam. http://www.openfoam.com. (Cited on pages 11, 47, and 86.)

[3] Keim S. and König D. Study of the behavior of droplets on polymeric surfaces under the influence of an applied electrical field. Proceedings of IEEE Conference on Electrical Insulation and Dielectric Phenomena, 1999. (Cited on pages 11 and 55.)

[4] Langemann D. A droplet in a stationary field. Math. Comp. Simulation, 63:529–539, 2003. (Cited on page 11.)

[5] Langemann D. and Krüger M. 3d model of a droplet in an electric field. Math. Comp. Simulation, 66:539–549, 2004. (Cited on page 11.)

[6] Y. Mizuno O. Fujii, K. Honsali and K. Naito. Vibration of a water droplet on a polymeric insulating material subjected to ac voltage stress. IEEE trans. on Dielectrics and Electrical insulation, 17:566–571, 2010. (Cited on pages 15, 55, 64, 69, 70, and 76.)

[7] M. de Montigny and G. Rousseaux. On the electrodynamics of moving bodies at low velocities. European Journal of Physics, 27:755–768, 2006. URL: `http://iopscience.iop.org/0143-0807/27/4/007/`. (Cited on page 15.)

[8] F. Rapetti and G. Rousseaux. Implications of galilean electromagnetism in numerical modeling. IET 8th International Conference on Computation in Electromagnetics, 2011. URL: `http://dx.doi.org/10.1049/cp.2011.0062`. (Cited on page 15.)

[9] J. D. Jackson. Classical electrodynamics 3^{rd} edition. pages 165–167. (Cited on page 17.)

[10] J. R. Melcher. Continuum electromechanics. page 3.11. URL: `http://ocw.mit.edu/resources/res-6-001-continuum-electromechanics-spring-2009/textbook-contents/chap03_sec_100.pdf`. (Cited on pages 16 and 17.)

[11] Indian Institute of technology Kanpur. Distinction between an incompressible and a compressible flow. Webcourse Fluid mechanics lecture-2. URL: `http://nptel.iitm.ac.in/courses/Webcourse-contents/IIT-KANPUR/FLUID-MECHANICS/lecture-2/2-6-dist_incomp_comp.htm`. (Cited on page 25.)

[12] Feier-Iova S. and Hinrichsen V. Partial discharge inception voltage of water drops on insulating surfaces stressed by electrical field. Proceedings of IEEE Electrical Insulation Conference, pages 21–25, 2009. (Cited on pages 27 and 63.)

[13] Nazemi M.H. and Hinrichsen V. Partial discharge investigation and electric field analysis of different oscillation modes of water droplets on the surface of polymeric insulator under tangential ac electric field stress. Proceedings of the Eleventh IEEE International Conference on Solid Dielectric, 2013. (Cited on pages 27, 63, 64, 66, and 69.)

[14] Crank J. and Nicolson P. A practical method for numerical evaluation of solutions of partial differential equations of the heat conduction type. Proc. Camb. Phil. Soc, 43:50–67, 1947. (Cited on page 29.)

[15] Lapidus L. and Pinder G. Numerical solution of partial differential equations in science and engineering. John Wiley & Sons, pages 160–187, 1982. (Cited on page 29.)

[16] Céa J. Approximation variationnelle des problèmes aux limites. Annales de l'institut Fourier, 2:345–444, 1964. (Cited on page 30.)

[17] Brenner C.S. and Ridgway S. The mathematical theory of finite element methods second edition. Springer, page 137, 2000. (Cited on page 31.)

[18] Schoeberl J. and Zaglmayr S. High order nédélec elements with local complete sequence properties. COMPEL, 24:374–384, 2005. (Cited on page 32.)

[19] College of Enginering & Applied Science University of Colorado Boulder. The quadratic tetrahedon. Webcourse Advanced Finite Element lecture 17. URL: `http://www.colorado.edu/engineering/CAS/courses.d/AFEM.d/AFEM.Ch17.d/AFEM.Ch17.Slides.d/AFEM.Ch17.Slides.pdf`. (Cited on pages 34 and 79.)

[20] PETSc. http://www.mcs.anl.gov/petsc/petsc-current/docs/manualpages/ksp/kspcg.html. (Cited on page 38.)

[21] Márquez Damián S. An extended mixture model for the simultaneous treatment of short and long scale interfaces. 2013. (Cited on pages 47 and 48.)

[22] Hirt C.W. and Nichols B.D. Volume of fluid (VOF) method for the dynamics of free boundaries. Journal of Computational Physics, 39:201–225, 1981. (Cited on pages 47 and 57.)

[23] Kothe D.B Brackbill J.U. and Zemach C. A continuum method for modeling surface tension. Journal of Computational Physics, 100:335–354, 1992. (Cited on page 48.)

[24] Issa R. I. Solution of the implicitly discretized fluid flow equations by operator splitting. Journal of Computational Physics, 62:40–65, 1986. (Cited on page 50.)

[25] Fatollahi A. and Hajirahimi M. Making sessile drops easier. cond-mat.soft, abs/1304.6366, 2013. (Cited on page 53.)

[26] Mathematica. http://wolfram.com/mathematica. (Cited on page 53.)

[27] Nelder J. and Mead R. A simplex method for function minimization. Computer Journal 7, pages 308–313, 1965. (Cited on page 60.)

[28] Lamb H. Hydrodynamics. Cambridge University Press, 1932. (Cited on pages 72, 74, and 75.)

[29] Strani M. and Sabetta F. Free vibrations of a drop in partial contact with a solid support, volume 141. 1984. (Cited on page 73.)

[30] Kim H. Yang J. and Chung J. Resonant oscillation phenomena of a sessile droplet on electrohydrodynamic jetting nozzle, volume 53. 2014. URL: `iop.science.iop.org/1347-4065/53/5S3/05HC03/article`. (Cited on page 75.)

Curriculum Vitae

Personal Data

Name: Harald Songoro

Date of birth: 03.01.1971

Place of birth: Orléans, France

Email: harald.songoro@gmail.com

Professional Experience / Education

01/2013 - Heute	Principal Engineer, CST AG, Darmstadt, Germany
09/2010 - Heute	Ph.D. Candidate at the Computational Electromagnetics Laboratory (TEMF), Technische Universität Darmstadt, Darmstadt, Germany
11/2005 - 07/2010	Lead Research Engineer within the HFSS solver group at Ansoft /ANSYS, Pittsburgh, USA
05/2000 - 10/2005	Lead Research Engineer for SEMCAD X at Schmid and Partner Engineering AG (SPEAG), Zürich, Switzerland
11/1997 - 03/2000	Research Engineer at Firstmark Technologies in charge of the EMC and safety aspects of hand-held terminals project for the European Space Agency and Bell Mobility, Ottawa, Canada
09/1996 - 10/1997	Research Engineer at Realix Technologies in charge of the Electrostatic Characterization Discharge project for the European Space Agency and the Canadian Space Agency, Ottawa, Canada
09/1994 - 10/1995	Diplôme d'Études Approfondies in Theoretical Computing and Parallelization, Institut National Polytechnique de Toulouse, France
09/1988 - 10/1994	Diplôme d'Ingénieur des Grandes Écoles in Computer Science and Applied Mathematics, ENSEEIHT, Toulouse, France